

# **Distributed Logistics in an Urban Setting Using Small Unmanned Aerial Vehicles**

May 29, 2015

**Team Lakshya-IIISc: SDC Final Proposal**

## Acknowledgement

Team Lakshya-IISc would like to acknowledge the following professors, technical advisors and students for their assistance:

Dr. Ranjan Ganguli (Professor), Department of Aerospace Engineering, Indian Indian Institute of Science

Dr. Dineshkumar Harursampath (Assistant Professor), Department of Aerospace Engineering, Indian Indian Institute of Science

Dr. S N Omkar (Chief Research Scientist), Department of Aerospace Engineering, Indian Indian Institute of Science

Titas Bera (PhD student), Department of Aerospace Engineering, Indian Indian Institute of Science

Rajarshi Bardhan (PhD student), Department of Aerospace Engineering, Indian Indian Institute of Science

Ganesh S (Graduate student), Department of Aerospace Engineering, Indian Indian Institute of Science

Kalaiselvam (Project Assistant), Department of Aerospace Engineering, Indian Institute of Science

Gautham Anand (Project Assistant), Department of Aerospace Engineering, Indian Institute of Science

Ravi Kumar (Project Assistant), Department of Aerospace Engineering, Indian Institute of Science

Amod Hulge and Aditya Wagh of QRERA, Bangalore

## **32<sup>nd</sup> Annual AHS International Student Design Competition (SDC)**

### **Letter of Intent**

This letter is to express the intent of the undersigned to participate as a Graduate team for the 32<sup>nd</sup> Annual AHS International Student Design Competition.

**Name of the University:** Indian Institute of Science, Bangalore, India

**Name of the team:** Team Lakshya

**Category:** Graduate team

#### **Team members:**



**Rajnish Mallick, Team Captain**

(Graduate Student)

Email id: [rajnish@aero.iisc.ernet.in](mailto:rajnish@aero.iisc.ernet.in)



**Pothula Shiva Harsh**

(Graduate Student)

Email id: [shivaharsh.p@gmail.com](mailto:shivaharsh.p@gmail.com)



**D R Abhiram, Team Vice Captain**

(Graduate Student)

Email id: [abhiram@aero.iisc.ernet.in](mailto:abhiram@aero.iisc.ernet.in)



**Vinod Kumar Datusliya**

(Graduate Student)

Email id: [vinodkd@aero.iisc.ernet.in](mailto:vinodkd@aero.iisc.ernet.in)



**Nilanjan Chattaraj**

(Graduate Student)

Email id: [nilanjan@aero.iisc.ernet.in](mailto:nilanjan@aero.iisc.ernet.in)



**Shashank Agrawal**

(Graduate Student)

Email id: [shash7.shashank@gmail.com](mailto:shash7.shashank@gmail.com)



**Manu Kamin**

(Graduate Student)

Email id: [manu.kamin@gmail.com](mailto:manu.kamin@gmail.com)

**Faculty Advisors:**



**Dr. Ranjan Ganguli**  
Professor,  
Department of Aerospace Engineering, Indian Institute of Science  
**Email id:** [ganguli@aero.iisc.ernet.in](mailto:ganguli@aero.iisc.ernet.in)



**Dr. Dinesh Kumar Harursampath**  
Associate Professor,  
Department of Aerospace Engineering, Indian Institute of Science  
**Email id:** [dinesh@aero.iisc.ernet.in](mailto:dinesh@aero.iisc.ernet.in)



**Dr. S.N Omkar**  
Chief Research Scientist,  
Department of Aerospace Engineering, Indian Institute of Science  
**Email id:** [omkar@aero.iisc.ernet.in](mailto:omkar@aero.iisc.ernet.in)

# Contents

<b>1</b>	<b>Introduction</b>	<b>13</b>
1.1	Helicopter Performance Analysis . . . . .	13
1.1.1	Combined Blade Element Momentum Theory . . . . .	14
1.1.2	Numerical Implementation of BEMT . . . . .	15
<b>2</b>	<b>Micromechanics Analysis for Energy Harvesting Application in Helicopter Rotor Blade</b>	<b>18</b>
2.1	Introduction . . . . .	18
2.2	Literature Survey . . . . .	19
2.3	Purpose of Work . . . . .	20
2.4	General terminologies . . . . .	21
2.4.1	VAM . . . . .	21
2.4.2	Variational Asymptotic Method for Unit Cell Homogenisation (VAMUCH) . . . . .	22
2.4.3	Geometrically Exact Beam Theory (GEBT) . . . . .	22
2.4.4	Piezoelectricity . . . . .	23
2.4.5	Interdigitated Electrodes . . . . .	23
2.4.6	Connectivity . . . . .	24
2.5	Mathematical Formulation . . . . .	24
2.6	Results & Discussions . . . . .	27
2.6.1	Effective Material Properties estimation and comparison . . . . .	27
2.6.2	Validation study . . . . .	35
2.6.3	Results obtained with practical loads cases . . . . .	36
<b>3</b>	<b>Helicopter Blade: Structural Design and Analysis</b>	<b>42</b>
3.1	Introduction . . . . .	42
3.1.1	Background . . . . .	43
3.1.2	Literature Survey . . . . .	43
3.2	Theoretical Approach . . . . .	43

3.2.1	Design of Rotor Blade Cross-section . . . . .	44
3.3	Structural Analysis Formulation . . . . .	45
3.3.1	Cross-Sectional Analysis Formulation . . . . .	46
3.3.2	Nonlinear Beam Analysis Formulation . . . . .	47
3.4	Base Case Analysis . . . . .	48
<b>4</b>	<b>Design Optimization</b>	<b>50</b>
4.1	Taguchi Method of Design . . . . .	50
4.2	Robust Design of Unmanned Helicopter Rotor for Hover Using Taguchi Method . . . . .	53
4.2.1	Design Parameters and Noise Factors . . . . .	53
4.2.2	Parameter Design Using Taguchi Method . . . . .	53
4.3	Evolutionary Algorithms Inspired Multi-Objective Optimization . . . . .	58
4.4	Optimization problem . . . . .	58
4.5	Response surface method . . . . .	60
4.6	Orthogonal array . . . . .	61
4.7	Multi-objective bat algorithm . . . . .	61
4.7.1	Echolocation of bats . . . . .	63
4.7.2	Pareto optimal multi-objective bat algorithm . . . . .	63
4.8	Results and discussion . . . . .	65
4.8.1	Response Surface generation . . . . .	66
4.8.2	Multi-objective Pareto optimal design . . . . .	66
<b>5</b>	<b>Vehicle Routing Problem and Path Planning of Aerial Vehicles</b>	<b>71</b>
5.1	Introduction . . . . .	71
5.2	Vehicle Routing Problem . . . . .	72
5.3	Path Planning Algorithm . . . . .	73
5.4	State Space Formulation of Motion Planning . . . . .	75
5.5	Rapidly Exploring Random Tree: Algorithm and Simulation . . . . .	77
5.6	Preprocessing of State Space . . . . .	83
5.7	Simulation . . . . .	89
<b>6</b>	<b>Hardware System Validation</b>	<b>94</b>
6.1	3D Scanning and CAD Model of Quadcopter Blade . . . . .	94
6.2	3D Printing . . . . .	94
6.3	Fabrication and design of the quadcopter . . . . .	97
6.4	Hardware Components . . . . .	97
6.5	Final Quadcopter Design . . . . .	108

<b>7 Cost Analysis</b>	<b>109</b>
7.1 Cost associated to forward supply locations . . . . .	109
7.2 Cost for electricity consumed by vehicles . . . . .	110
7.3 Pounds of CO <sub>2</sub> released for grid based charging . . . . .	110
7.4 Vehicle repair labor and operation . . . . .	111
7.5 Development cost of RUAVs based on empty weight . . . . .	111

# List of Figures

1.1	Payload weight frequency . . . . .	14
1.2	Zones in the urban area . . . . .	15
2.1	The effective homogenised model from the fiber matrix composite . . . . .	20
2.2	A typical piezofiber[1] . . . . .	23
2.3	An arrangement of interdigitated electrodes . . . . .	24
2.4	Coordinate direction along which the material properties are prescribed. .	26
2.5	Piezofiber Matrix Composite with different Fiber Volume fraction . . . . .	27
2.6	Young's Modulus in Longitudinal Direction . . . . .	31
2.7	Young's Modulus in Transverse Direction . . . . .	32
2.8	Inplane Shear Modulus . . . . .	32
2.9	Major Poisson Ratio . . . . .	33
2.10	Young's Modulus in Transverse direction and Transverse Shear Modulus .	33
2.11	Minor Poisson Ratios . . . . .	34
2.12	Effective Density . . . . .	34
2.13	Fiber matrix model with transverse concentrated force at the tip . . . . .	35
2.14	Centrifugal, thrust and drag loads on the unit cell model. . . . .	36
2.15	Variation of Electric flux density with time . . . . .	38
2.16	Variation of Electric field with time . . . . .	38
2.17	Capacitor model for unit cell . . . . .	39
2.18	Variation of Charge generation with time . . . . .	39
2.19	Variation of Electric Potential with time . . . . .	40
2.20	Variation of Electrostatic energy density with time . . . . .	41
3.1	A typical rotor blade cross-section . . . . .	42
3.2	Undeformed & deformed geometries in VAM formulation . . . . .	44
3.3	Flowchart of Structural Analysis . . . . .	46
3.4	Meshed Model . . . . .	48
3.5	L-18 Table with corresponding stiffness norm & weight per unit length .	49

4.1	Variation in $y_1$ for $x_1$ and $x_2$ in design space . . . . .	69
4.2	Variation in $y_2$ for $x_1$ and $x_2$ in design space . . . . .	69
4.3	Pareto curve for blade cross-section design with four parameters . . . . .	70
5.1	A genetic algorithm solution for a vehicle routing problem. Number of customers are 50 and number of vehicles used are 6 . . . . .	73
5.2	A configuration space $S^2$ and collection of tangent vectors at $q$ . . . . .	76
5.3	Reachable set of $x_0$ and the collision states . . . . .	76
5.4	(a) RRT vertices after 200 iterations, the aircraft's position and orientation at some RRT nodes are also shown, (b) Illustration of Extend function of RRT algorithm c) RRT vertices after many iterations [2] . . . . .	80
5.5	Bug Trap Problem. Dynamic domain sampling for RRT exploration [3]. . . . .	84
5.6	The regions $x_1, x_2, x_3$ and their transition probabilities . . . . .	85
5.7	Voronoi partition of state space. . . . .	88
5.8	(a) Figure showing the quad rotor initial position and the customer location	90
5.9	(a) Figure showing the path planned by the modified RRT algorithm . . . . .	91
5.10	(a) Zone sequence as obtained from modified RRT (b) modified RRT vertices distribution after 2000 iteration (c) Path closest to the final state found by modified RRT after 4000 iteration (d) $u, w, q$ and $\theta$ variation along the path generated by the modified RRT. Clearly distance from goal configuration to the closest Tree node for modified RRT is less than the basic RRT . . . . .	92
5.11	Figures showing different instance of OpenGL based simulation of quad rotor path planning and obstacle avoidance. . . . .	93
6.1	3D Scanner . . . . .	95
6.2	Cloud Points Generated from 3D Scanner . . . . .	95
6.3	3D Surface of Blade . . . . .	96
6.4	3D CAD Model of Blade . . . . .	96
6.5	Brushless DC motor, which is used to build the quadcopter . . . . .	98
6.6	Clockwise and anticlockwise propeller of the quad copter . . . . .	99
6.7	An arm of the quadcopter Frame . . . . .	100
6.8	Central Body of the Quadcopter Frame . . . . .	101
6.9	Quad-Copter Frame With Crab Landing Gear . . . . .	101
6.10	Electronic speed controller . . . . .	102
6.11	Speed controller connector PCB . . . . .	103
6.12	Multiwii_Pro/ MegaPirate Flight controller . . . . .	104
6.13	Li-Po Battery . . . . .	106
6.14	RC Transmitter and receiver module . . . . .	107

6.15	Direction of propeller rotation	108
6.16	Complete quadcopter	108

# List of Tables

2.1	Material Constants . . . . .	28
2.2	Material Constants . . . . .	28
2.3	Material Constants . . . . .	28
2.4	Material Constants . . . . .	28
2.5	Effective Material Properties . . . . .	29
2.6	Effective Material Properties . . . . .	29
2.7	Effective Material Properties . . . . .	30
2.8	Effective Material Properties . . . . .	30
2.9	Effective Material Properties . . . . .	31
2.10	Recovered Stress . . . . .	35
2.11	Recovered Stress . . . . .	35
2.12	Recovered Stress . . . . .	37
2.13	Recovered Stress . . . . .	37
3.1	Base Case Data Set . . . . .	48
4.1	Design parameters, levels and noise values . . . . .	55
4.2	Standard $L_9(3^4)$ orthogonal array . . . . .	55
4.3	Standard $L_8(2^7)$ orthogonal array . . . . .	55
4.4	Design parameter matrix: Inner array $L_9(3^4)$ . . . . .	56
4.5	Noise matrix for 1 <sup>st</sup> experiment: Outer array $L_8(2^4)$ . . . . .	56
4.6	Results of 9 parameter design experiments . . . . .	57
4.7	Comparison of baseline helicopter design with robust design . . . . .	57
4.8	A 3-level MGB4P-OA orthogonal array for four parameters . . . . .	62
4.9	Coded and physical values of design variables for four parameters . . . . .	65
4.10	Comparison between predicted response and VAM analysis for $y_1$ using MGB4P-OA . . . . .	67
4.11	Comparison between predicted response and VAM analysis for $y_2$ using MGB4P-OA . . . . .	68

6.1	Specification of the Brushless DC motor . . . . .	98
6.2	Quad copter Propeller . . . . .	99
6.3	Quad-Copter Frame With Crab Landing Gear . . . . .	100
6.4	Electronic speed controller . . . . .	102
6.5	Speed controller connector PCB . . . . .	103
6.6	Multiwii_Pro/ MegaPirate Flight controller . . . . .	104
6.7	Li-Po Battery . . . . .	106
7.1	Measures of effectiveness at a glance . . . . .	110

# **Chapter 1**

## **Introduction**

Rotorcrafts are versatile machines, which can perform vertical takeoff and landing at almost any terrain. To address the problem of distributive logistics using unmanned aerial vehicles in an urban setting, we propose a solution using a combination of type-I helicopter and quadrotor. Here type-I helicopter used in the final proposal is similar to Yamaha R-MAX with an advanced rotor blade design configuration, called thereafter as Advanced R-MAX helicopter. A quadrotor is type of rotorcraft equipped with four rotor placed symmetrically around its centre. It can perform hover, forward flight, vertical takeoff and landing (VTOL) and therefore, classified as a rotary wing VTOL aircraft. In this proposal, the light weight packages are delivered to the customers by both quadcopters and Advanced R-MAX helicopters. However, medium and heavy weight packages are only delivered by the Advanced R-MAX helicopters only. The package/payload weight frequency is mentioned in Figure 1.1. The whole region of interest for package distribution is divided in to five zones for effective delivery of goods, as illustrated in Figure 1.2. The helicopter performance analysis of the Advanced R-MAX is presented in the following section.

### **1.1 Helicopter Performance Analysis**

The main rotor is a very critical component of helicopter as it is responsible for three important functions - generation of thrust for hover and vertical flight, generation of horizontal force for forward flight, and generation of forces and moments (along with the tail rotor) to control it's attitude and position. Thus, an accurate estimation of the main rotor performance becomes essential for a good rotor design. Even for hover, where the flow is azimuthally axisymmetric and is considered easiest to analyse, performance prediction is still not straightforward as the rotor operates in a complex aerodynamic environment

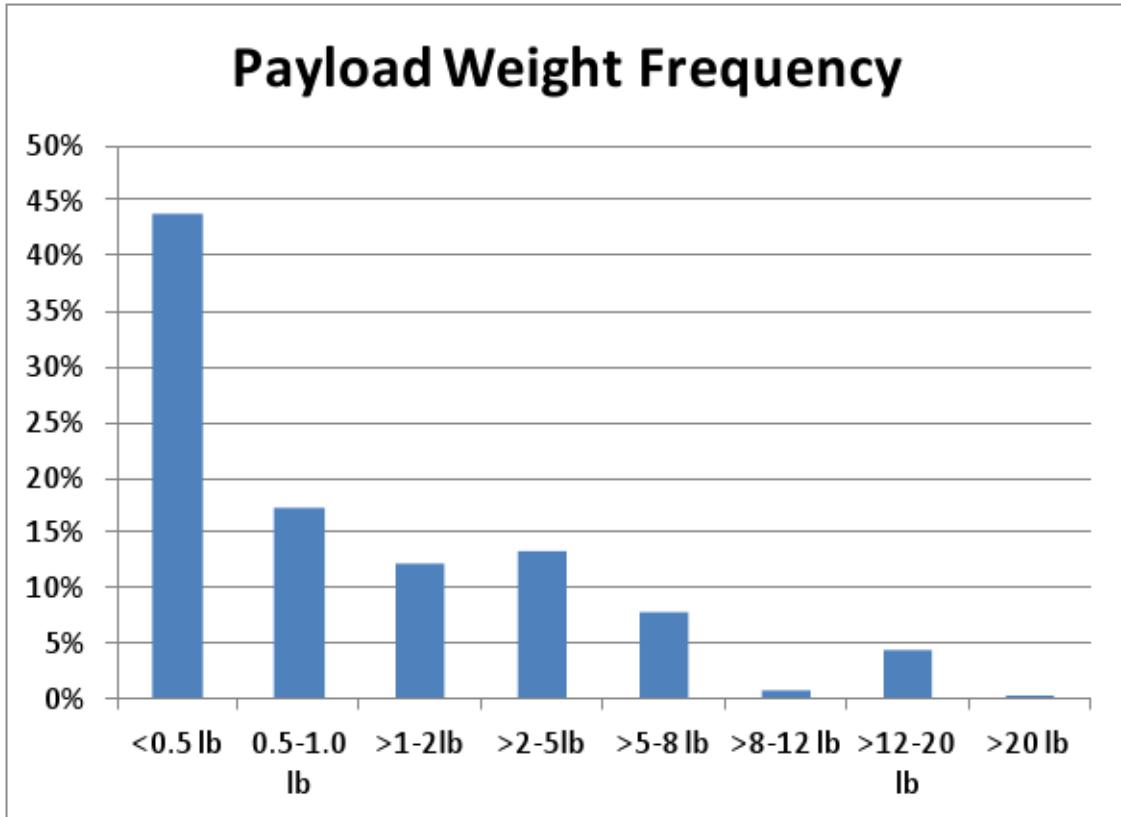


Figure 1.1: Payload weight frequency

consisting of vortical wakes. As such, the aerodynamics considered in the analysis will influence the rotor design to a large extent. For the initial design studies aimed at rotor sizing and performance analysis of the helicopter RUAU used, blade element momentum theory principles have been used.

### 1.1.1 Combined Blade Element Momentum Theory

The BEMT is a hybrid approach combining the principles of both momentum theory and blade element theory. The rotor blades are idealized as a permeable rotor disk; which are made up of successive annuli. Conservation of mass, momentum and energy equations are applied to a small annulus of the rotor, and it's incremental thrust and power are calculated based on momentum theory. It is assumed that successive rotor annuli have no mutual effects on each other. In this study, numerical implementation of the BEMT

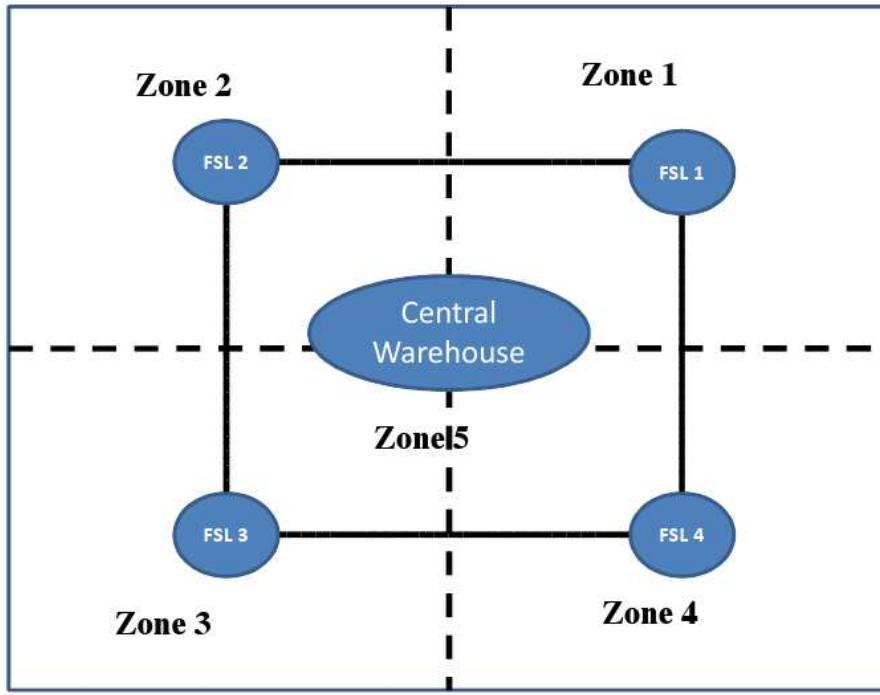


Figure 1.2: Zones in the urban area

equations are carried out for performance analysis, as this can be used for arbitrary radial variations in blade twist and taper.

### 1.1.2 Numerical Implementation of BEMT

The various steps involved in performance analysis, based on equations from reference [4], are enumerated below.

1. The blade is uniformly discretized into a series of small elements (totalling to  $N$ ), each of which are of span  $\Delta r$  (non-dimensional length).
2. The rotor collective pitch,  $\theta_0$ , is calculated for the required thrust coefficient. Starting from an initial value (based on uniform inflow assumption), the collective pitch is updated iteratively [4].
3. Next, the inflow and Prandtl's tip loss function,  $F$ , are calculated iteratively until

convergence:

$$\lambda_n = \frac{\sigma a_0}{16 F_n} \left( \sqrt{1 + \frac{32 F_n \theta_n r_n}{\sigma a_0}} - 1 \right) \quad (1.1)$$

$$F_n = \frac{2}{\pi} \cos^{-1} \left( e^{-f_n} \right) \quad (1.2)$$

where  $f_n$  is given by

$$f_n = \frac{N_b}{2} \left( \frac{1 - r_n}{\lambda_n} \right) \quad (1.3)$$

4. Once the pitch,  $\theta_n$  and inflow,  $\lambda_n$ , have been obtained, the rotor thrust coefficient is calculated as:

$$(\Delta C_T)_n = \frac{\sigma a_0}{2} (\theta_n r_n^2 - \lambda_n r_n) \Delta r \quad (1.4)$$

$$\Rightarrow C_T = \sum_{n=1}^N (\Delta C_T)_n \quad (1.5)$$

where,  $(\Delta C_T)_n$  is the thrust coefficient of the  $n^{th}$  element.

5. The induced power coefficient is then given by:

$$(\Delta C_{Pi})_n = \lambda_n (\Delta C_T)_n \quad (1.6)$$

$$\Rightarrow C_{Pi} = \sum_{n=1}^N (\Delta C_{Pi})_n \quad (1.7)$$

where,  $(\Delta C_{Pi})_n$  is the induced power coefficient of the  $n^{th}$  element.

6. With the blade pitch and inflow distribution known, the angle of attack,  $\alpha$ , of each of the blade elements can be calculated. With this, the rotor profile power coefficient,  $C_{Po}$ , can be calculated as given below:

$$(\Delta C_{Po})_n = \frac{\sigma}{2} C_d r_n^3 \Delta r \quad (1.8)$$

where,  $C_d = C_{d0} + d_1 \alpha + d_2 \alpha^2$ .

$$\Rightarrow C_{Po} = \sum_{n=1}^N (\Delta C_{Po})_n \quad (1.9)$$

7. The net power coefficient of the rotor,  $C_P$ , the total rotor power,  $P_T$ , and the rotor figure of merit,  $FM$  are calculated as given below:

$$C_P = C_{Pi} + C_{Po} \quad (1.10)$$

$$P_T = \rho A (\Omega r)^3 C_P \quad (1.11)$$

$$FM = \frac{C_T^{3/2}}{C_P} \quad (1.12)$$

# **Chapter 2**

## **Micromechanics Analysis for Energy Harvesting Application in Helicopter Rotor Blade**

### **2.1 Introduction**

Multifunctional composites are in fact an exciting area of research now a days. Improving the properties of materials to satisfy certain desired conditions is at a saturated stage. Now the researchers are focussing on how to use the same material or structure for multitasking, thereby reducing the weight and volume. The multifunctional composites consisting of piezo-ceramic fiber can be used in a wide variety of fields such as, structural health monitoring, energy harvesting, actuation etc. Depends on the applicability, the piezoelectric material and the binding material changes. Also we need to determine the proper volume fraction of fiber along with the amount of polarisation to achieve the desired performance. Usually the piezo-ceramic fiber matrix are orthotropic and heterogeneous, that is the properties not only depends on direction but also position. A homogeneous model of the composite structure is generated so that to conduct a comparative studies among different materials. The present work is oriented towards the multi scale modelling of multifunctional composites consisting piezo-ceramic fibers. The essence from the Variational Asymptotic Method (VAM) and Finite Element Method (FEM) are used for modelling the composite structure. Using VAM, the computational effort for developing the analytical framework reduces to a large extent without reducing the accuracy. The numerical model based on FEM over the analytical framework of the representative volume element (RVE) ensures modelling complex realistic geometries and material distributions. Electromechanical analysis has been carried out to explore the energy har-

vesting capabilities of the multifunctional piezo-fiber composites considered in this work.

## 2.2 Literature Survey

The idea of using piezoceramic materials for energy harvesting took shape decades ago. But its applications cannot get green light because of the high energy loss in the electronic components. Due to the rapid development in electronics now a days, this idea has come to the forefront again. The basics of the piezoelectric fiber composites along with its development, modelling and application can be found in [5]. The piezoceramic most widely used are PZT and its derivatives. Above the Curie point, there will be no piezoelectricity. The modelling of the piezoelectric module with interdigitated electrodes are developed in [6]. Here the interdigitated electrode design (IDE design) which allows to utilise the primary piezoelectric effect in longitudinal direction for piezoelectric sheet actuator is investigated with the help of a detailed finite element analysis. From [6], we can see that for improving the performance, we need to decrease the electrode finger width and increase the electrode finger distance. The details regarding unit cell homogenisation for transversely isotropic materials are available from [7]. The electromechanical Reissner Mindlin model is developed for laminated piezoelectric plate in [8]. The variational statement is formed using the Hamilton's principle considering the kinetic energy, electric enthalpy, and the virtual work of applied loads and electric charge. After the construction of the Reissner Mindlin model, 2D variational statement is generated for the electromechanical problem. A generalised Timoshenko model developed for prismatic beam structures with embedded or surface mounted piezoelectric materials can be seen in [9]. The X-FEM implementation of VAMUCH are explained in [10]. The extended FEM allows one to use meshes not necessarily matching the physical surface of the problem but retains accuracy. The micro-mechanic model such as X-Y and Y-X are developed in[11] for predicting the non-linear behaviour of piezoelectric fiber reinforced composite materials. A micro-mechanical study on the effective non-linear behaviour of electrostrictive multiphase composites is developed in [12] based on Variational Asymptotic Method (VAM). The homogenisation is done through unit cell approach and a quasi continuum approach is used to avoid the difficulty associated with discrete integer arguments. The method can be applied for modelling other non-linear behaviour such as elasto-plastic, non-linear elastic, non-linear behaviour of composites containing shape memory alloys etc. Most of the above models are based on VAM developed by V.L Berdichevsky in 1978 [13].

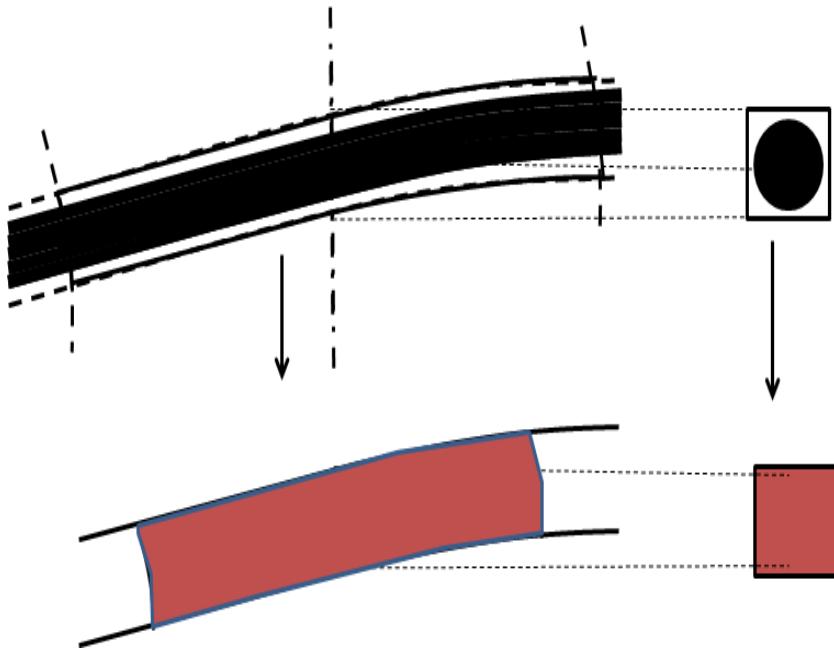


Figure 2.1: The effective homogenised model from the fiber matrix composite

### 2.3 Purpose of Work

From the literature, it is found that many attempts were made for getting effective homogeneous properties for specific cases. The high level of vibrations in the helicopter blades is a very good source for energy harvesting. The purpose of the present work is to get the point wise displacement fields and the electric charges developed in the material due to the applied force fields. Here, the problem is modelled in two length scales - micro electromechanics and macro electromechanics. The building block used to model the circular cross section Active Fiber Composites is from Hashin Rosen approach[14]. The micro mechanical analysis is done using VAMUCH [15]. The homogeneous effective stiffness obtained from VAMUCH is fed to the GEBT [16] to get the macro displacements. These macro displacement fields are input to VAMUCH again to recover the point wise local fields and electromechanical couplings. A validation study is done using Abaqus (an established 3D FEM solver).

## 2.4 General terminologies

### 2.4.1 VAM

Variational Asymptotic method (VAM) introduced by Berdichevsky[13], is a mathematical approach to determine the solution using the advantages of the existence of small parameters and in an asymptotic sense.

The small parameters are inherent to almost all the system like the size of gas molecules in a container, displacements or deformations in some systems, thickness of plates or shells. Such problems can be efficiently investigated using VAM. VAM is defined as the asymptotic analysis of a functional. It is a finite variable optimisation problem. In VAM only a functional called Lagrangian is investigated instead of a system of differential equations. This makes it simpler. The approximate equations of VAM always possess a variational structure.

In VAM the small terms in the energy functional are identified and neglected without losing the uniqueness or existence of solution. The main issue is to identify the leading terms. But it is not a problem in many cases. For example, in the neighbourhood of point  $u = 0$ , and taking small parameter to be,  $u_2$  is globally secondary with respect to  $u_2$  and  $u_3$  is locally secondary with respect to  $u_2$ . Generally, several adhoc assumptions are used in practical situations to reduce the 3D elasticity problem for simplifying the analysis. This creates inaccuracies in results and the reliability is lost to some extent. So there is an ever increasing demand for a methodology where the process is simple but the adhoc assumptions used are negligible. VAM is such a method which, analyses the 3D framework entirely, uses the existence of small parameters to dimensionally reduce so that the accuracy of the results is retained. The closed form analytical solutions for anisotropic materials can be easily obtained through VAM which are very difficult with other methods.

The process in VAM is done in a sequence as zeroth order approximation, first order approximation, etc. Usually the first order approximation will provide the accurate enough results as far as a structural problem is concerned. Basic structural problems which can be dimensionally reduced are classified into beam problems and shell problems. If one dimension is much larger than the other two dimensions, then beam analysis is done. But if two dimensions are larger than the third one, shell analysis is carried out. The problem arises if we cannot determine whether shell analysis or beam analysis is to be done. We rely on phantom analysis to get the displacement field.

## **2.4.2 Variational Asymptotic Method for Unit Cell Homogenisation (VAMUCH)**

Variational Asymptotic Method for Unit Cell Homogenisation (VAMUCH) is a code introduced by Prof. Wenbin Yu to generate the effective homogeneous properties of heterogeneous materials. It is used in micro-mechanics where the fiber and matrix possess individual strength and stiffness which makes the analysis complex. It is necessary to get the homogeneous properties of the fiber-matrix combination for doing macro-analysis. VAMUCH uses VAM, and it uses the finite element mesh to model the domain, which can be used to model the domain of any complex cross section. Its outputs are the effective stiffness properties, the effective density, porosity etc. The 3D point wise local field distribution can also be recovered using VAMUCH. The code can be used in all areas of Physics such as elasticity, conductivity, dielectrics, magnetics and diffusion areas. It can also predict coupled properties such as coefficient of thermal expansion, pyroelectric, pyromagnetic, piezoelectric, piezomagnetic, and electro-magnetic field. Although VAMUCH theory is solved using finite element technique, it is very different from the finite element micro-mechanics approach. In finite element approach, the fundamental variables are displacements, whereas in VAMUCH, they are fluctuating functions. Also while predicting effective properties different boundary conditions need to be maintained in FEM based model. But in VAMUCH, only the periodic boundary conditions are enough to be maintained for getting all the effective properties.

## **2.4.3 Geometrically Exact Beam Theory (GEBT)**

Geometrically Exact Beam Theory (GEBT) is a code for the macro analysis to obtain the 3D displacement field along the 1D. It is based on the mixed variational formulation of the geometrically exact intrinsic beam theory developed by Hodges [17]. The output from the GEBT is input to VAMUCH to recover the 3D pointwise displacement, strains, and stress distribution within the structure. GEBT uses the lowest possible shape functions, and the element matrices are exactly calculated without numerical integration. GEBT can be used for static or dynamic, linear or non-linear, steady or transient, with or without initial curvatures, with prescribed loading or varying sectional properties. GEBT is a versatile tool which can treat an arbitrary assembly of beams made of arbitrary material and oriented arbitrarily in 3D space. GEBT has a built in 1D finite element mesh generator. The output of a GEBT will be macro displacements, rotations and internal forces and moments. For dynamic analysis, apart from above linear and angular moments are also outputted.

## 2.4.4 Piezoelectricity

Piezoelectricity refers to generation of electrical energy on application of mechanical pressure. It is the linear electromechanical interaction between the mechanical and electrical state in crystalline materials. It is a reversible process. The piezoelectric materials includes quartz, tourmaline crystals, calcites, Rochelle salt, lead zirconate titanate (PZT), polyvinylidene fluoride (PVDF).

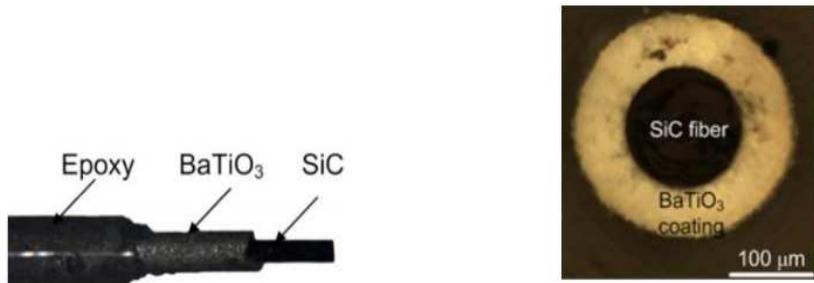


Figure 2.2: A typical piezofiber[1]

The piezo-structure creates an electric dipole moment in the crystal lattices, which is sensitive to both elastic strain and applied electric field. In piezo actuators, the converse effect (i.e. from electrical energy to mechanical energy) is used while in sensors, the direct piezo effect (i.e. from mechanical to electrical) is used. The adjoining figure illustrates a piezo fiber composite specimen.

## 2.4.5 Interdigitated Electrodes

The conventional set-up of a film actuator in which the piezoelectric sheet is poled in thickness direction, utilises the transverse piezoelectric effect. While this design is adequate for many applications, the effect is isotropic in the actuator plane and does not allow a decoupling of the longitudinal and transverse deformations. The transverse effect is also weaker (about 50%) than the primary piezoelectric effect which occurs in the poling direction. Therefore, IDE (Interdigitated electrodes) are used for maintaining an electric field in the longitudinal direction thereby exploiting the primary piezoelectric effect. As the electrode coating is very thin, it has no mechanical effect and has not been included into the model as an extra material. Figure 2.3 illustrates an arrangement of IDEs along the piezofibers

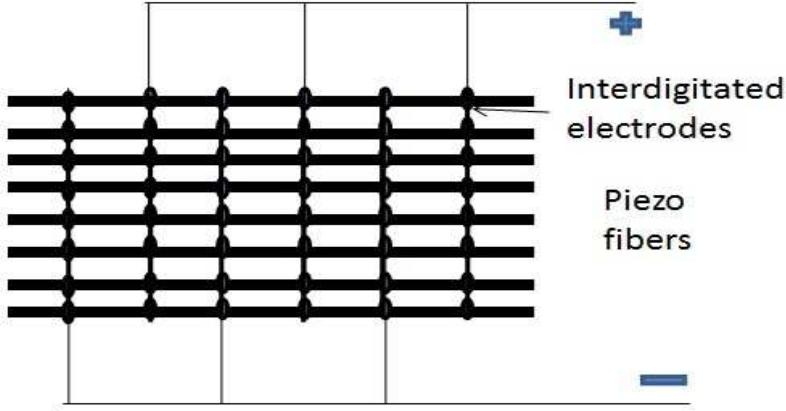


Figure 2.3: An arrangement of interdigitated electrodes

#### 2.4.6 Connectivity

Newnham[18] introduced the concept of connectivity for describing the number of dimensions that each phase was physically in contact with itself. According to the connectivity of two phase composites, the composites geometry can be classified into 10 structures. They are 0 - 0, 0 - 1, 0 - 2, 0 - 3, 1 - 1, 1 - 2, 1 - 3, 2 - 1, 2 - 2, 2 - 3, 3 - 1, 3 - 2, 3 - 3. For piezo composites, of the two numbers the first one corresponds to the physical connectivity of the active phase and the second number denotes the physical connectivity of the passive phase. The 1 3 composites is the most widely studies and utilised . Here the individual piezo-ceramic fibers are poled in the longitudinal direction. The advantages of this type of arrangement includes high coupling factors, low acoustic impedance, mechanical flexibility and broad bandwidth.

### 2.5 Mathematical Formulation

A brief outline of the piezoelectric fiber composite model and theory behind homogenization are provided in this section. The work done in an electromechanical system [1] involves elasticity and electric parts. The net work done of the system is given by

$$dW = Vidt + f\dot{\Delta}dt; = VdQ + fd\Delta; \quad (2.1)$$

where  $V$  is the electric potential,  
 $i$  is the electric current,

$f$  is the force field,  
 $\Delta$  is the displacement,  
 $Q$  is the charge.

So the constitutive equations become

$$f = \frac{\partial W_e}{\partial \Delta}; V = \frac{\partial W_e}{\partial Q} \quad (2.2)$$

Using Legendre transformation, a co-energy function defined as

$$W_e^*(\Delta, V) = VQ - W_e(\Delta, Q) \quad (2.3)$$

Now

$$dW_e^* = QdV - fd\Delta; \quad (2.4)$$

The Lagrangian is defined as

$$L = T^* + W_e^* - V \quad (2.5)$$

where  $T^*$  is the total kinetic energy and  $V$  is the work done by the external forces.

The co-energy density function composed of mechanical, electrical and electromechanical coupling components.

$$W_e^*(\Gamma, E) = \frac{1}{2}\{\Gamma\}^T[s]\{\Gamma\} - \{\Gamma\}^T[e]\{E\} - \frac{1}{2}\{E\}^T[\varepsilon]\{E\} \quad (2.6)$$

The co-energy density function over the whole domain

$$W_e^*(\Gamma, E) = \int_{\Omega} \left( \frac{1}{2}\{\Gamma\}^T[s]\{\Gamma\} - \{\Gamma\}^T[e]\{E\} - \frac{1}{2}\{E\}^T[\varepsilon]\{E\} \right) d\Omega \quad (2.7)$$

The first part  $\frac{1}{2}\{\Gamma\}^T[s]\{\Gamma\}$  is the strain energy,  $\frac{1}{2}\{E\}^T[\varepsilon]\{E\}$  is the electrical energy and  $\{\Gamma\}^T[e]\{E\}$  is the electromechanical coupling energy. Similarly the kinetic energy term is given by the co-energy density function over the whole domain

$$T^* = \int_{\Omega} \frac{1}{2}\rho\{\dot{u}\}^T\{\dot{u}\} d\Omega \quad (2.8)$$

Now the electric displacement is given by

$$\{D\} = \left\{ \frac{\partial W_e^*}{\partial E} \right\} \quad (2.9)$$

and stress

$$\{\sigma\} = -\left\{ \frac{\partial W_e^*}{\partial \Gamma} \right\} \quad (2.10)$$

The coupled equation for piezoelectric materials are described below

$$\{\Gamma\} = [C]\{\sigma\} + [d]^T\{E\} \quad (2.11)$$

$$\{D\} = [d]\{\sigma\} + [\varepsilon]^T\{E\} \quad (2.12)$$

$[C]$  is the compliance matrix,  $[d]$  is the piezoelectric strain coefficient,  $[\varepsilon]$  is the dielectric field.

The coordinate system used to describe the orthotropic directions is shown in Figure 2.4

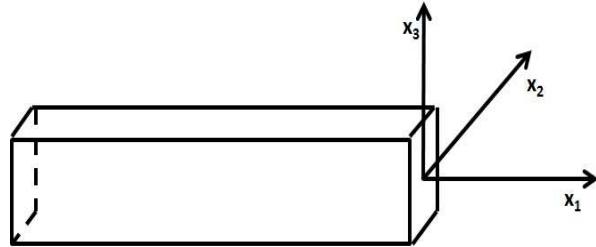


Figure 2.4: Coordinate direction along which the material properties are prescribed.

During actuation or converse piezoelectric effect, the relation becomes,

$$\left\{ \begin{array}{l} \Gamma_{11} \\ \Gamma_{22} \\ \Gamma_{33} \\ 2\Gamma_{23} \\ 2\Gamma_{13} \\ 2\Gamma_{12} \end{array} \right\} = \left[ \begin{array}{cccccc} C_{11} & C_{12} & C_{13} & 0 & 0 & 0 \\ C_{21} & C_{22} & C_{23} & 0 & 0 & 0 \\ C_{31} & C_{32} & C_{33} & 0 & 0 & 0 \\ 0 & 0 & 0 & C_{44} & 0 & 0 \\ 0 & 0 & 0 & 0 & C_{55} & 0 \\ 0 & 0 & 0 & 0 & 0 & C_{66} \end{array} \right] \left\{ \begin{array}{l} \sigma_{11} \\ \sigma_{22} \\ \sigma_{33} \\ 2\sigma_{23} \\ 2\sigma_{13} \\ 2\sigma_{12} \end{array} \right\} + \left[ \begin{array}{cccccc} d_{11} & d_{12} & d_{13} & 0 & 0 & 0 \\ 0 & 0 & 0 & 0 & 0 & d_{26} \\ 0 & 0 & 0 & 0 & d_{35} & 0 \end{array} \right]^T \left\{ \begin{array}{l} E_{11} \\ E_{22} \\ E_{33} \end{array} \right\} \quad (2.13)$$

During sensing or direct piezoelectric effect, the relation becomes,

$$\left\{ \begin{array}{l} D_1 \\ D_{22} \\ D_{33} \end{array} \right\} = \left[ \begin{array}{cccccc} d_{11} & d_{12} & d_{13} & 0 & 0 & 0 \\ 0 & 0 & 0 & 0 & 0 & d_{26} \\ 0 & 0 & 0 & 0 & d_{35} & 0 \end{array} \right] \left\{ \begin{array}{l} \sigma_{11} \\ \sigma_{22} \\ \sigma_{33} \\ 2\sigma_{23} \\ 2\sigma_{13} \\ 2\sigma_{12} \end{array} \right\} + \left[ \begin{array}{ccc} \varepsilon_{11} & 0 & 0 \\ 0 & \varepsilon_{22} & 0 \\ 0 & 0 & \varepsilon_{33} \end{array} \right] \left\{ \begin{array}{l} E_{11} \\ E_{22} \\ E_{33} \end{array} \right\} \quad (2.14)$$

## 2.6 Results & Discussions

### 2.6.1 Effective Material Properties estimation and comparison

The unit cell homogenisation is done for different fiber volume fractions and the results are plotted in Figure 2.5.

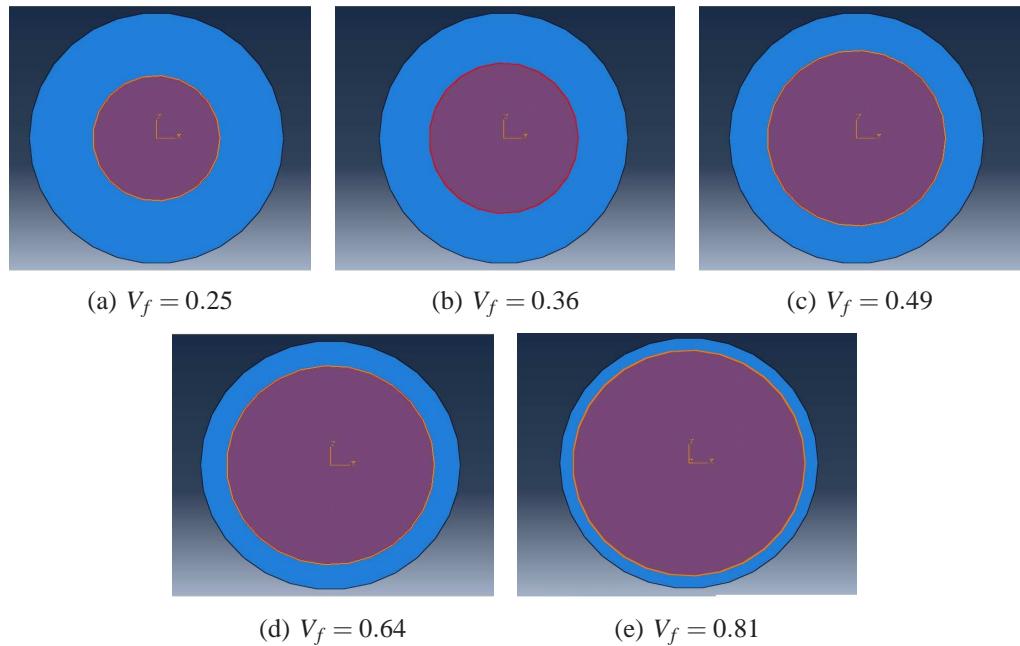


Figure 2.5: Piezofiber Matrix Composite with different Fiber Volume fraction

The material constants of fiber and matrix are

**Table 2.1: Material Constants**

Material	$E_1$	$E_2$	$E_3$	$G_{12}$	$G_{13}$
PZT 5A	6.09E+10	6.09E+10	5.32E+10	2.26E+10	2.11E+10
Epoxy	1.51E+09	1.51E+09	8.06E+08	6.45E+8	6.45E+8

**Table 2.2: Material Constants**

Material	$G_{23}$	$\nu_{12}$	$\nu_{13}$	$\nu_{23}$	Density
PZT 5A	2.11E+10	3.51E-01	4.40E-01	4.40E-01	7.75E+03
Epoxy	6.45E+8	1.68E-01	7.48E-01	7.48E-01	1.40E+03

**Table 2.3: Material Constants**

Material	$d_{11}$	$d_{12}$	$d_{13}$	$d_{26}$	$d_{35}$
PZT 5A	328.3752	264.5136	258.824	13.1984	12.3224
Epoxy	0	0	0	0	0

**Table 2.4: Material Constants**

Material	$e_{11}$	$e_{22}$	$e_{33}$
PZT 5A	1.537E-8	1.537E-8	1.537E-8
Epoxy	0.5314E-10	0.5314E-10	0.5314E-10

The effective values of the material constants for different fiber volume fractions generated from the VAMUCH.

Table 2.5: Effective Material Properties

$V_f$	$E_1$	$E_2$	$E_3$	$G_{12}$	$G_{13}$
2.50E-01	2.14E+10	5.16E+08	4.96E+08	2.76E+08	3.34E+08
3.60E-01	3.02E+10	5.57E+08	5.57E+08	2.90E+08	3.63E+08
4.90E-01	4.06E+10	6.37E+08	6.49E+08	3.21E+08	4.02E+08
6.40E-01	5.25E+10	7.76E+08	7.68E+08	3.62E+08	4.48E+08
8.10E-01	6.60E+10	9.84E+08	1.16E+09	4.14E+08	5.72E+08

Table 2.6: Effective Material Properties

$V_f$	$G_{23}$	$v_{12}$	$v_{13}$	$v_{23}$	Effective Density
2.50E-01	2.23E+08	3.23E-01	6.65E-01	7.33E-02	2.99E+03
3.60E-01	2.27E+08	3.74E-01	6.50E-01	3.54E-02	3.69E+03
4.90E-01	2.48E+08	4.29E-01	6.40E-01	1.39E-02	4.51E+03
6.40E-01	2.74E+08	4.82E-01	6.41E-01	6.45E-03	5.47E+03
8.10E-01	3.59E+08	5.27E-01	6.56E-01	7.71E-03	6.55E+03

Table 2.7: Effective Material Properties

$V_f$	$d_{11}$	$d_{12}$	$d_{13}$	$d_{26}$	$d_{35}$
2.50E-01	30.59	0.1496	0.1712	1.04E-04	1.56E-04
3.60E-01	44.08	0.2426	0.2823	1.46E-04	2.35E-04
4.90E-01	60.063	0.395	0.4589	2.23E-04	3.56E-04
6.40E-01	78.55	0.651	0.726	3.52E-04	5.47E-04
8.10E-01	99.73	1.0561	1.4093	6.07E-04	1.17E-03

Table 2.8: Effective Material Properties

$V_f$	$e_{11}$	$e_{22}$	$e_{33}$
2.50E-01	1.82E-07	2.27E-07	2.76E-07
3.60E-01	2.63E-07	2.39E-07	3.01E-07
4.90E-01	3.58E-07	2.66E-07	3.34E-07
6.40E-01	4.68E-07	3.01E-07	3.74E-07
8.10E-01	5.91E-07	3.46E-07	4.83E-07

The effective properties obtained from rules of mixtures are.

Table 2.9: Effective Material Properties

$V_f$	$E_1$	$E_2$	$G_{12}$	$\nu_{12}$
2.50E-01	1.64E+10	2.00E+09	8.52E+8	2.14E-01
3.60E-01	2.29E+10	2.33E+09	9.92E+8	2.34E-01
4.90E-01	3.06E+10	2.89E+09	1.23E+9	2.58E-01
6.40E-01	3.95E+10	4.02E+09	1.71E+9	2.85E-01
8.10E-01	4.96E+10	7.19E+09	3.03E+9	3.16E-01

The effective homogenised material constants generated from the VAMUCH are plotted with fiber volume fraction. The upper bound and the lower bound of the modulus values are fiber properties and matrix properties respectively. But it is observed that the effective stiffness in the longitudinal direction increases beyond the fiber property which means the property are augmented with the combination. The properties such as Young's Modulus in longitudinal and transverse direction and the major Poisson ratio are compared with that generated from Rules of Mixtures hypothesis.

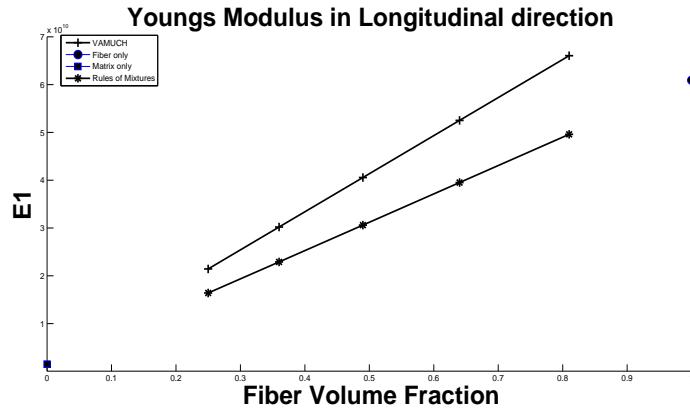


Figure 2.6: Young's Modulus in Longitudinal Direction

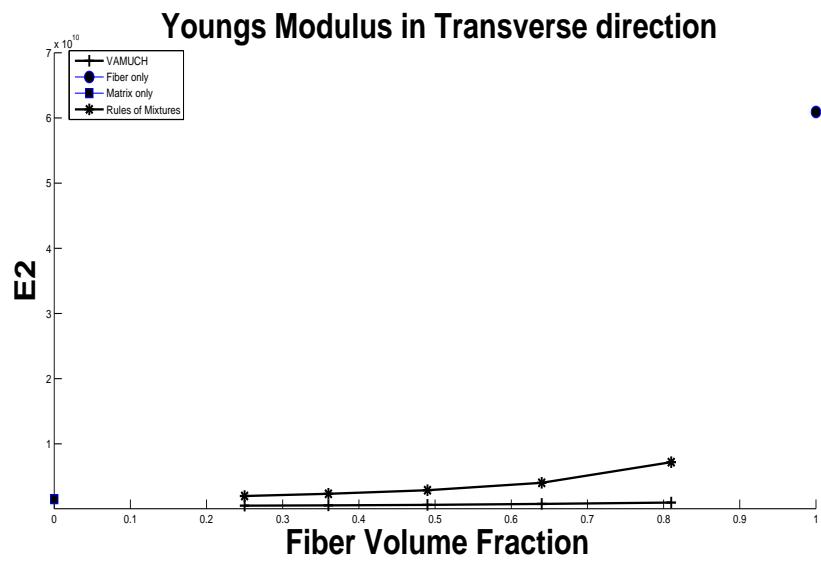


Figure 2.7: Young's Modulus in Transverse Direction

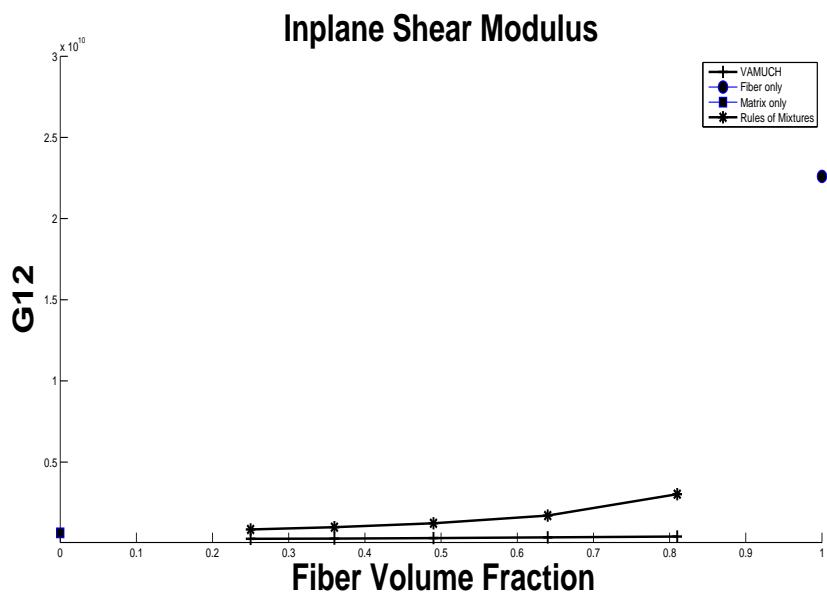


Figure 2.8: Inplane Shear Modulus

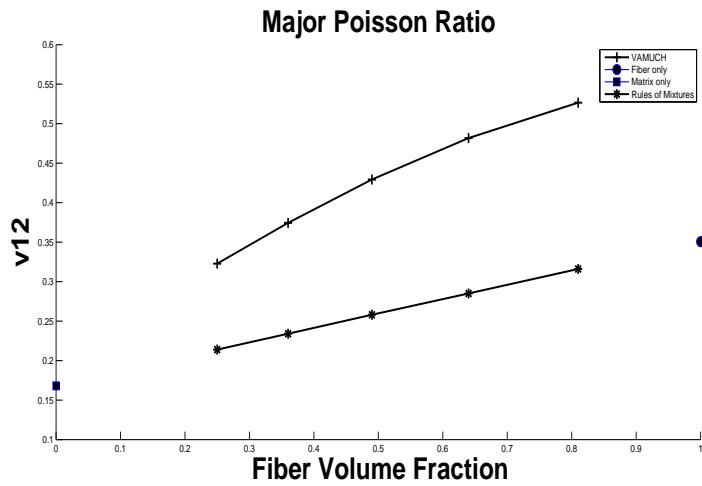


Figure 2.9: Major Poisson Ratio

The Young's Modulus in Transverse direction and Transverse Shear Modulus and the minor Poisson ratios calculated with VAMUCH are plotted with fiber volume fraction. The effective density variation with increase in fiber volume ratio is also shown.

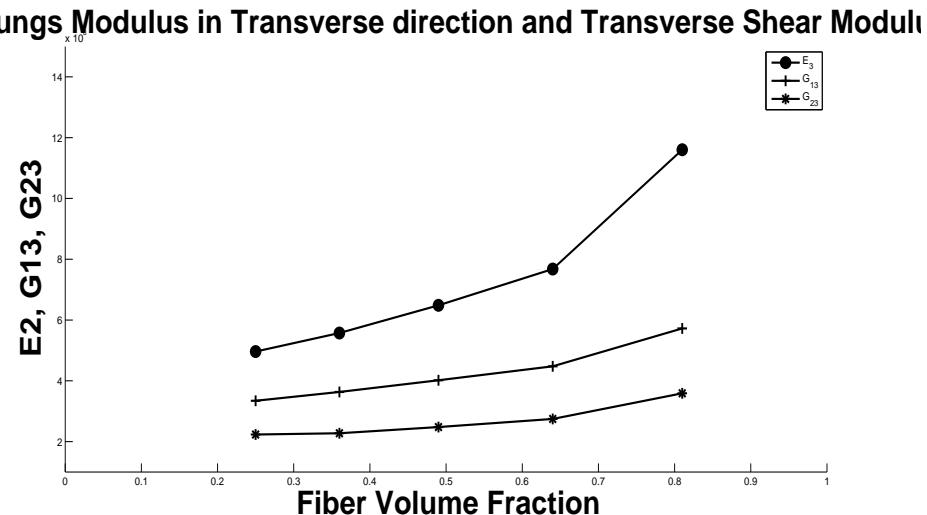


Figure 2.10: Young's Modulus in Transverse direction and Transverse Shear Modulus

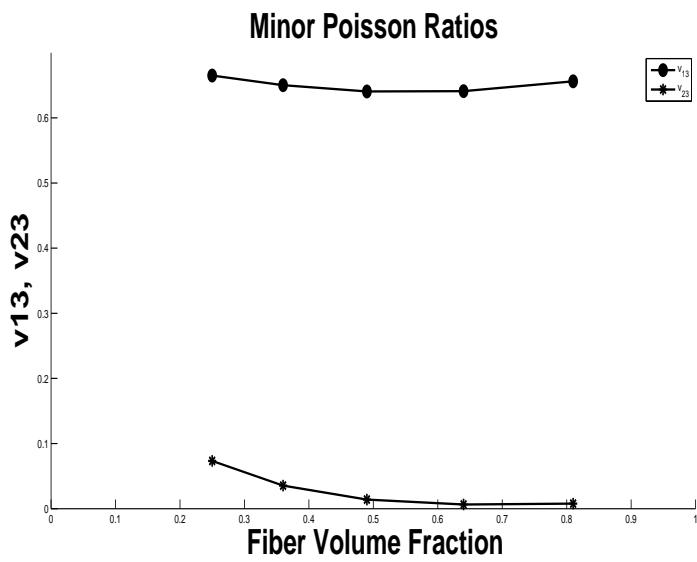


Figure 2.11: Minor Poisson Ratios

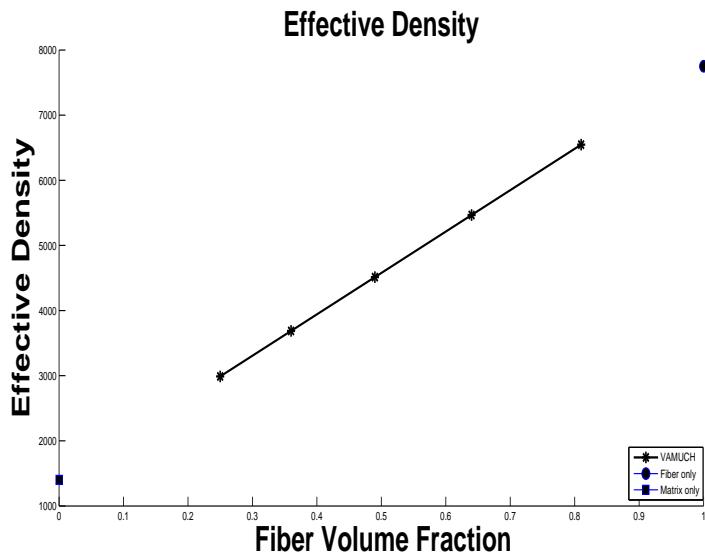


Figure 2.12: Effective Density

## 2.6.2 Validation study

A validation study is conducted using a PZT 5A - Epoxy unit cell of dimension  $10 \times 10 \times 100 \text{ mm}^3$ . A transverse force of amount  $10^7$  is applied at one of its boundary keeping the other boundary fixed. The study is conducted with a fiber volume fraction of 0.196. The stress values obtained from VAMUCH and Abaqus is given below.

Table 2.10: Recovered Stress

Recovered Stress	$\sigma_{11}$	$\sigma_{22}$	$\sigma_{33}$
Abaqus	-9.50E+06	-3.00E+06	-3.00E+06
VAMUCH	-1.31E+07	-3.98E+06	-4.92E+06

Table 2.11: Recovered Stress

Recovered Stress	$\sigma_{12}$	$\sigma_{13}$	$\sigma_{23}$
Abaqus	-2.80E+06	1.80E+06	-5.90E+05
VAMUCH	-2.12E+05	1.47E+06	-5.11E+05

The resultant displacement developed in the model is shown in Figure 2.13 .

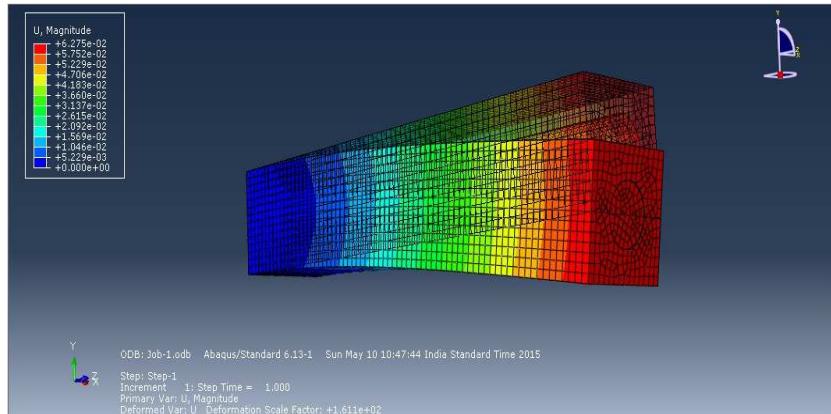


Figure 2.13: Fiber matrix model with transverse concentrated force at the tip

### 2.6.3 Results obtained with practical loads cases

An electromechanical analysis is done using a PZT 5A - Epoxy unit cell of dimensions  $10 \times 10 \times 100 \text{ mm}^3$  using Abaqus. The load acting on the helicopter blade, obtained from 1, and are considered for the calculations. The drag load is of value  $6.67 \text{ N/m}$ . The centrifugal load linearly varies from root to tip as  $7018.4 Z \text{ N/m}$  as  $Z$  varies from 0 to 1 for our case. Similarly for thrust load, a quadratic variation,  $-774.0 Z^2 + 2217.4 Z - 21.04 \text{ N/m}$  is used.

The different loads employed for analysis are shown in Figure 2.14 .

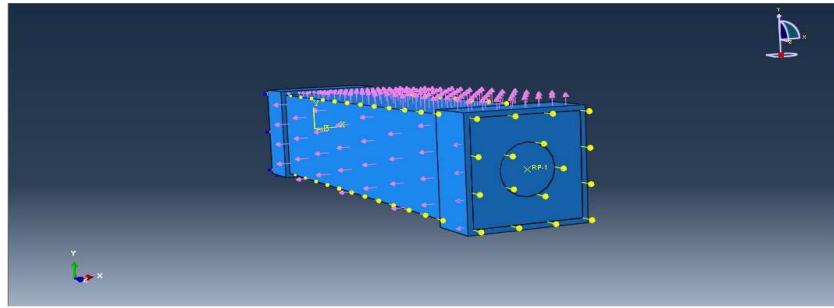


Figure 2.14: Centrifugal, thrust and drag loads on the unit cell model.

A dynamic load with frequency of  $20 \text{ Hz}$  is applied to evaluate the electrical energy generation.

The macro displacements are obtained using Abaqus is given as input to VAMUCH for getting the local point wise stresses, strains, displacements, electric fields and electric displacements. The results obtained for the macro properties at the tip of the model is given in tables 2.12 and 2.13.

The maximum stress values recovered from Abaqus and VAMUCH is given below.

Table 2.12: Recovered Stress

Recovered Stress	$\sigma_{11}$	$\sigma_{22}$	$\sigma_{33}$
Abaqus	1.69E+05	6.9E+04	5.87E+04
VAMUCH	1.4E+05	3.46E+04	3.4E+04

Table 2.13: Recovered Stress

Recovered Stress	$\sigma_{12}$	$\sigma_{13}$	$\sigma_{23}$
Abaqus	6.4E+04	5.4E+04	1.3E+04
VAMUCH	3.4E+04	3.4E+04	0.86E+04

We have done the analysis considering the model in sensor mode. With the applied loads, electric fields and electric displacements are generated other than stresses and strains. From the electric properties, we can easily determine the amount of charges accumulated in the specimen.

The variation of the electric displacement (in  $C/m^2$ ) and electric field (in  $C/N$ ) with time (in second) are shown in Figure 2.15 and Figure 2.16 respectively.

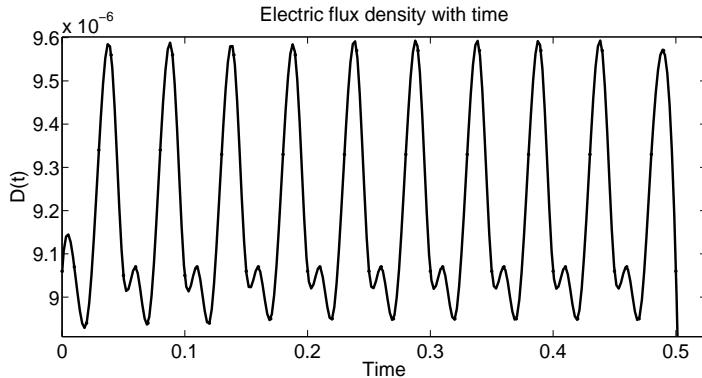


Figure 2.15: Variation of Electric flux density with time

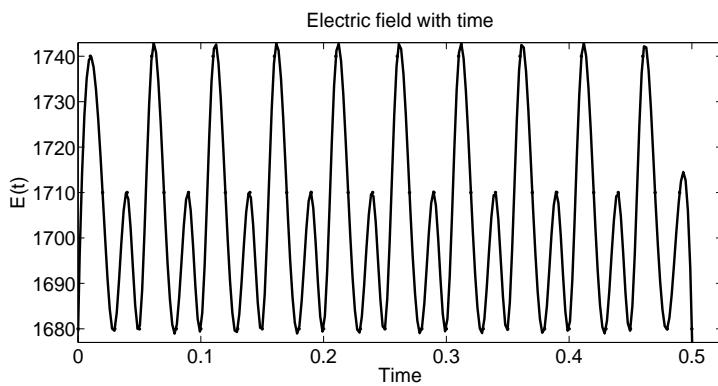


Figure 2.16: Variation of Electric field with time

The dielectric constant,  $\epsilon$  for the material is given by

$$\epsilon = \frac{D_1}{E_1} \quad (2.15)$$

From the results,

$$e = 5.4 * 10^{-9} C^2 N^{-1} m^{-2} \quad (2.16)$$

The electric displacement is equivalent to the free charge developed per unit area of a capacitor. Assuming the given model to be a capacitor with plates situated at the electrode locations as sketched in the Figure 2.17.

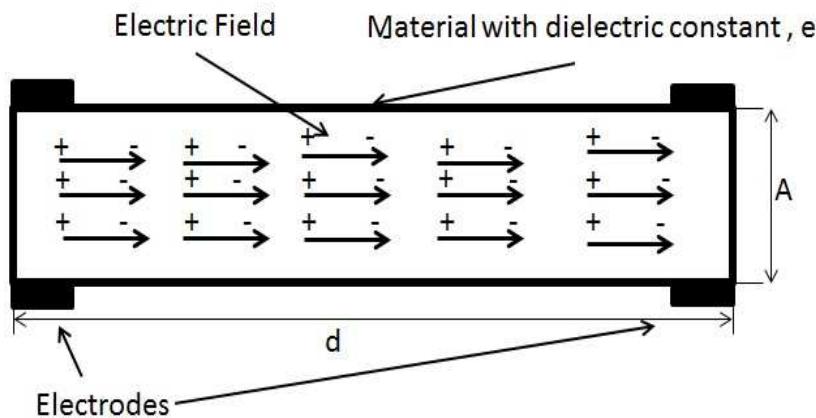


Figure 2.17: Capacitor model for unit cell

From this model, we can get a reasonable estimate of the quantity of free charges accumulated in the model. Thus the charge (in *Coulomb*) generated with time (in *second*) is shown in the Figure 2.18.

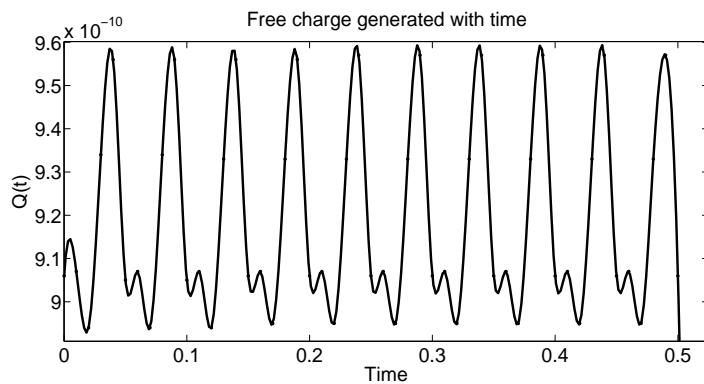


Figure 2.18: Variation of Charge generation with time

The capacitance, C of the model is given by the expression,

$$C = \frac{eA}{d} \quad (2.17)$$

where A being the capacitor plate area and d, the distance between the plates. Here, A is same as the cross sectional area and d, the length of the unit cell. Taking

$$A = 10^{-4} m^2 \quad (2.18)$$

$$d = 10^{-1} m \quad (2.19)$$

So the capacitance,

$$C = 5.4 * 10^{-12} \text{ farad} \quad (2.20)$$

The electric potential is given by,

$$V = \frac{Q}{C} \quad (2.21)$$

The variation of electric potential (in *volt*) with time (in *second*) is given in the Figure 2.19

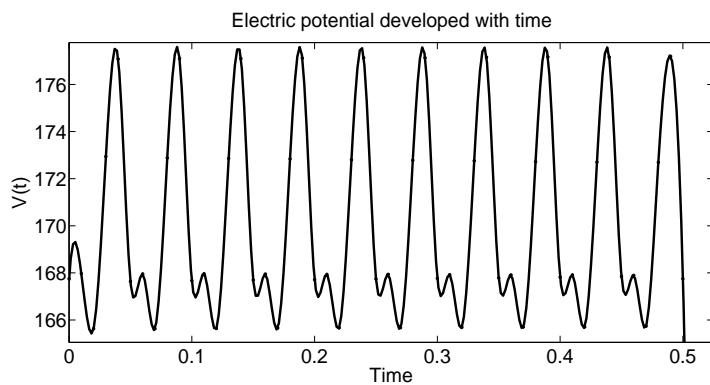


Figure 2.19: Variation of Electric Potential with time

The electrostatic energy density(in  $J/m^3$ ) produced in the model with time(in *second*) is shown in Figure 2.20

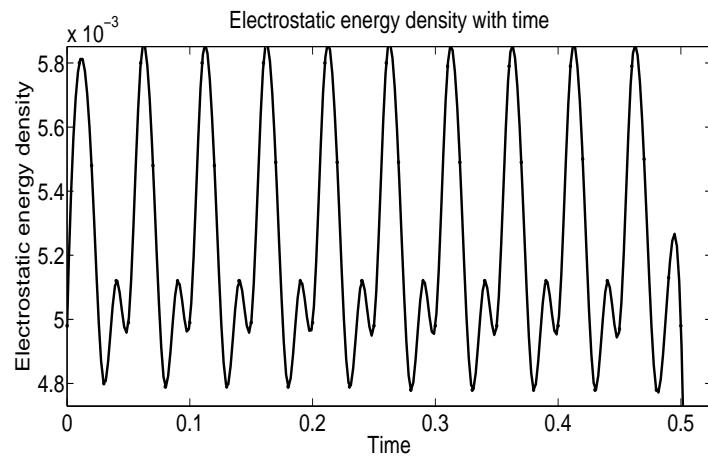


Figure 2.20: Variation of Electrostatic energy density with time

# Chapter 3

## Helicopter Blade: Structural Design and Analysis

### 3.1 Introduction

The most important structural component of a Rotary Unmanned Aerial Vehicle (RUAV) is the main rotor blades. The rotor blades provide the thrust as well as the lift to the entire vehicle. The design of the rotor blade involves extensive knowledge of structures, aerodynamics, fatigue, dynamics, manufacturing and optimisation. The deflection of the rotor blade will affect the airflow over the blade. The strong coupling between aerodynamic loads and structural deformation makes its design and analysis a complicated Fluid Structure Interaction (FSI) problem. Figure [3.1] shows the cross-section a typical helicopter rotor blade.

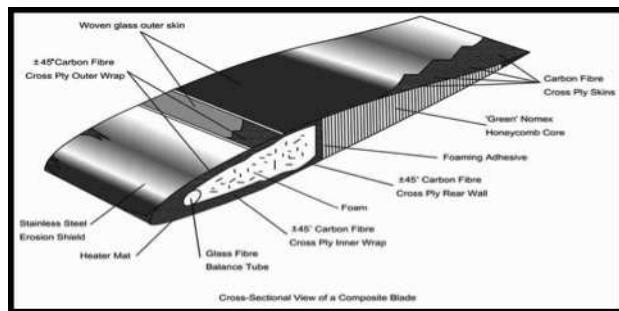


Figure 3.1: A typical rotor blade cross-section

### **3.1.1 Background**

Rotor blades are made up of composite materials to ensure the high strength to weight ratio. The damage tolerance and fatigue properties of composites are superior compared to those of metals. Another interesting aspect of the composites is their anisotropy, where designer has all the freedom to tailor the stiffness of the structure. The main theme of the present work is to tailor the stiffness and weight of the composite while simultaneously meeting the mission requirements. The major challenges in the blade design are observed in designing the airfoil cross-section and addressing nonlinearities associated with the finite large deformation along the span of the blade. The computation of the stiffness for this sectional profile is cumbersome and presence of nonlinear 1D behaviour made way to the development of many computationally intensive nonlinear solutions.

### **3.1.2 Literature Survey**

Different beam theories are available in the literature to analyse helicopter rotor blades. According to Hodges, the beam theories are classified broadly into five categories. Firstly, ad-hoc beam theories which are based on the ad-hoc corrections made on existing simpler theory. Extension of the theory by Houbolt and Brooks (1958) is an example for this theory. Next set of the beam theories are based on the ordering of the pertinent variables. This theory is simpler to hold quadratic nonlinearity. Examples of this kind of theory may be found in Hodges and Dowell (1974), Kaza and Kvaternik (1977), Rosen and Friedmann (1978), Crespo da Silva and Hodges (1986), and Rosen et al. (1986). Engineering theories based on the small strain approximation emphasise that the ordering of the pertinent variables are based on the smallness of the strain without any approximations on the rotation. Next class termed as Director beam theories in which there is a decomposition of the problem into 2D analysis and 1D analysis without any justification. Erickson and Truesdell (1958), Green and Laws (1966), Cohen (1966), and Whitman and DeSilva (1969) have presented the examples of this theory.

## **3.2 Theoretical Approach**

The primary objective of this study is to analyze the rotor blade configuration for the given loads. Variational Asymptotic Method (VAM) is proposed for the design and analysis of this kind of problem along with certain optimisation algorithms. VAM makes use of the certain small parameters that are inherent to the physics and geometry of the given system and then it decouples the original 3D slender solid with complex microstructure (sophisticated cross-section with or without span-wise heterogeneity) into a simple engineering

beam model consisting of 2D analysis & 1D analysis. Fig [3.2] shows undeformed & deformed beam geometries considered in the VAM formulation.

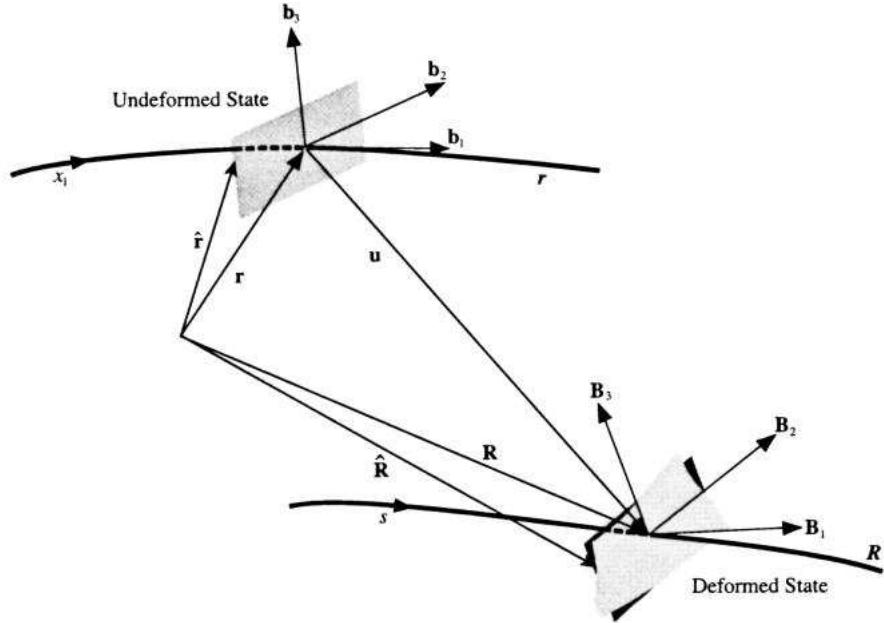


Figure 3.2: Undeformed & deformed geometries in VAM formulation

The 2D cross sectional analysis yields the 1D constitutive law, which relates the cross-sectional stress resultants and 1D generalised strains. This acts as the input for the 1D analysis. Variational Asymptotic Beam Sectional analysis(VABS) is used for cross-sectional analysis. VABS is a general-purpose tool for computing beam cross-sectional properties and recovering 3D fields of slender composite structures. With continuous development spanning over 15 years for performance and robustness, VABS is highly regarded in industry as a mature product. Furthermore, VABS accuracy has been extensively verified by its developers and users. The 1D analysis is carried out using an in-house code developed in IISc.

### 3.2.1 Design of Rotor Blade Cross-section

In rotor blade structural design, it is prevalent in the literature to assume a specific topology of structural components inside a given airfoil shape. This sort of assumption reduces

the problem to a sizing optimizaton in which one varies various parameters like dimensions, orientations, and locations of structural components to achieve the desired sectional properties. In this study, the multi-objective problem is formulated to obtain an optimal cross-section design. Here the objective is to minimize the weight and maximisation the stiffness. The parameters considered in the design optimisation are ply thickness, number of plies, web location along the chord and percentage of Carbon Nano Tube (CNT) doped.

The stiffness of the cross section varies with the thickness and as the thickness of the section along the bending axis or torsional axis increases, the beam becomes stiffer along those axes. Also the stiffness of the structure is tailored by varying the ply angles, ply thickness and number of plies. To further improve the stiffness characteristics, Carbon Nano Tube particles are added to the material. Here the percentage of the CNT is also considered as the variable.

The minimum ply thickness that is manufactured by HexCel technologies is 0.018mm and is considered as a reference for ply thickness base value. The variations of the thickness are assumed in the order of 10 mm on either side of the base value. Considering a symmetric ply angle configuration, following layup is considered for modeling the skin of the airfoil:

$$[0^0][0^0/45^0/-45^0/0^0]_m[0^0]$$

The effective modulus of the lamina after CNT doping is obtained by the general rule of mixtures. To estimate the range of the web-location a preliminary analysis is performed.

### 3.3 Structural Analysis Formulation

Rotor blades are modelled as initially curved and twisted cantilever beams. VAM is adopted for analysing this composite beam. According to this approach the complex 3D model is replaced by the reduced order in terms of asymptotic series of certain small parameters inherent to the structure. Therefore the 3D analysis is broken into 2D linear analysis and 1D nonlinear analysis. For the purpose of sectional analysis of the blade VABS 3.0 is used. VABS, as an alternate to 3D FEM and with substantial reduction in computational cost for a given level of accuracy, has the capability of capturing the trapeze and Vlasov effects and calculating the 1D sectional properties with transverse shear refinement for any initially twisted and curved, inhomogeneous, anisotropic beam with arbitrary geometry and material properties. For the 1D nonlinear analysis an inhouse code is used which is developed based on the theory of Geometrically Exact Beam Theory (GEBT). The flow chart of the structural analysis is given in the below Fig [3.3].

### 3.3.1 Cross-Sectional Analysis Formulation

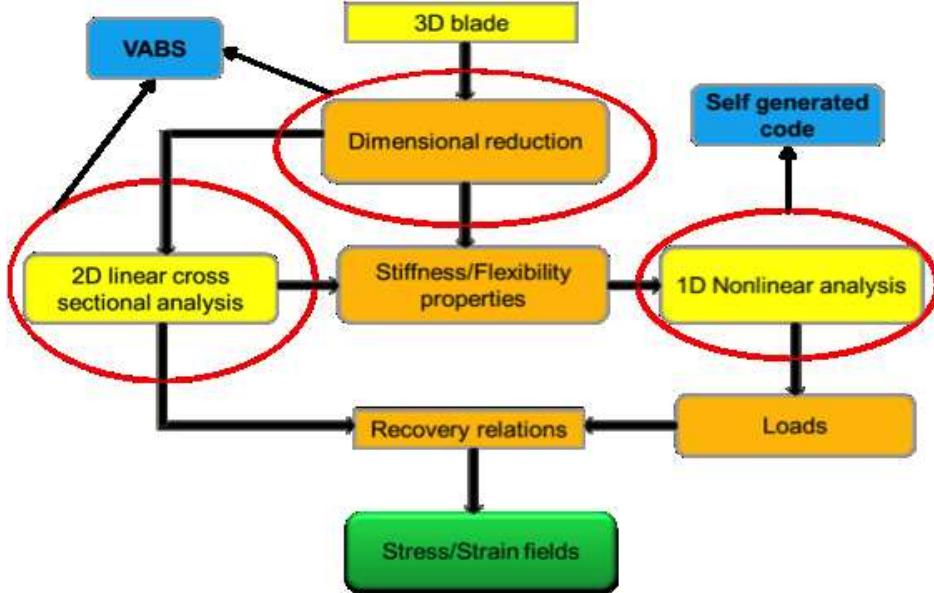


Figure 3.3: Flowchart of Structural Analysis

VABS formulation depends upon minimising the strain energy per unit length of the beam. The 3D strains denoted as  $\Gamma$  have 6 components as shown below:

$$\Gamma = [ \Gamma_{11} \quad 2\Gamma_{12} \quad 2\Gamma_{13} \quad \Gamma_{22} \quad 2\Gamma_{23} \quad \Gamma_{33} ]^T \quad (3.1)$$

The strain energy expression is given in equation [3.2], where  $g$  is the determinant of the metric tensor for the un-deformed state. This strain energy is ordered asymptotically and minimised to calculate warping

$$U = \frac{1}{2} \int_A \Gamma^T D\Gamma \sqrt{g} dx_2 dx_3 \quad (3.2)$$

where,  $x_2$  and  $x_3$  correspond to the orthogonal cartesian coordinates in the cross-section

The strain energy as shown in equation [3.3] can be expressed in terms of a series of asymptotically correct energy terms that correspond to different orders of the small parameter inherent to the beam. To avoid redundancy the three warping terms  $w_i(x_1, x_2, x_3)$ ,

( $i = 1, 2, 3$ ), which are introduced in the VAM formulation to allow for higher order arbitrary 3D deformation, need to satisfy certain constraints. The warping constraints are introduced using Lagrange multipliers in the energy functional.

$$U = U_0 + U_1 + U_2 + \dots \quad (3.3)$$

where  $U_0$ ,  $U_1$ , and  $U_2$  are zeroth-order, first-order, and second-order approximations of the strain energy. The second-order asymptotically correct energy accounts for the effects of initial twist and curvature. Once the first-order approximation of warping function is obtained, the strain energy is asymptotically correct through second-order of approximation and can be expressed in terms of the generalised Timoshenko beam strain measures. By differentiating it with respect to the generalised Timoshenko 1D strain measures, one can obtain the 1D constitutive law and the cross-sectional 1D stiffness matrix, shown below:

$$\begin{bmatrix} F_1 \\ F_2 \\ F_3 \\ M_1 \\ M_2 \\ M_3 \end{bmatrix} = \begin{bmatrix} S_{11} & S_{12} & S_{13} & S_{14} & S_{15} & S_{16} \\ S_{12} & S_{22} & S_{23} & S_{24} & S_{25} & S_{26} \\ S_{13} & S_{23} & S_{33} & S_{34} & S_{35} & S_{36} \\ S_{14} & S_{24} & S_{34} & S_{44} & S_{45} & S_{46} \\ S_{15} & S_{25} & S_{35} & S_{45} & S_{55} & S_{56} \\ S_{16} & S_{26} & S_{36} & S_{46} & S_{56} & S_{66} \end{bmatrix} \begin{bmatrix} \gamma_{11} \\ 2\gamma_{12} \\ 2\gamma_{13} \\ \kappa_1 \\ \kappa_2 \\ \kappa_3 \end{bmatrix} \quad (3.4)$$

where  $F_i$  and  $M_i$  are sectional forces and moments, respectively; and  $\gamma_{1i}$  and  $\kappa_i$ , ( $i = 1, 2, 3$ ) are the 1D generalised strains, twist & curvatures of the beam, respectively. The matrix  $S_{ij}$ , ( $i, j = 1$  to 6) is called the generalised Timoshenko stiffness matrix.

### 3.3.2 Nonlinear Beam Analysis Formulation

After getting 1D stiffness matrix from the cross-sectional analysis, 1D sectional forces & moments are substituted into the following geometrically exact nonlinear 1D equations, equation [3.5,3.6], corresponding to the static problem. These equations are developed in an intrinsic formulation that is not tied to a specific choice of displacement or rotation variables.

$$F' + \tilde{K}F + f = 0 \quad (3.5)$$

$$M' + \tilde{K}M + (\tilde{e}_1 + \tilde{\gamma})F + m = 0 \quad (3.6)$$

where  $(\cdot)'$  denotes the partial derivative with respect to the axial coordinate  $x_1$  and column matrices  $e_1 = [1 \ 0 \ 0]^T$ ,  $F = [F_1 \ F_2 \ F_3]^T$ ,  $M = [M_1 \ M_2 \ M_3]^T$ ,  $\gamma =$

$[\gamma_{11} \ 2\gamma_{12} \ 2\gamma_{13}]^T$ ,  $f = [f_1 \ f_2 \ f_3]^T$ , and  $m = [m_1 \ m_2 \ m_3]^T$ .  $F_i$ ,  $M_i$ ,  $\gamma_{1i}$  &  $\kappa_i$  are as defined before. The distributed loads are denoted by  $f_i$  &  $m_i$ , where ( $i = 1, 2, 3$ ).

Above nonlinear equations are solved using FEM using an in-house code with 30 1D elements and using hermite polynomial shape function to discretise the independent variables  $\gamma$  &  $\kappa$ . After 1D analysis, recovery analysis is performed using VABS so as to obtain 3D stress fields which are the crucial parameters for an optimum design of the helicopter blade.

### 3.4 Base Case Analysis

A preliminary analysis is done for the base case in which the thickness of all the components is assumed to be uniform along the span and following specifications are chosen as shown in Table [3.1]:

Airfoil	NACA 0012
Chord	5 inches
Ply thickness	0.015 inches
Number of plies	5
Ply angles	$45^\circ / -45^\circ / 0^\circ / -45^\circ / 45^\circ$

Table 3.1: Base Case Data Set

The structured mesh is generated using the Pre-VABS, and the meshed model is shown in Fig [3.4]

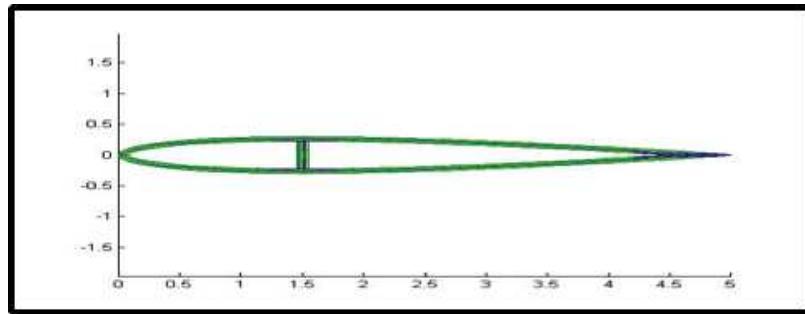


Figure 3.4: Meshed Model

A orthogonal array based design of experiments (DOE) approach, discussed in chapter 4 is used to conduct 18 design runs to obtain the  $l^2$  stiffness norm and structural weight towards an optimal helicopter rotor blade cross-section design. The details of the design parameters and the corresponding stiffness norm and structural weight obtained are shown in Figure 3.5. The details of the formal mathematical optimization routines to obtain the cross-section design is discussed in chapter 4.

S_no	Var1	Var2	Var3	Var4	Stiffness_norm	Weight/unit length
1	-1	-1	-1	-1	30465769092	0.199314328
2	0	0	0	0	1.58943E+11	0.387208738
3	1	1	1	1	3.38318E+11	0.610425294
4	0	0	1	1	2.20935E+11	0.384643137
5	1	1	-1	-1	64425049153	0.612731266
6	-1	-1	0	0	84189051081	0.199699657
7	-1	1	0	1	1.37468E+11	0.324954349
8	0	-1	1	-1	1.64708E+11	0.294487132
9	1	0	-1	0	61517373359	0.504012537
10	1	0	0	-1	2.00453E+11	0.504933426
11	-1	1	1	0	1.88614E+11	0.325515903
12	0	-1	-1	1	45140415843	0.293440886
13	1	-1	1	0	2.14501E+11	0.38696553
14	-1	0	-1	1	34056301650	0.26219295
15	0	1	0	-1	1.91016E+11	0.476080436
16	0	1	-1	0	51654223504	0.475210629
17	1	-1	0	1	1.59284E+11	0.385791899
18	-1	0	1	-1	1.51006E+11	0.263123613
Var1	Thickness				Inputs	
Var2	Number of plies				Stiffness norm	
Var3	% CNT				Weight per unit length	
Var4	Web location					

Figure 3.5: L-18 Table with corresponding stiffness norm & weight per unit length

# Chapter 4

## Design Optimization

### 4.1 Taguchi Method of Design

The Taguchi method of design is a statistical technique that aims to improve the quality characteristic of a product by focussing on the design variables at the design stage itself. It is a fractional factorial design of experiments approach. In the Taguchi method, quality is reflected as consistent performance of a product close to a target value, and reduction in the variation of performance is seen as quality enhancement. As the Taguchi method can efficiently determine the combination of design parameters that lead to an optimum or enhanced performance of a system, with minimum variation in its performance, it is used in several engineering fields to obtain robust design systems [19]. The Taguchi method of design involves two steps:

1. Selecting the values of design parameters such that it results in optimal (or improved) performance, and
2. Making the design robust, in the sense that performance remains insensitive to the influence of uncontrollable factors (noise).

This is carried out by using orthogonal arrays.

Orthogonal arrays are a unique set of tables developed for designing experiments; they represent the smallest fractional factorials which can be used for experiment designs [20]. Orthogonal arrays allow for independently investigating the effect of each design parameter on the performance of the system while carrying out a minimum number of experiments or numerical simulations. Orthogonal arrays are also used to consider uncontrollable variations in design parameter values, also called noise.

Noise factors are factors that affect the performance of the system but cannot be economically controlled. The effect of noise factors on the response of the system under

study is called noise. Noise can be due to both internal and external factors and is seen as variations in design parameter values from the desired values that may arise during manufacturing, finishing process, etc. Influence of environmental and other uncontrollable factors will also lead to noise in design parameters.

The use of orthogonal arrays in the Taguchi method of design consists of following steps:

1. Identification of controllable factors and their levels. Controllable factors are design variables which directly influence the system performance. Factor levels refer to the different discrete values of the design variables that are considered for design of experiments.
2. Selection of appropriate orthogonal array for design parameters. Based on the number of design variables and their levels, an appropriate orthogonal array is selected. Standard orthogonal arrays are used in most of the problems. The orthogonal array used for the design variables is called design parameter matrix or inner array.
3. Selection of appropriate orthogonal array for noise values. Based on the number of design parameters that are influenced by noise factors, and their levels, a suitable orthogonal array is selected to account for noise factors. This orthogonal array is called noise matrix or outer array. There will be one noise matrix for each experiment or simulation in the design parameter matrix.
4. Analysis of system performance. The average performance of the system and the associated 'signal-to-noise ratio',  $S/N$  ratio, is obtained for each experiment or simulation in design parameter matrix based on the output from the noise matrices. The values of  $S/N$  ratios are used to arrive at a robust design of the system.

Signal-to-noise ratio,  $S/N$ , is a variance index. It gives an indication of the variation of the quality characteristic for each experiment or simulation of the design parameter matrix. 'Signal' is defined as "the change in the quality characteristic of the system under investigation in response to a factor introduced in the experimental design" [20]; it is a desired effect, as against noise which is undesired. The  $S/N$  ratio gives a measure of the sensitivity of the system performance to design parameters, relative to the sensitivity of the system performance to the noise factors.  $S/N$  ratio is defined according to problem objective. There are three commonly used  $S/N$  ratios, based on the definition of mean square deviation used:

1. **Smaller-the-better** definition is used in cases where the objective is to minimize the quality characteristic of the system under study. Examples include minimization of shrinkage of cast products, minimization of defects in manufactured products,

minimization of heat generated in an electronic or electrical circuit, minimization of induced stresses in a mechanical system, minimization of vibration in machining systems, etc. The  $S/N$  ratio for smaller-the-better quality characteristic is given by:

$$\frac{S}{N} = -10 \log_{10} \left( \frac{1}{k} \left[ \sum_{i=1}^k (y_i)^2 \right] \right) \quad (4.1)$$

where  $y_i$  is the performance characteristic of the  $i^{th}$  trial in the noise matrix, and  $k$  is the total number of trials in the noise matrix.

2. **Nominal-the-better** is used when the objective is to make the quality characteristic achieve a value as close as possible to a specified target value. Examples where nominal-the-better is used include manufactured products and mechanical fittings, whose dimensions have to be consistently close to a nominal value; ratios of chemicals or mixtures which constitute as the ingredients in a chemical compound; thickness of material deposition or material removal in processes such as electroplating, etching, etc. The  $S/N$  ratio for nominal-the-better quality characteristic is given by:

$$\frac{S}{N} = -10 \log_{10} \left( \frac{1}{k} \left[ \sum_{i=1}^k (y_i - y_0)^2 \right] \right) \quad (4.2)$$

where  $y_0$  is the specified target (nominal) value.

3. **Larger-the-better** is used when the objective is to maximize the quality characteristic of the system. Examples are maximizing the life expectancy of a product, maximizing the power output of a power generating system, maximizing the range of an aircraft, etc. The  $S/N$  ratio for nominal-the-better quality characteristic is given by:

$$\frac{S}{N} = -10 \log_{10} \left( \frac{1}{k} \left[ \sum_{i=1}^k \left( \frac{1}{y_i} \right)^2 \right] \right) \quad (4.3)$$

Irrespective of the definition of  $S/N$  ratio, the combination of design parameters for which the  $S/N$  ratio is highest, will always correspond to the best performance with least variation in performance under the given noise conditions. Thus, the aim of any experiment or simulation is to determine the highest possible  $S/N$  ratio. Higher values of  $S/N$  ratios implies higher signal than noise values, i.e., the system is less sensitive to noise factors and thus, uncontrollable factors will not cause large variation in performance of the system.

## **4.2 Robust Design of Unmanned Helicopter Rotor for Hover Using Taguchi Method**

The robust design of the advanced R-MAX helicopter using Taguchi method is described in the following sections. The objective of the parameter design stage is to determine the values of design parameters that lead to improved hover performance. Noise values are considered for each of the design parameters to ensure robustness of the design.

### **4.2.1 Design Parameters and Noise Factors**

Based on the expression for the power required for a hovering helicopter, 4 main-rotor parameters are selected as design variables: blade radius, chord length at blade tip (along with blade taper, these capture the blade planform variation), unit linear twist of the blade, and the rotor speed. Three levels of the design parameters are considered. The chord length at the blade tip is also used for determining the rotor blade shape. At level 1, the blade is of constant chord whereas it has a linear taper at levels 2 and 3, while keeping the having equal planform areas at all three levels.

Noise values are introduced for each design parameters to analyze the sensitivity of performance to noise factors. Following the method adopted in [19], realistic tolerance of the design parameters have been assumed as noise values.

The values of the design parameters at the three levels along with the noise levels for each design parameter are given in Table (4.1).

### **4.2.2 Parameter Design Using Taguchi Method**

The parameter design using Taguchi method involves the use of two matrices - the design parameter matrix (inner array) and the noise matrix (outer array). In this section, 4 design parameters, at 3 levels, are considered. Therefore, the appropriate orthogonal array for design parameter matrix is the standard  $L_9(3^4)$  orthogonal array. For the noise matrix, which has 4 variables at 2 levels, the closest standard OA is the standard  $L_8(2^7)$  array. The naming convention for OAs is  $L_x(y^z)$ ; where,  $z$  represents the number of design parameters being considered,  $y$  represents the number of levels of the design parameters, and  $x$  represents the number of rows in the OA, i.e. the number of numerical experiments or simulations that are to be carried out.

The design parameter matrix and the noise matrix are obtained by substituting the actual values of the design parameter levels and noise levels in Tables (4.2) and (4.3), respectively. For the design parameter matrix, '1' corresponds to least factor level of the design variables, i.e. level 1, and '2' corresponds to the middle factor level, i.e. level 2,

and '3' corresponds to the highest factor level, i.e. level 3. The design parameter matrix is given in Table (4.4).

Each experiment in the design parameter matrix has a corresponding noise matrix. Since, the design parameter matrix has 9 experiments, there will be 9 corresponding noise matrices. As only 4 noise factors are considered, only the first 4 columns of the  $L_8(2^7)$  OA are considered for constructing the noise matrices. In the present work, tolerance values of design parameters are considered as noise values. The noise matrix, for each parameter design experiment, is constructed by adding the tolerance values of the design parameters to the corresponding design parameter values. The lower tolerance is used for '1' and the upper tolerance is used for '2', to populate the noise matrix. For the 1<sup>st</sup> experiment, the design parameter values along with their noise values, (i.e. tolerance), are:

- A: Rotor radius =  $1.5 \pm 0.005 \text{ m}$
- B: Tip chord =  $0.14 \pm 0.005 \text{ m}$
- C: Blade linear twist =  $-5^\circ \pm 1^\circ$
- D: Rotor speed =  $760 \pm 5 \text{ rpm}$

Now, the noise matrix for the 1<sup>st</sup> experiment is constructed by adding the tolerance values to the design parameter values. The hover power required for each simulation, as calculated is also presented in Table (4.5). Similarly the noise matrices for parameter design experiments 2 through 9, are obtained.

The values of the power required to hover, obtained from the simulations of the noise matrices, are used to compute the  $S/N$  ratios for each parameter design experiment. For each of the 9 parameter design experiments in inner array, 8 simulations are carried out in their corresponding outer arrays. Thus, a total of  $(9 \times 8 =) 72$  simulations are carried out. Since the objective of this study is to minimize the power, smaller-the-better definition is used to compute the  $S/N$  ratios. The robust design with the best hover performance will correspond to the combination of design parameters that will lead to the highest value of  $S/N$  ratio.

The mean power required to hover and the  $S/N$  ratios computed for each parameter design experiment are tabulated in Table (4.6). From Table (4.6) it is clear that the 5<sup>th</sup> numerical experiment of the design parameter matrix corresponds to the highest  $S/N$  ratio and also the lowest mean power required to hover. These results indicate that the design parameter setting:  $A_2$ ,  $B_2$ ,  $C_3$  and  $D_1$ , correspond to the robust configuration of the helicopter which has the least power consumption during hover. Table (4.7) gives a comparison of the main rotor parameters and the hover performance between the baseline - Yamaha R-MAX helicopter and the obtained robust advanced R-MAX helicopter designs. The robust design demonstrates improved hovering efficiency of about 10%.

Table 4.1: Design parameters, levels and noise values

Design variables		Units	Level-1	Level-2	Level-3	Noise value
A	Rotor radius	m	1.5	1.75	2.0	$\pm 0.005$
B	Tip chord	m	0.14	0.12	0.10	$\pm 0.005$
C	Blade linear twist	degrees	-5	-7.5	-10	$\pm 1$
D	Rotor speed	rpm	760	830	900	$\pm 5$

 Table 4.2: Standard  $L_9(3^4)$  orthogonal array

Experiment Number	Parameters			
	A	B	C	D
1	1	1	1	1
2	1	2	2	2
3	1	3	3	3
4	2	1	2	3
5	2	2	3	1
6	2	3	1	2
7	3	1	3	2
8	3	2	1	3
9	3	3	2	1

 Table 4.3: Standard  $L_8(2^7)$  orthogonal array

Simulation	Parameters						
	P1	P2	P3	P4	P5	P6	P7
1	1	1	1	1	1	1	1
2	1	1	1	2	2	2	2
3	1	2	2	1	1	2	2
4	1	2	2	2	2	1	1
5	2	1	2	1	2	1	2
6	2	1	2	2	1	2	1
7	2	2	1	1	2	2	1
8	2	2	1	2	1	1	2

Table 4.4: Design parameter matrix: Inner array  $L_9(3^4)$ 

Experiment Number	Rotor radius A (m)	Tip chord B (m)	Blade linear twist C (degrees)	Rotor speed D (rpm)
1	1.5	0.14	-5	760
2	1.5	0.12	-7.5	830
3	1.5	0.10	-10	900
4	1.75	0.14	-7.5	900
5	1.75	0.12	-10	760
6	1.75	0.10	-5	830
7	2.0	0.14	-10	830
8	2.0	0.12	-5	900
9	2.0	0.10	-7.5	760

 Table 4.5: Noise matrix for 1<sup>st</sup> experiment: Outer array  $L_8(2^4)$ 

Simulation Number	Rotor radius $R(m)$	Tip chord $c_{tip}(m)$	Blade linear twist $\theta_{tw}(\circ)$	Rotor speed $\Omega(rpm)$	Hover power P (KW)
1	1.495	0.135	-6	755	9.0981
2	1.495	0.135	-6	765	9.136
3	1.495	0.145	-4	755	9.2811
4	1.495	0.145	-4	765	9.3243
5	1.505	0.135	-4	755	9.1664
6	1.505	0.135	-4	765	9.2072
7	1.505	0.145	-6	755	9.1527
8	1.505	0.145	-6	765	9.1963

Table 4.6: Results of 9 parameter design experiments

Experiment No.	Mean Power (kW)	S/N Ratio
1	9.1953	-19.2715
2	9.2872	-19.358
3	9.4079	-19.4702
4	10.5368	-20.4554
5	8.6623	<b>-18.7532</b>
6	9.3124	-19.3822
7	11.1095	-20.9159
8	12.3002	-21.8008
9	9.2248	-19.3006

Table 4.7: Comparison of baseline helicopter design with robust design

Design parameter	Rotor radius	Tip chord	Root chord	Blade linear twist	Rotor speed	Hover power	Figure of merit
Symbol	$R$	$c_{tip}$	$c_{root}$	$\theta_{tw}$	$\Omega$	$P_T$	$FM$
Units	m	m	m	degrees	rpm	kW	-
Baseline	1.558	0.138	0.138	0	830	9.6034	0.586
Robust	1.75	0.12	0.16	-10	760	8.6623	0.671

## **4.3 Evolutionary Algorithms Inspired Multi-Objective Optimization**

In this section, optimal design of rotor blade cross-section is explored to simultaneously achieve maximum stiffness and minimum weight inclusion. Surrogate models are developed using design of experiments based on response surface methodology (RSM). Second order polynomial response surfaces are generated by solving the structural analysis using variational asymptotic method (VAM) 3 using a sparse set of design points based on three-level design orthogonal arrays (OA). A new orthogonal array known as MGB4P-OA is used to construct the nonlinear response surfaces with full interaction terms till second order. Pareto analysis is employed in conjunction with a newly developed nature inspired multi-objective bat algorithm (MOBA). Optimal rotor blade cross-section is obtained for mutually conflicting objectives of maximum stiffness and minimum structural weight.

Determining optimal thickness of a ply, number of plies, percentage of carbon nanotubes (CNTs) inclusion and web locations is a conglomeration of a critical design parameters which constitutes a typical conundrum for helicopter structural analysts. Thickness and number of plies are vital design parameters as they significantly influence the cross-section properties of the composite rotor blade and therefore, affects the 2D structural analysis. Therefore selection of best design parameters becomes a cumbersome exercise as the number of design variables increase. In this chapter, ply thickness, number of plies, percentage CNTs and web location are selected as the design variables to formulate an multi-objective optimization problem, which gives a set of Pareto optimal design points. A best trade-off design directs towards an optimal rotor blade cross-section design, which simultaneously satisfies the target objective of minimum structural weight and maximum stiffness.

## **4.4 Optimization problem**

Most of the practical engineering problems pose greater challenges in front of the designers as they have multiple objectives which are mutually conflicting in nature [21]. Helicopter rotor blade design using optimization is a complex and computationally expensive task because of the inherent nonlinearity and contradictory objective functions [22]. Global optimizers, such as, evolutionary algorithms offer superior techniques to address this problem [23]. Recently, Yang has proposed a bat intelligence inspired metaheuristic algorithm [24]. It has been shown that bat algorithm can find global optimal solutions for complex real time optimization problems in an efficient way, than other evolutionary algorithms available in the literature [24, 25]. In this study, a multi-objective framework

of bat algorithm in the realm of multi-objective optimization for the best trade-off design is presented.

The objective of this investigation is to search an optimal design configuration for a composite rotor blade cross-section. A schematic of composite rotor blade section is shown in Figure 3.1. An optimization problem is formulated and analyzed, with four parameters. The design variables considered in the analysis are thickness, number of plies, percentage CNTs and web location. An optimal design of helicopter rotor blade cross-section is the subject of investigation in this study. The baseline design configuration of the composite rotor blade design have 15mm, 8, 10 and 0.35c as ply thickness, number of plies, percentage CNT inclusion and web location, respectively. Stiffness  $S$  and structural weight  $W$  are chosen as the design objectives in this study. Here, structural weight is evaluated per unit length and stiffness is evaluated as a  $l^2$  norm of the stiffness vector as discussed in chapter 3. The values of  $S$  and  $W$  are normalized with respect to the respective baseline design point. These normalized values are denoted by  $y_1$  and  $y_2$ , respectively. The optimization problem for four parameters is formulated as follows:

$$\text{Minimize} \quad \{y_1, y_2\} \quad (4.4)$$

$$\text{subject to :} \quad x_{1,lower} \leq x_1 \leq x_{1,upper} \quad (4.5)$$

$$x_{2,lower} \leq x_2 \leq x_{2,upper} \quad (4.6)$$

$$x_{3,lower} \leq x_3 \leq x_{3,upper} \quad (4.7)$$

$$x_{4,lower} \leq x_4 \leq x_{4,upper} \quad (4.8)$$

Here  $x_1$ ,  $x_2$ ,  $x_3$  and  $x_4$  are the design variables, representing thickness, number of plies, CNT doping percentage and web location, respectively. The objective functions are of conflicting nature for the same choice of design variables, which implies that, to achieve a stiff structure, it would incur high weight inclusion. This kind of optimization problems falls under the category of multi-objective design optimization. An optimization solution is said to be Pareto optimal if it is impossible to minimize one objective without increasing the other objective.

A response surface method (RSM) is used to obtain surrogate models of the objective function in terms of second order polynomials. The optimization problem is decoupled from the expensive structural analysis using RSM technique. Henceforth, these second order polynomial approximations will serve as the objective functions which will be analyzed for Pareto optimal design points using computationally efficient evolutionary optimization algorithms, such as, multi-objective bat algorithm (MOBA) discussed in section 4.7.

## 4.5 Response surface method

Response surface methods (RSM) are a collection of statistical and mathematical techniques which are used for improving and optimizing products and processes. RSM generates a functional relation between an output variable and set of input variables (independent variables) [26],

$$y = f(x) + \varepsilon \quad (4.9)$$

In RSM approach,  $f$  is an unknown function and the error  $\varepsilon$  is treated as a statistical error, with zero nominal distribution, zero mean and variance. Here, the relationship between input variables and output (response) is obtained using a less number of design experiments using orthogonal arrays, discussed in section 4.6. Response surfaces are generally approximated with second order polynomials, as it captures the curvature and interaction effects along with the slope. A second order response surface is obtained by a polynomial multiple regression technique to approximate the objective functions. For instance, a general second order polynomial response surface is,

$$y(x_i) = \beta_0 + \sum_{i=1}^k \beta_i x_i + \sum_{i=1}^k \beta_{ii} x_i^2 + \sum_{i < j} \sum_j^k \beta_{ij} x_i x_j + \varepsilon \quad (4.10)$$

A second order polynomial response surface  $y$  for four design variables is modeled as,

$$\begin{aligned} y(x_1, x_2, x_3, x_4) = & \beta_0 + \beta_1 x_1 + \beta_2 x_2 + \beta_3 x_3 + \beta_4 x_4 + \beta_{11} x_1^2 + \beta_{22} x_2^2 \\ & + \beta_{33} x_3^2 + \beta_{44} x_4^2 + \beta_{12} x_1 x_2 + \beta_{13} x_1 x_3 + \beta_{14} x_1 x_4 \\ & + \beta_{23} x_2 x_3 + \beta_{24} x_2 x_4 + \beta_{34} x_3 x_4 + \varepsilon \end{aligned} \quad (4.11)$$

Regression analysis is used to obtain the regression coefficients  $\beta_0, \beta_i, \beta_{ii}$  and  $\beta_{ij}$ . The method of least squares is invoked to estimate the regression coefficients, which minimizes the sum of the squares of the deviation of the predicted values  $\hat{y}(x_i)$ , from the actual  $y(x_i)$ . Regression coefficients are obtained from Equation 4.11 by writing it in matrix form,  $\mathbf{y} = \mathbf{X}\boldsymbol{\beta} + \varepsilon$ . Both response  $\mathbf{y}$  and error  $\varepsilon$  are  $n$ -dimensional vectors and  $\boldsymbol{\beta}$  is a  $k$ -dimensional vector of regression coefficients. Here,  $k$  is the number of design points and  $\mathbf{X}$  is matrix of sample data points with dimension  $n \times k$ . Regression coefficients are obtained by minimizing the least square error obtained using the following relation,

$$L = \sum_{i=1}^n \varepsilon_i^2 = \boldsymbol{\varepsilon}^T \boldsymbol{\varepsilon} = (\mathbf{y} - \mathbf{X}\boldsymbol{\beta})^T (\mathbf{y} - \mathbf{X}\boldsymbol{\beta}) \quad (4.12)$$

Therefore, with the best estimate of regression coefficients, as,  $\hat{\boldsymbol{\beta}} = (\mathbf{X}^T \mathbf{X})^{-1} \mathbf{X}^T \mathbf{y}$ , the fitted model for the response surfaces is,

$$\hat{\mathbf{y}}(x) = \mathbf{X}\hat{\boldsymbol{\beta}} \quad (4.13)$$

## 4.6 Orthogonal array

Orthogonal arrays provide a systematic approach to perform numerical experiments with only fraction of design points for the factorial design [27, 28]. In the this report, a newly developed 3-level design orthogonal arrays (OAs) named as (MGB4P-OA) is used for non-singular matrix evaluation to create second order polynomial response surfaces with all interaction terms for four parameter problems [29]. Fractional factorial experimental design uses only a fraction of the total number of possible combinations to estimate the main effects and interactions. Here orthogonality means that the factors can be evaluated independent of each other. MGB4P-OA for a 3-level design are shown in Table 4.8. The values -1, 0 and 1 in the tables correspond to the three levels of the design variables. Note that the columns corresponding to the design variables in Table 4.8 are orthogonal to each other. In general form, for an orthogonal array,

$$\begin{aligned} \mathbf{X}_{OA} &= [\mathbf{x}_1, \mathbf{x}_2, \dots, \mathbf{x}_n] \\ \mathbf{x}_i^T \mathbf{x}_j &= 0; \quad i \neq j \end{aligned} \quad (4.14)$$

## 4.7 Multi-objective bat algorithm

A new metaheuristic search algorithm called multi-objective bat algorithm (MOBA) has been developed recently [24]. It has been shown that MOBA algorithm is highly efficient and outperforms already existing algorithms [25, 30]. In this study, MOBA is employed for multi-objective design optimization of composite helicopter rotor blade. Bat algorithm is based on the natural echolocation capability of the bats and a brief description of bat algorithm is outlined below.

Table 4.8: A 3-level MGB4P-OA orthogonal array for four parameters

S.No.	Design Variables			
	$x_1$	$x_2$	$x_3$	$x_4$
1	-1	-1	-1	-1
2	0	0	0	0
3	1	1	1	1
4	0	0	1	1
5	1	1	-1	-1
6	-1	-1	0	0
7	-1	1	0	1
8	0	-1	1	-1
9	1	0	-1	0
10	1	0	0	-1
11	-1	1	1	0
12	0	-1	-1	1
13	1	-1	1	0
14	-1	0	-1	1
15	0	1	0	-1
16	0	1	-1	0
17	1	-1	0	1
18	-1	0	1	-1

### 4.7.1 Echolocation of bats

Bats are quite interesting mammals, with fascinating capabilities of echolocation. They are the only mammals with wings. There are about 996 species of bats and their size varies from tiny bumblebee bats ( $\sim 2\text{g}$ ) to giant bats ( $\sim 1\text{Kg}$ ) with wing span of around 2m. Among the plethora of bat species which account for about 20% mammal species, microbats (with forearm length of about 2.2cm to 11cm) use echolocation quite extensively [31]. Microbats use a type of sonar system, known as echolocation to avoid obstacles, for prey detection and also to locate their roosting crevices in the pitch-dark. These bats transmit loud pulses of sound and listen to the echo that reflect from the surroundings. The pulse variations can be correlated with their hunting methods, which are species dependent. Generally each pulse has a constant frequency which is in the region of 25KHz to 150KHz. Usually these ultrasonic bursts last for a few thousandths of a second (5 to 20ms) and microbats transmit about 200 bursts per second (when they are approaching their prey). These short and intense ultrasonic bursts show the fantastic capability of the signal processing power of bats [24, 31].

Typically the speed of sound in air medium is  $v = 340\text{m/s}$ . The ultrasonic sound bursts with constant frequency  $f$  and wavelength  $\lambda$  are correlated as,

$$\lambda = \frac{v}{f} \quad (4.15)$$

For the frequency range of 25KHz to 150KHz, wavelength  $\lambda$  falls in the range of 2mm to 14mm and such wavelengths are of the same order as their prey size. Altringham reported that microbats use the time difference between their two ears, time delay from the emission and receiving of the echo and the echolocation variation to create a three dimensional map of the environment [32]. It was shown that bats can precisely predict the location and speed of the target and types of prey. Robust optimization algorithms can be formulated towards minimization of an objective, which can be closely associated with the echolocation strategy of the microbats.

### 4.7.2 Pareto optimal multi-objective bat algorithm

Some idealizations are used to develop the echolocation characteristics in the bat algorithm [24]. Bats fly randomly with velocity  $v_i$  and frequency  $f_{min}$  towards location  $x_i$ . They search the prey with loudness  $A_0$  and wavelength  $\lambda$ . Bats can adjust the rate, wavelength (frequency) of the emitted pulses according to the target locations, such that,  $r \in [0, 1]$  and  $A_0 \in [1, 2]$ . Bats wander the ‘d’-dimensional search space with velocities  $v_i$  and location  $x_i$ , as per the following rules,

$$\begin{aligned} f_i &= f_{min} + (f_{max} - f_{min})\beta \\ v_i^t &= v_i^{t-1} + (x_i^t - x_*)f_i \\ x_i^t &= x_i^{t-1} + v_i^t \end{aligned} \quad (4.16)$$

Here  $\beta \in [0, 1]$  is a random vector evaluated using uniform distribution. Here  $x_*$  is the current global best position which is found after comparing all the solutions among all  $n$  bats at time  $t$ . Initially, each bat is randomly assigned a frequency which is obtained from a uniform distribution of  $[f_{min}, f_{max}]$ . Once a solution is selected among the current best solutions, a new solution for individual bat is generated locally using random walk,

$$x_{new} = x_{old} + \varepsilon A^t \quad (4.17)$$

Here  $\varepsilon \in [-1, 1]$  is a random vector and  $A^t = \langle A_i^t \rangle$  is the average loudness of all the bats at time step  $t$ . The loudness  $A_i$  and rate  $r_i$  of pulse emission is updated as bats approach towards their prey. Here,  $A_0 = 1$  and  $A_{min} = 0$  is chosen, where  $A_0$  implies that the bat has found its target and stopped emitting any pulses. Thus,

$$\begin{aligned} A_i^{t+1} &= \alpha A_i^t \\ r_i^t &= r_i^0 [1 - \exp(-\gamma t)] \end{aligned} \quad (4.18)$$

Here  $\alpha$  and  $\gamma$  are constants. For  $\alpha \in [0, 1]$  and  $\gamma > 0$ ,  $A_i^t \rightarrow 0$  and  $r_i^t \rightarrow r_i$  as  $t \rightarrow \infty$ .

Multi-objective optimization problems are often more complex than single objective optimization. Tradeoff design strategies, such as Pareto optimal fronts can be constructed to obtain an optimal compromise design. The Pareto front (PF) of a multi-objective problem can be defined as the set of ‘non-inferior’ or ‘non-dominated’ solutions, such that, [24, 33, 34]

$$PF = \{s \in S \mid \nexists s' \in S : s' \prec s\} \quad (4.19)$$

Here, ‘non-dominated’ solutions implies that for a solution vector,  $\mathbf{a} = \{a_1, a_2, \dots, a_n\}^T \in \mathcal{A}$ , is said to dominate over vector  $\mathbf{b} = \{b_1, b_2, \dots, b_n\}^T$ , if and only if,  $a_i \leq b_i \forall i \in \{1, 2, \dots, n\}$  and  $\exists i \in \{1, 2, \dots, n\} : a_i < b_i$ . It means that no element of  $\mathbf{a}$  is greater than the corresponding entry of  $\mathbf{b}$  and at least one component is smaller. Therefore, another dominance  $\preceq$  relation can be defined as,

$$\mathbf{a} \preceq \mathbf{b} \Leftrightarrow \mathbf{a} \prec \mathbf{b} \vee \mathbf{a} = \mathbf{b} \quad (4.20)$$

Therefore, an optimal location  $x_* \in \mathcal{A}$  is called a non-dominated solution if no solution is found which dominates it [33]. Hence, for the predefined search space, the Pareto optimal set  $PF^*$  is,

$$PF^* = \{x \in \mathcal{A} \mid \nexists x' \in \mathcal{A} : \mathbf{f}(x') \prec \mathbf{f}(x)\} \quad (4.21)$$

Here,  $\mathbf{f} = (f_1, f_2, \dots, f_K)$  is a  $K$ -dimensional set of functions. The set of  $K$  objectives is combined into a single objective using a weighted sum, such that,

$$\begin{aligned} f &= \sum_{i=1}^K w_i f_i \\ \sum_{i=1}^K w_i &= 1 \end{aligned} \quad (4.22)$$

In this investigation, weights are varied systematically to generate the Pareto front. In this report the two objectives,  $S(y_1)$  and  $W(y_2)$  are used to obtain the optimal design of cross-section design of helicopter blade.

## 4.8 Results and discussion

In this work, results are obtained for a composite rotor blade cross-section. Baseline cross-section blade properties for the four design variables, ply thickness, number of plies, percentage CNT inclusion and web location are 15mm, 8, 10 and 0.35c, respectively. Table 4.9 shows the physical and coded values for the four parameter case with four design/decision variables along with their move limits. Here c represents the blade chord. The bounds on the design space are determined by the physical constraints.

Table 4.9: Coded and physical values of design variables for four parameters

Coded values	-1	0	1
	Physical Values		
Ply thickness ( $x_1$ )	0.1mm	0.15mm	0.2mm
Number of plies ( $x_2$ )	6	8	10
% CNT inclusion ( $x_3$ )	0%	10%	20%
Web location ( $x_4$ )	0.25c	0.35c	0.45c

### 4.8.1 Response Surface generation

A MGB4P-OA orthogonal array with 3-level design is employed to construct a nonlinear polynomial response surfaces  $y_1$  and  $y_2$  with all interaction terms till second order, to approximate VAM predictions adequately. Response surfaces decouples the optimization problem from the computational codes and therefore incurs less computational cost. The response surfaces for four parameters using least square method are,

$$\begin{aligned} y_1 = & 1.0147 + 0.2600x_1 + 0.1888x_2 + 0.5235x_3 - 0.0039x_4 - 0.0394x_1^2 \\ & - 0.0327x_2^2 - 0.1669x_3^2 + 0.0259x_4^2 + 0.0301x_1x_2 + 0.1665x_1x_3 \\ & + 0.0066x_1x_4 + 0.1581x_2x_3 + 0.0073x_2x_4 - 0.0090x_3x_4 \end{aligned} \quad (4.23)$$

$$\begin{aligned} y_2 = & 1.0048 + 0.3087x_1 + 0.2303x_2 - 0.0081x_3 - 0.0032x_4 - 0.0091x_1^2 \\ & - 0.0062x_2^2 + 0.0024x_3^2 - 0.0048x_4^2 + 0.0633x_1x_2 - 0.0012x_1x_3 \\ & + 0.0004x_1x_4 - 0.0018x_2x_3 - 0.0001x_2x_4 + 0.0016x_3x_4 \end{aligned} \quad (4.24)$$

Table 4.10 through Table 4.11 shows the comparison of the response surface prediction and VAM analysis using MGB4P-OA for  $y_1$  and  $y_2$  responses, respectively. It is interesting to note that maximum variation between the surrogate prediction and VAM analysis is around 2% for  $y_1$  and less than 1% for  $y_2$ . Response surfaces for  $y_1$  and  $y_2$  are shown in Figure 4.1 and Figure 4.2, respectively with two parameters  $x_1$  and  $x_2$ , while other two parameters  $x_3$  and  $x_4$  are fixed to value  $-1$  for representation.

Figure 4.1 illustrates that ply thickness ( $x_1$ ) has a dominant effect than number of plies ( $x_2$ ) parameter to minimize  $y_1$ . This is also evident from the expression for the objective function in equation (4.23) for  $y_1$ , as the coefficient of ply thickness parameter  $x_1$  is of higher magnitude than  $x_2$ . Figure 4.2 shows the variation of response surface  $y_2$ . It is to be noted that the curvature effects are apparent in Figure 4.1 than in Figure 4.2. This is reflection of the nonlinear expressions present in the response surfaces. The nonlinear coefficients response  $y_1$  are one order of magnitude higher than the response  $y_2$ , as also evident from the expression in equation (4.23) and equation (4.24).

Since both the objectives posses conflicting behaviour towards the decision variables in both the cases. Therefore, a multi-objective Pareto optimal design approach is used to obtain the optimal flap configuration.

### 4.8.2 Multi-objective Pareto optimal design

A multi-objective bat algorithm (MOBA) is implemented to construct the Pareto front for obtaining global optimal solutions. A bat population ( $n = 10$ ), initial loudness  $A_i^0 = 0.25$ ,

Table 4.10: Comparison between predicted response and VAM analysis for  $y_1$  using MGB4P-OA

S.No.	$x_1$ Coded value	$x_2$ Coded value	$x_3$ Coded value	$x_4$ Coded value	$y_1$ RSM prediction	$y_1$ Analysis prediction	% Error
1	-1	-1	-1	-1	0.1917	0.1928	0.6
2	0	0	0	0	1.0000	1.0147	1.5
3	1	1	1	1	2.1285	2.1296	0.03
4	0	0	1	1	1.3900	1.3843	-0.4
5	1	1	-1	-1	0.4053	0.4134	2.0
6	-1	-1	0	0	0.5297	0.5239	-1.1
7	-1	1	0	1	0.8649	0.8640	-0.1
8	0	-1	1	-1	1.0363	1.0378	0.1
9	1	0	-1	0	0.3870	0.3784	-2.2
10	1	0	0	-1	1.2612	1.2585	-0.2
11	-1	1	1	0	1.1867	1.1895	0.2
12	0	-1	-1	1	0.2840	0.2846	0.2
13	1	-1	1	0	1.3495	1.3487	-0.1
14	-1	0	-1	1	0.2143	0.2158	0.7
15	0	1	0	-1	1.2018	1.1933	-0.7
16	0	1	-1	0	0.3250	0.3223	-0.8
17	1	-1	0	1	1.0021	1.0050	0.3
18	-1	0	1	-1	0.9501	0.9508	0.1

initial emission rate  $r_i^0 = 0.5$  is considered. However, loudness ratio  $\alpha$  and pulse reduction rate  $\gamma$  are set as 0.9. MOBA based optimization is found to be computationally efficient for global search in the design space. Figure 4.3 depicts the objective space for four parameters: ply thickness, number of plies, percentage CNTs and web location. Figure 4.3 shows the Pareto front obtained using MOBA with mutually conflicting objectives for four parameter case. Our objective is to maximize the stiffness norm ( $y_1$ ) and minimize the structural weight ( $y_2$ ). It is evident from Figure 4.3, that maximization of the objective  $y_1$  is only possible as the expense of increase in objective  $y_2$ , which is not desirable. Therefore, out of all of the Pareto points, a Pareto optimal point (P) is chosen judiciously which satisfies both the objectives as shown in Figure 4.3.

Design configuration (P) corresponds to 0.1mm, 6, 10 and 0.35c for design variables ply thickness, number of plies, percentage CNTs and web location, respectively. From MOBA algorithm, it is observed that the Pareto optimal design point is achieved with

Table 4.11: Comparison between predicted response and VAM analysis for  $y_2$  using MGB4P-OA

S.No.	$x_1$ Coded value	$x_2$ Coded value	$x_3$ Coded value	$x_4$ Coded value	$y_2$ RSM prediction	$y_2$ Analysis prediction	% Error
1	-1	-1	-1	-1	0.5213	0.5216	0.1
2	0	0	0	0	1.0000	1.0048	0.5
3	1	1	1	1	1.5765	1.577	0.03
4	0	0	1	1	0.9945	0.9927	-0.2
5	1	1	-1	-1	1.6025	1.605	0.2
6	-1	-1	0	0	0.5157	0.5138	-0.4
7	-1	1	0	1	0.8392	0.8393	0.01
8	0	-1	1	-1	0.7605	0.7611	0.1
9	1	0	-1	0	1.3181	1.3161	-0.2
10	1	0	0	-1	1.3040	1.3024	-0.1
11	-1	1	1	0	0.8407	0.8415	0.1
12	0	-1	-1	1	0.7674	0.7675	0.01
13	1	-1	1	0	0.9994	0.9995	0.01
14	-1	0	-1	1	0.6857	0.6863	0.1
15	0	1	0	-1	1.2295	1.2274	-0.2
16	0	1	-1	0	1.2428	1.2412	-0.1
17	1	-1	0	1	0.9963	0.9971	0.1
18	-1	0	1	-1	0.6795	0.6797	0.02

weight  $w = 0.6$ .

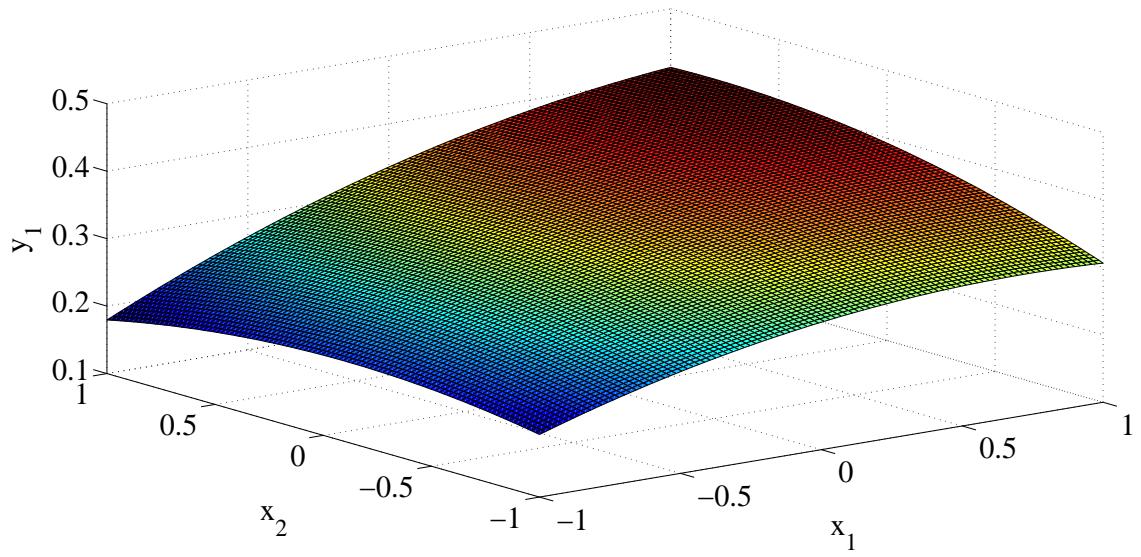


Figure 4.1: Variation in  $y_1$  for  $x_1$  and  $x_2$  in design space

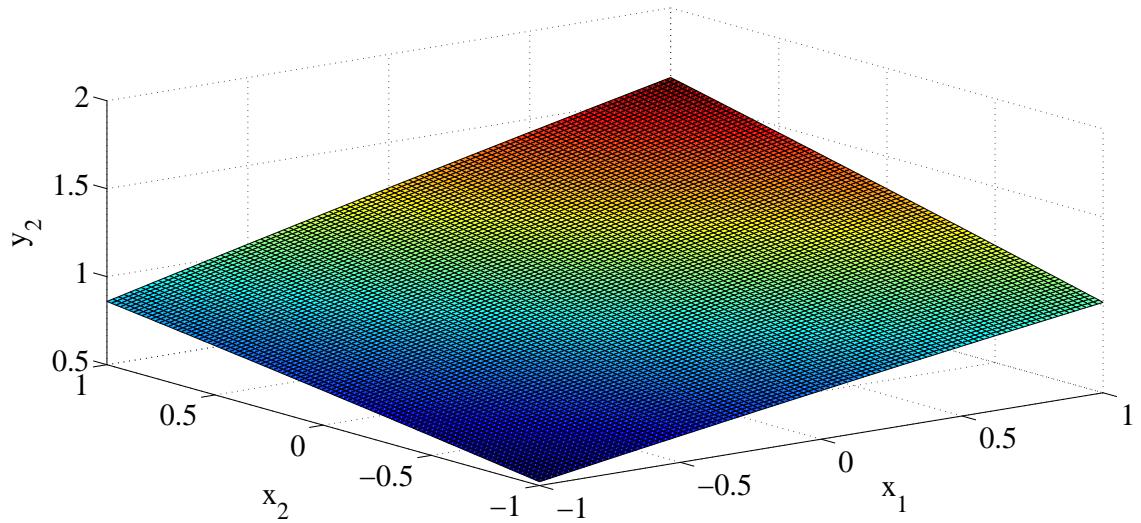


Figure 4.2: Variation in  $y_2$  for  $x_1$  and  $x_2$  in design space

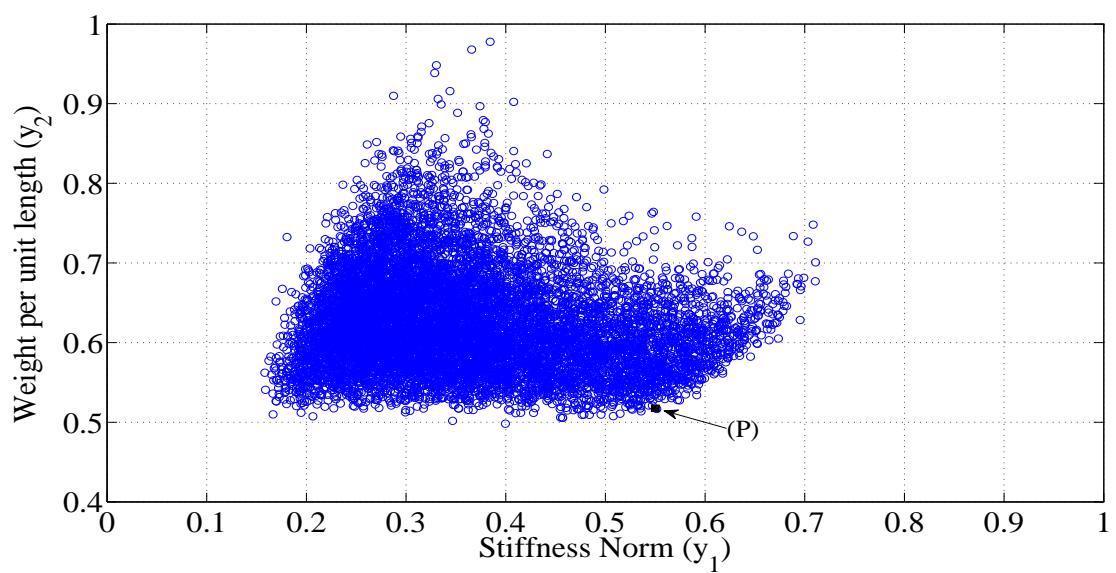


Figure 4.3: Pareto curve for blade cross-section design with four parameters

# **Chapter 5**

## **Vehicle Routing Problem and Path Planning of Aerial Vehicles**

### **5.1 Introduction**

The distribution of goods concerns the service, in a given time period, of a set of customers by a set of delivery vehicles, which are located in one or more warehouses, are operated by a set of autonomous systems. These autonomous systems perform the package distribution using an appropriate path network. The path network, used for the transportation of goods, is generally described through a graph, whose arcs represent the path sections and whose vertices correspond to the path junctions and to the warehouse and customer locations. These problems can be considered as a subclass of vehicle routing problem. Some typical characteristics of these problems are,

- vertex of the path graph in which the customer is located.
- amount of goods, possibly of different types, which must be delivered or collected at the customer.
- periods of the day during which the customer can be served.
- times required to deliver or collect the goods at the customer location.
- subset of vehicles that can be used to serve the customer.

Transportation of goods is performed by using a fleet of vehicles whose composition and size can be fixed or can be defined according to the requirements of the customers. Typical characteristics of the vehicles are

- central warehouse of the vehicle and the possibility to end service at a warehouse other than the central one.
- capacity of the vehicle, expressed as the maximum weight, or volume, or number of the pallets, the vehicle can load.
- costs associated with utilization to the vehicle.

Several different objectives can be considered for the vehicle routing problems. Typical objectives are,

- minimization of the global transportation cost, dependent on the global distance travelled and on the fixed costs associated with used vehicles.
- minimization of the number of vehicles.
- balancing of the routes, as well as avoiding obstacles in case of an aerial delivery system.
- minimization of the penalties associated with partial service of the customers.

The following section contains the formulation of the vehicle routing problem which is a subclass of multiple travelling salesman problem and a genetic algorithm based solution.

## 5.2 Vehicle Routing Problem

In the vehicle routing problem, all the customers correspond to deliveries and the demands are deterministic, known in advance and may not be split. The vehicles are identical and based on either central or forward warehouse, and only capacity restrictions for the vehicles are imposed. The objective is to minimize a weighted function of the number of routes and their length or travel time to serve all the customers.

The vehicle routing problem may be described as the following graph theoretic problem. Let  $G = (V, E)$  be a complete graph, where  $V = 0, \dots, n$  is the vertex set and  $E$  is the edge set. Vertices  $i = 1, \dots, n$  correspond to the customers, where vertex 0 denotes the warehouse. A non negative cost is associated with  $c_{ij}$  is associated with each edge  $(i, j) \in E$  and represents the travel cost spent to go from vertex  $i$  to vertex  $j$ . Each customer  $i$  is associated with a known non negative demand  $d_i$  to be delivered, and the warehouse has a fictitious demand  $d_0 = 0$ . Given a vertex set  $S \subset V$ , let  $d(S) = \sum_{i \in S} d_i$  denote the total demand of the set.

A set of  $K$  identical vehicles, each with capacity  $C$ , is available at the warehouse. To ensure feasibility we assume  $d_i \leq C$  for each  $i$ .  $k_{\min}$  is the minimum number of vehicles

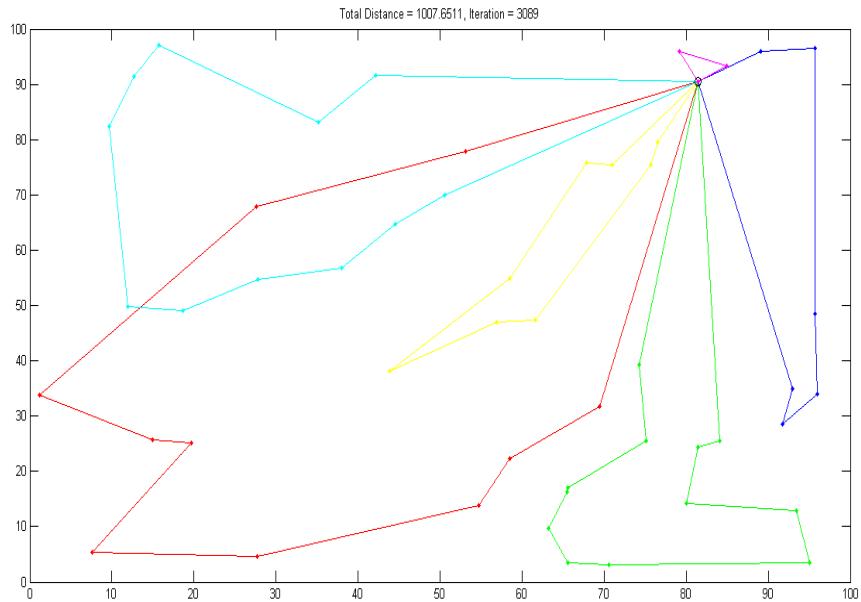


Figure 5.1: A genetic algorithm solution for a vehicle routing problem. Number of customers are 50 and number of vehicles used are 6

needed to be serve all the customers. The value of the  $K_{\min}$  can be solved by determining the Bin Packing Problem associated with the vehicle routing problem.

The vehicle routing problem is known to be a subclass of multiple travelling salesman problem and is NP-Hard. Stochastic algorithm such as genetic algorithm can be used to solve such kind of problems. Figure 5.1, shows one such instance of vehicle routing simulation where number of customers are 50 and the number of vehicles used are 6.

However, the routing problem does not consider the obstacles present in the path and therefore these solutions need to be modified according to the location of the obstacles. These initial solutions can serve as baseline solution on which further modifications are possible. In the following section we discuss the simultaneous motion planning and obstacle avoidance problem for the class of aerial vehicles.

### 5.3 Path Planning Algorithm

Traditionally, motion planning is a decoupled multi-layered approach, consisting of an upper level decision, theoretic planning layer and an inner level control theoretic execu-

tion layer. Although this is a standard practice and applicable to a wide range of systems, systems with complex dynamics very often need an integrated approach. This integrated approach must consider simultaneously the kinematics and dynamics of the system, that is, it must take into account the overall kinodynamic problem. Rapidly Exploring Random Tree or RRT based motion planning is one such method which is widely used for an integrated kinodynamic planning. In this chapter, the RRT methodology is described, as well as new insights to the probabilistic completeness and asymptotic optimality properties of RRT, are also presented. This chapter also contains a new state transition probability based pre-processing method which, when coupled with basic RRT, leads to an improved motion planning solution.

Most approaches of path planning use a decoupled approach. Initially, a basic path is generated in the configuration space ignoring the system dynamics. The trajectory planning calculation is based on a pure kinematic representation of the system. In the next stage an appropriate controller is designed to follow the trajectory generated in the first phase while satisfying system dynamics.

This decoupled approach has several disadvantages. A decoupled motion planning involves separate planning for kinematics and dynamics, which means that the path generated at one stage of planning may not be feasible at all. Also, to generate a collision free trajectory solution, explicit use of system dynamics is necessary. For example, a configuration, consisting of position and orientation of an aircraft, may not be in collision condition with any of the obstacles, but the magnitude and direction of velocity may be such that a collision is imminent. In other words, the vehicle may be in a collision course. This is quite common for systems with significant limits on available controls. Therefore, for trajectory planning the magnitude and direction of velocity must also be taken into account.

These indicate that planning has to be done in state space, which is an augmentation of the configuration space along with linear and angular velocities. Topologically, this comprises the configuration space along with its tangent bundle. For example, for 6-degree of freedom rigid body dynamics, the position  $(x, y, z)$  and Euler orientation angles  $(\phi, \theta, \psi)$ , with respect to some inertial reference frame, represent the configuration space. Any point in such a configuration space is a 6-tuple, represented by  $(x, y, z, \phi, \theta, \psi)$ . The corresponding point can be represented in the state space as a 12 tuple,  $(x, y, z, u, v, w, \phi, \theta, \psi, p, q, r)$  where  $(u, v, w)$  are the linear velocities and  $(p, q, r)$  are the angular velocities. Thus, the dimension of state space is higher than the configuration space.

Motion planning in state space translates to finding control inputs that drives the vehicle on a trajectory from an initial to a final point in the state space, while satisfying both global and local environmental constraints and holonomic or non-holonomic, as well as differential constraints arising from interactions with different external forces and mo-

ments. Such planning methods are called kinodynamic motion planning.

An integral part of kinodynamic motion planning is the representation of obstacles in the state space. Since the dimension of state space is much higher than the workspace, a direct mapping of workspace obstacle to state space obstacle is computationally intensive, and thereby infeasible. To avoid this curse of dimensionality, Lavalle and Knuffer [35] initiated randomized approaches in motion planning. Using the concept of random walk, they created a simple and effective data structure for motion planning which is known as Rapidly Exploring Random Tree (RRT). Till date, RRT is perhaps the only way to perform a quick but effective kinodynamic motion planning in the state space. There exist many variants of the basic RRT algorithm, suitably customized for different motion planning problems.

## 5.4 State Space Formulation of Motion Planning

The configuration of a robot or MAV, with  $n$  degrees of freedom can be represented as a point in a  $d$ -dimensional space, called the configuration space  $\mathbb{C}$ , which is locally like a  $d$ -dimensional Euclidean space  $\mathbb{R}^d$ . A configuration  $q$  in  $\mathbb{C}$  is free if the robot placed at  $q$  does not collide with the obstacles. Let us augment this definition of configuration space with its tangent bundle. A tangent bundle of  $\mathbb{C}$  is defined as  $T(\mathbb{C}) = \cup_{q \in \mathbb{C}} T_q(\mathbb{C})$ , where  $T_q(\mathbb{C})$  is the collection of all tangent vectors at  $q$ . Figure 5.2 illustrates a 2-sphere  $S^2$  and some of its tangent vectors.

The configuration space together with its tangent bundle is called state space  $X$ , in which a state  $x \in X$  is simply defined as  $x = (q, \dot{q})$ . Holonomic constraints can be defined as  $h_i(q, t) = 0$ . Non-holonomic constraints require the use of rate variables and or inequalities, that is  $l_i(q, \dot{q}, t) = 0$  or  $l_i(q, \dot{q}, t) < 0$ . Differential constraints can be written in Lagrangian dynamics as a set of equations of the form  $g_i(q, \dot{q}, \ddot{q}, t) = 0$ , additionally involving acceleration. The use of state space formulation allows representations of the dynamic constraints as a set of  $m$  equations  $G_i(x, \dot{x}) = 0$ ,  $m < 2n$ , where,  $n$  is the dimension of the configuration space. These equations can be rewritten in the form  $\dot{x} = f(x, u)$ , where  $u \in U$  the set of allowable control inputs to the system. The equations thus describe the state transitions resulting from a control input.

To define state space obstacles apart from defining  $x \in X_{Obs} \Leftrightarrow q \in C_{Obs}$  for  $x = (q, (\dot{q}))$ , we need to define the reachable set from an initial configuration. For the system defined by the expression  $\dot{x} = f(x, u)$ , a state  $x'$  can be obtained by applying a control input  $u$  over time  $t$  from an initial state of  $x_0$ . The set of all possible  $x'$  is called the reachable state of  $x_0$  for a time  $t$ , see Figure 5.4. For each state  $x$ , among the set of reachable states, one can define future collision states  $X_{fc}$  and free state space  $X_{free} = X \setminus X_{fc}$ . Note that,  $X_{fc}$  grows as the speed of the system increases and may look rather different from

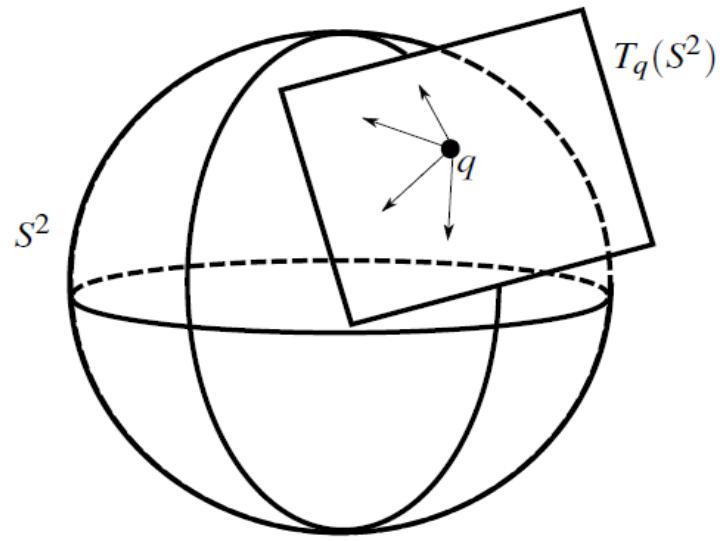


Figure 5.2: A configuration space  $S^2$  and collection of tangent vectors at  $q$

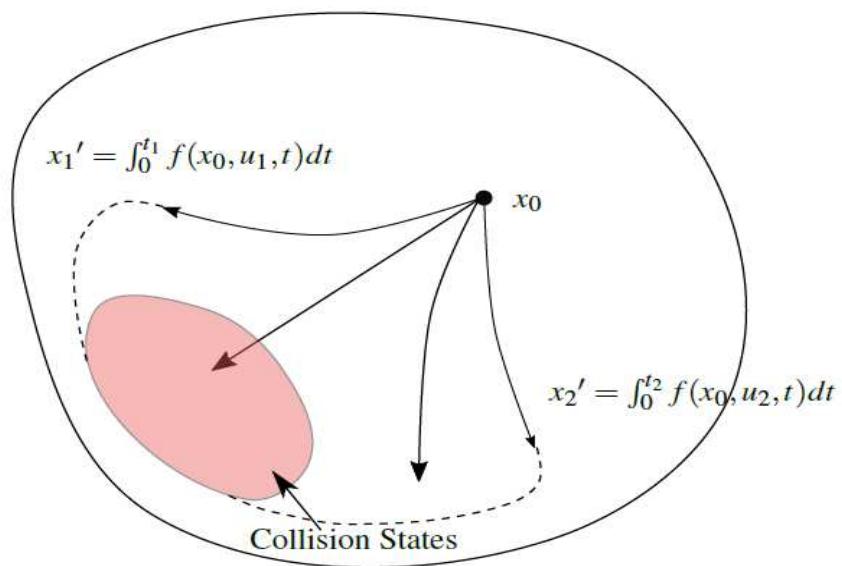


Figure 5.3: Reachable set of  $x_0$  and the collision states

$X_{obs}$ . This makes finding a valid Kinodynamic trajectory more difficult. Therefore, the goal of kinodynamic motion planning is to find a trajectory  $x(t) \in X_{free}$  from an initial state  $x_{init} \in X_{free}$  to a final state  $x_{final} \in X_{free}$  and to find a time parameterized function of control input  $u(t)$  that results in such a trajectory. For convergence issues, we define a general goal subset  $x_{goal}$ , rather than a specific  $x_{final}$ . Clearly,  $x_{final} \in x_{goal}$ .

## 5.5 Rapidly Exploring Random Tree: Algorithm and Simulation

Rapidly Exploring Random Tree (RRT) has been shown to be very effective in solving robot motion planning problems in a complex state space with kinodynamic motion constraints. RRT is introduced in [2], [35] as an efficient data structure and sampling scheme to quickly search high dimensional spaces that have algebraic constraints (arising from the obstacle) and differential constraints (arising from nonholonomy and system dynamics). The algorithm incrementally builds a tree whose nodes are different states of the robot/vehicle. These nodes are added randomly to the tree until one of the node comes close enough to any of the states in  $x_{goal}$ . Next, that goal state is added to the tree and a solution trajectory connecting  $x_{goal}$  and  $x_{init}$  can be found by backtracking the nodes. The edges of the tree forms a one feasible path or solution trajectory connecting a pair of initial and final states. The key idea behind RRT is to bias the tree growth towards unexplored regions of state space by random sampling and extending tree nodes to those regions. The selection of tree nodes for expansion is heavily dependent on current spatial distribution of tree nodes within the state space. Implicitly, the nodes with larger Voronoi cells<sup>1</sup> are more probable for extension. This is because the probability that a node is selected for expansion is directly proportional to the volume measure of its Voronoi cell. The tree node extension logic is based on forward simulation of system dynamics upon random control input. In the following, we present the basic RRT algorithm. The RRT algorithm consists of two subroutines, Build-RRT 5.1 and Extend-RRT 5.2.

The Build-RRT algorithm initially samples a random state or  $x_{rand}$ . In the Extend-RRT function, a nearest node  $x_{near}$  from the tree to the generated random state  $x_{rand}$  is selected for future expansion. The function  $\text{New State}(x_{near}, u)$ , does a forward simulation of system dynamics for  $\Delta t$  time period by applying a control input  $u \in U$ , where  $U$  is a finite input set, to the state at  $x_{near}$ . This input can be chosen at random or can be

---

<sup>1</sup>Voronoi diagram for a set of points  $S$  in a plane is a partitioning of the plane with respect to those points. The partition is formed in such a way that each point in  $S$  belongs to one partition. The points in  $S$  are called sites or nodes. The distance between any point within a partition and the corresponding node is less than the distance between the point and any other node.

---

**Algorithm 5.1:** Build-RRT

---

```
 $T \cdot init(x_{init})$   $\triangleright$  Initialize tree  $T$ ;  
for  $i=1, \dots, K$  do  
     $x_{rand} \leftarrow$  Random Configuration;  
    Extend  $(T, x_{rand})$   
end  
return  $T$ 
```

---

---

**Algorithm 5.2:** Extend RRT

---

```
 $x_{near} \leftarrow$  Nearest Neighbor  $(x, T)$ ;  
 $x_{new} \leftarrow$  New State  $(x_{near}, u)$ ;  
if  $x_{new}$  is Not in Obstacle then  
     $T \cdot add\_vertex(x_{new})$ ;  
     $T \cdot add\_edge(x_{near}, x_{new}, u_{new})$ ;  
    if  $x_{new} \in X_{goal}$  then  
        return Reached;  
    else  
         $\mid$  return Continue  
    end  
end  
end
```

---

selected from all possible inputs by choosing one which yields a new state  $x_{new}$  which is as close as possible to  $x_{rand}$ . The selection of input  $u$  can also be based on minimization of some performance criterion. Further,  $x_{new}$  is checked for collision and system constraint violation. If  $x_{new}$  does not collide with any of the state space obstacles and satisfies all the constraints, then  $x_{new}$  is added to the tree as a child node of  $x_{near}$ ; otherwise it is discarded. If  $x_{new} \in X_{goal}$ , the algorithm stops. This way the vertices or nodes of the RRT tree eventually forms a large connected component with  $X_{free}$  and can come arbitrarily close to a specified  $x_{goal}$ . Note that since the algorithm is only probabilistically complete, the algorithm continues to search for a solution until it finds a close enough node to  $x_{goal}$ . Heuristic termination condition can be added to stop the algorithm after a certain number of iterations. Figure 5.4 shows RRT vertices for an aircraft motion planning problem in the longitudinal plane.

Although RRT vertices can come arbitrarily close to any state in  $x_{goal}$ , the convergence to the solution trajectory may be slow. One solution may be to sample certain  $x_{goal} \in X_{goal}$  repeatedly in random sampling stage so that this introduces a biased sample generation towards  $X_{goal}$ . In such a way, a quick convergence towards the solution trajectory can be found, although it may lead RRT vertices to fall into a trap formed by certain spatial distribution of state space obstacle.

The choice of step size and  $\Delta t$  used in forward simulation of the Extend function is important. If the obstacles are located far away and system dynamics is considerably simple, then a larger step size can be used. In such cases, instead of attempting to extend  $x_{near}$  by incremental step size, one can use the Extend function repeatedly until the extension is no longer possible. That is, a forward simulation produces states that violate system constraints or collide with the obstacle. Obviously, the success of this heuristics method is heavily dependent on the chosen problem. As reported in [36], this modification works best for holonomic planning.

RRT can be used as a single directional or bidirectional planner. A single directional RRT planner builds a tree starting from  $x_{init}$  towards  $X_{goal}$ . A bidirectional planner however builds two separate trees. One from  $x_{init}$  to  $X_{goal}$ , and the other is from any state  $x \in X_{goal}$  to  $x_{init}$ . Once the distance between a pair of vertices from either tree is within a certain tolerance bound, the two trees gets connected and forms a large single connected component. For holonomic planning, a bidirectional planner is faster than the single directional planner. This heuristics, however, does not work for non-holonomic or for differential systems, because of reachability problem.

An important subroutine in the RRT algorithm is the nearest neighbour search. Currently, the basic RRT's nearest neighbour search algorithm works based on the principle of exhaustive search. For a fixed dimension  $d$ , if at any instant the RRT tree contains  $n$  vertices, the task of searching for a true nearest neighbour node from a given query point

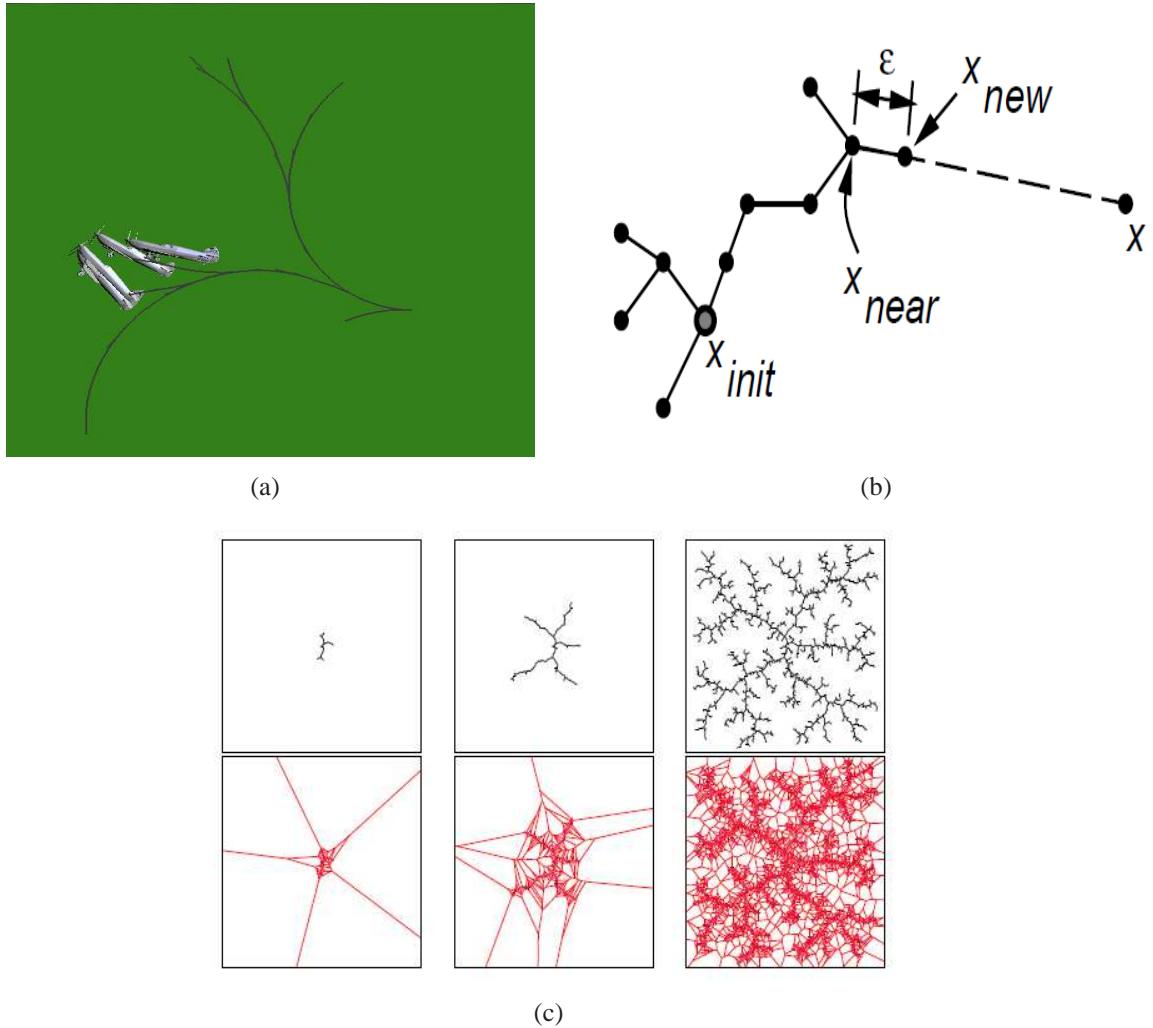


Figure 5.4: (a) RRT vertices after 200 iterations, the aircraft's position and orientation at some RRT nodes are also shown, (b) Illustration of Extend function of RRT algorithm c) RRT vertices after many iterations [2]

has  $O(n)$  time complexity. This approach, although linear with the number of vertices, eventually slows down (in the sense of time) the growth of RRT as the number of vertices increases. It should be noted that any approximate nearest neighbour searching degrades the RRT's exploration capability. For example, suppose at every iteration, a random vertex is selected as the nearest neighbour and RRT is expanded from this vertex. Now, probability of selecting any node from the  $n$  nodes is  $1/n$ . While for a basic RRT, probability of selecting any node  $q$  as nearest neighbour for some query point, is  $O(Vor(q))$ , where  $Vor(q)$  is the associated Voronoi cell of the node  $q$ . Since the node with largest Voronoi area has a higher probability of selection, the RRT vertices tend to grow to the region of largest Voronoi regions or, in other words, to the unexplored regions of state space. Clearly, selecting a random vertex as nearest neighbour is a compromise with the search of unexplored areas. After a large number of iterations if  $O(Vor(q)) \approx 1/n$  then selection of any vertex as nearest neighbour may be effective specially for holonomic cases.

Many variants and modifications of the basic RRT algorithm can be found in [37], [38], [36], [39], [40], etc. in order to address exploration vs. biasing issues, nearest-neighborhood queries, and probabilistic convergence. One shortcoming of the basic RRT algorithm is that it does not take branch cost or path cost value into account while selecting a particular RRT branch for future expansion. Urmson and Simmons, [37] use heuristic to assign costs to different branches of RRT so that a preferable lower cost path can be extended towards the goal. The heuristic is chosen in such a way that the selected branch also maintains a reasonable bias towards exploration. The authors define a path quality measure or cost as a function of different edge cost along the path from the root node to end node, estimated cost to the goal node, and maximum cost between all such paths. A modified nearest-neighbor function selects such nodes for expansion which have a moderate Voronoi region and which may lead to paths of minimum cost measure. Instead of selecting only one neighbor node, a  $k$ -nearest neighbor nodes can also be selected for better exploration. The heuristic often performs poorly when the state space has a poor connectedness or has a narrow passage problem. Jaillet et al. [41] consider motion planning using RRT with certain cost function minimization. This cost function is defined over workspace. For example, it can be an elevation map of the workspace or terrain. A simple RRT planner is used whose exploration nature is controlled or determined by minimizing a cost function. After the random sample generation phase in the RRT algorithm, instead of simply extending the nearest neighbor node, a filtration is performed to search for a low cost solution. The search method finds the gradient of the cost function along the local motion, resulting in an expansion biased to follow the valleys and the saddle points of the workspace. A similar approach is also used by Garcia and How [42], where the authors integrate an artificial potential function as obstacle information to the basic RRT motion planner. The potential function decreases monoton-

ically in the direction of the goal state. The RRT planner follows the negative gradient of the potential function and hence generates a path. Since the obstacles are represented as high peaks in the potential function, they repel any search that follows the negative gradient. Although this method suffers from getting trapped into a local minima, for path planning problem without differential constraints, this method can be very effective. The authors show that this method can be very effective for multiple spacecraft reconfiguration maneuver. Kuwata et al. [43] uses a closed loop approach to extend the basic RRT algorithm. The closed loop approach, called CL-RRT or closed-loop RRT, extends the premise of the basic RRT algorithm to take into account unstable dynamics and uncertainty in system modeling. The method uses a decoupled planning and control approach. Basically, the node extension subroutine of basic RRT algorithm is replaced by an algorithm which samples over a set of feasible reference command inputs instead of sampling directly random servo control inputs. A low level controller is then designed to realize such different reference command input. This way dynamically feasible trajectories can be achieved. The low level controller can be designed separately using any classical or modern control techniques. Once a reference command is generated, CL-RRT runs a forward simulation using the combined vehicle model and the controller to compute the predicted state trajectory. The feasibility of this trajectory is then checked against the vehicle and environmental constraints. The advantage of such decoupled approach is that a low level controller not only stabilizes an unstable system but also can achieve required performance specification. According to the nature of complexity of the vehicle model, more sophisticated but conventional deterministic controller can be designed. One should notice that basic RRT guarantees a solution trajectory as a time parameterized sequence of control inputs which work in an open loop manner. To achieve a closed loop control law, the control input should be a function of current measured states. To achieve closed loop characteristics with basic RRT scheme therefore creates a fundamental problem. This means the basic RRT, instead of sampling random control input for forward simulation, must sample system states. This is infeasible as the system states cannot be any arbitrary one. Therefore, to achieve a closed loop control law a decoupled approach is necessary. Note that, this although violates the very essence of an integrated path planning and control method, such as RRT. Sensitiveness on selected metric is one of the major issues of RRT method. In [44] and [45], Cheng and Lavalle point out the dependence of RRT solution on the metric used to solve motion planning problem. The authors also report an approach which reduces metric sensitivity of the generated solution. They also proposed a modification of the basic RRT algorithm that is capable of adaptively changing exploration strategy of RRT. The proposed method appears as resolution complete as the state space is finitely approximated as an union of  $d$  dimensional balls of radius  $r_d$  and whose center is at each newly created node in the RRT tree. The node extension subroutine of

RRT checks every prospective node to determine whether they belong to any of these already existing balls. If a proposed node does not find any free state space regions which is not covered by the existing balls, the algorithm stops. It is claimed that the reduction of metric sensitivity is achieved by selectively choosing nearest neighbour nodes according to a constraint violation frequency measure. This measure is calculated from estimation of constraint violation probability. This is estimated by exhaustively applying all inputs from the input set to a node and by checking if new nodes emerging from forward simulation of system dynamics, satisfy all the constraints. The nearest neighbour subroutine is modified by confining the nearest neighbour search among the nodes with low constraint violation probability. However, while the tree nodes are sufficiently far away from any type of constraint violation, the nearest neighbour function performs according to the chosen metric. This makes the claim of sensitivity reduction questionable, although the resolution completeness can be very useful as a termination criteria of any RRT.

In [44], it is mentioned that different choice of metric in  $X_{free}$  can lead to a drastic difference in the performance of RRT. This issue of RRT exploration vs. biasing is addressed in [46] in an indirect way. Here the authors propose a method to choose different nodes according to PRM method and then try to push RRT to sequentially follow the PRM vertices. But in general, for dynamical systems, the problem of reachability may occur, and one never knows whether a desired milestone is reachable or not *a priori*. In [38] an adaptive biasing is used. Here the focus is on the selection of the best among  $k$ -nearest neighbors, and on adaptively increasing or decreasing the sampling bias. But again this approach depends on too many tuning parameters that depend on configuration space criticality.

## 5.6 Preprocessing of State Space

Rapidly Exploring Random trees incrementally search a state space. At each iteration, RRT's exploration is determined indirectly by the spatial distribution of a tree's existing nodes. The nodes which have larger Voronoi region are more probable for a new tree branch extension. Hence, exploration of RRT nodes are called Voronoi biased. Note that, for each node the corresponding Voronoi partition is actually independent of the spatial distribution of the state space obstacles. Therefore, for certain spatial arrangement of state space obstacles  $X_{obs}$ , the RRT motion planner may show poor performance characteristics. This poor performance characteristics can be attributed to very slow convergence to the solution, or to not being able to find any solution at all, after the algorithm terminates according to some heuristics. One such case is shown in Figure 5.7. Here, since the volume of the free space inside the obstacle trap is larger than the small narrow opening region of the obstacle, the RRT exploration and node generation can be confined or limited

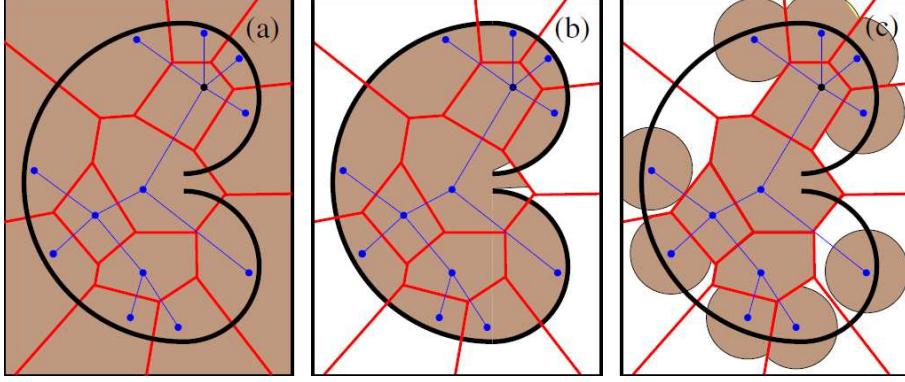


Figure 5.5: Bug Trap Problem. Dynamic domain sampling for RRT exploration [3].

within this obstacle trap. As shown in Figure 5.7, some of the points near the boundary wall have large Voronoi regions, thereby having higher chances of being selected for exploration. This makes the RRT planner’s execution for a new branch extension near the narrow open region very improbable. The chances of sampling inside the narrow passage is even less which makes the solution harder to find for a RRT planner. This problem is known as a bug trap. One intuitive solution to this problem is to consider an obstacle specific sampling scheme. But, since the shape of the state space obstacle is unknown, a direct obstacle based sampling is not practical. Yershova et al. [47] find an indirect way to overcome bug trap problems using the concept of frontier and boundary nodes. The frontier nodes are those nodes in the RRT tree whose Voronoi regions are growing with the size of the environment. The boundary nodes are those that lie in close proximity to the obstacles. Frontier nodes are responsible for exploration. However, when a frontier node becomes a boundary node, the exploration stops. Given a boundary point  $x_b$  at a distance at most  $\epsilon$  from an obstacle in  $\mathbb{X}_{obs}$ , the boundary domain for  $x_b$  is the intersection of the Voronoi region of  $x_b$  and an  $n$  dimensional sphere of radius  $R$  centred at  $x_b$ . The union of all boundary domains is called the dynamic domain of RRT. The algorithm updates the information about the boundary point based on the computation of dynamic domains on the fly. For each boundary point the sampling domain is restricted to its boundary domain. In [3], the authors show that the algorithm solves the bug trap problem in  $\mathbb{R}^2$ . The solution also depends on the choice of the parameter  $R$  in creating dynamic domain of RRT nodes.

The dynamic domain method limits the sample generation domain but it does not quite guide the RRT nodes to find an egress route when such a trap exists. The dynamic domain method is somewhat equivalent to a rejection sampling strategy. It does not force a particular order of sampling sequence so that RRT node can come out of the trap. To do this, it is necessary to identify the regions which, if sequentially searched, may lead

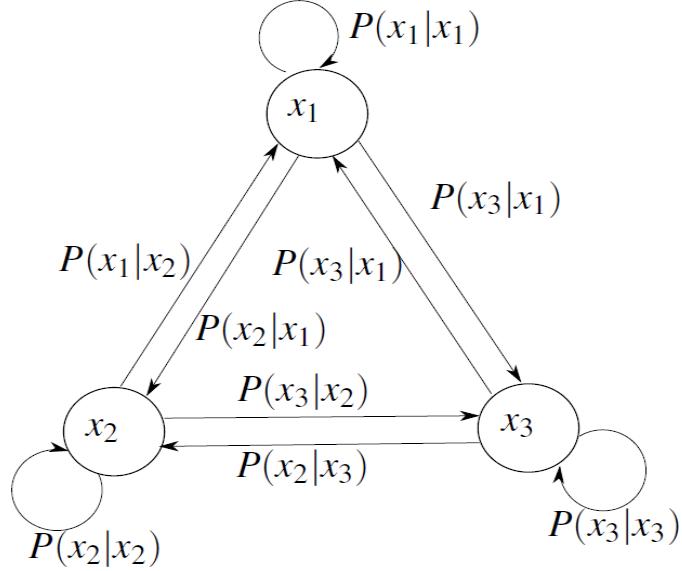


Figure 5.6: The regions  $x_1, x_2, x_3$  and their transition probabilities

to the goal states. Plaku et al. [48] use a multi-resolution approach to motion planning. Initially the method decomposes the workspace to build a graph that encodes the physical adjacency of the decomposed regions. This graph can be searched to obtain leads, which is a sequence of regions that should be explored with sampling based methods to generate solution trajectories. However, this method decomposes workspace and not the state space. Therefore, a certain sequence of decomposed workspace region may not solve the primary problem.

This motivates the identification of the regions of the state space which are worth searching sequentially for a solution trajectory. This requires a pre-processing of state space. This pre-processing will limit the sampling region in the RRT algorithm and establishes an ordered sampling sequence.

Let us assume that the state space is divided into  $N$  non-overlapping regions,  $R_1, R_2, \dots, R_N$ . From a state  $x_i$  in  $R_i$ , upon excitation of any random control input, the forward simulation subroutine generates state  $x_j$ . The probability that the state  $x_j$  will be in  $R_j$  is  $P_{ij}$ , that is,  $P(x_j|x_i)$ . This is the state transition probability from state  $i$  to state  $j$ . Graphically the following Figure 5.6 represents the transitions for 3 regions.

From this we can define a state transition probability matrix  $T_{ij}$ . Let the initial state lie in  $R_i$  and the final state in  $R_j$ . If not all the elements of state transition probability matrix are zero, then there may exist multiple probable paths between any  $R_i$  and  $R_j$ . Each path

consists of a sequence of region to be visited in a particular order. The solution lies in choosing the best sequence of regions that maximizes the probability of  $P(\bar{x}|R_{init}, R_{goal})$ , where  $\bar{x}$  is a state sequence vector. This is the probability of observing the vector containing the sequence of regions, given that initial and final states are in  $R_{init}$  and  $R_{goal}$  respectively. The state sequence which maximizes this probability can be denoted as,

$$\hat{x} = \arg \max_{\bar{x}} P(x|R_{init}, R_{goal}) \quad (5.1)$$

In general, solving this equation requires an exhaustive search over all possible region sequences, which is computationally expensive. The computational complexity of such an exhaustive search is exponential with the number of state space partitions. Instead, a dynamic programming method can be used to calculate the most probable region sequences without the need of performing an exhaustive search. The dynamic programming method, although it has high computational complexity, is still less compared to exponential complexity of exhaustive search. The dynamic programming is recursive and in each iteration for each possible new states, we keep only the path coming out from the previous regions that has the maximum probability. By recursively maximizing the joint probability for each possible new region, we maximize the final probability of the entire sequence of regions. Let us define the single best zone sequence of length  $T$  as  $Q = \{q_1, q_2, \dots, q_T\}$ , where,  $q_1, q_2, \dots, q_T$  are the corresponding cells. Next, we define the quantity  $\delta_t(i)$ , which is the best score along a single path at stage  $t$ , which ends at zone  $i$ , as

$$\delta_t(i) = \max_{q_1, q_2, \dots, q_{t-1}} P[q_1, q_2, \dots, q_t = i] \quad (5.2)$$

Next, by induction

$$\delta_{t+1}(j) = \max_i \delta_t(i) P_{ij} \quad (5.3)$$

To retrieve the cell sequence, we need to keep track of the argument that maximizes (5.3), for each  $t$  and  $j$ . We do this via the array  $\psi(j)$ . The complete procedure for finding the best state sequence can now be stated as

### 1. Initialization

$$\delta_1(i) = \pi_i w_i \quad (5.4)$$

$$\psi_1(i) = 0 \quad (5.5)$$

### 2. Recursion

$$\delta_t(j) = \max_{1 \leq i \leq N} \delta_{t-1}(i) a_{ij} w_i \quad (5.6)$$

$$\psi_t(j) = \arg \max_{1 \leq i \leq N} \delta_{t-1}(i) a_{ij} w_i \quad (5.7)$$

### 3. Termination

$$P^* = \max_{1 \leq i \leq N} \delta_T(i) \quad (5.8)$$

$$q_T^* = \arg \max_{1 \leq i \leq N} \delta_T(i) \quad (5.9)$$

### 4. Back Tracking

$$q_t^* = \psi_{t+1}(q_{t+1}^*), \quad t = T-1, T-2, \dots, 1 \quad (5.10)$$

It is important to choose the number of stages  $T$  or the length of the Markov chain, over which the maximization occurs. We are assuming that a Markovian nature exists while computing the most probable path. For a Markov process, the question of required number of stages  $T$  can be phrased as: How many transitions, will it take to reach region  $j$  for the first time if the system is in region  $i$  initially? This number of transitions is a random variable, defined as  $\Theta_{ij}$ , which is the first passage time of the system from state  $i$  to state  $j$ . To get the answer we must find the probability distribution of  $\Theta_{ij}$ . Let  $f_{ij}$  BE the probability that  $\Theta_{ij}$  will be equal to  $n$ ,

$$f_{ij}(n) = P(\Theta_{ij} = n) \quad (5.11)$$

where,  $n = 1, 2, 3, \dots$ . If we know the probability distribution  $f_{ij}(.)$  for the first passage time  $\Theta_{ij}$ , then we have all possible information ON how long it takes to get from one state to another in a Markov process.

The probability distribution of first passage time characteristics can be calculated recursively. If  $n = 1$ , this could only be accomplished if the process made its first transition to state  $j$ , an event with probability  $P_{ij}$ . If  $n$  is greater than 1, however, the process must have made its first transition to state  $j$  for the first time at a time  $m \leq n$ , and then must have reached state  $j$  once more after the passage of the remaining time  $n - m$ . Since reaching state  $j$  for the first time at time  $m$  is mutually exclusive for different values of  $m$ , we can write the recurrence equation,

$$\phi_{ij}(n) = \sum_{m=1}^n f_i(m) \phi_{ij}(n-m) \quad (5.12)$$

where  $n = 1, 2, 3, \dots$

It is important to estimate transition probability accurately. This requires segmentation of the state space into various appropriate partitions. Since no *a priori* knowledge about the geometry of the state space is assumed, a uniform sampling scheme is used

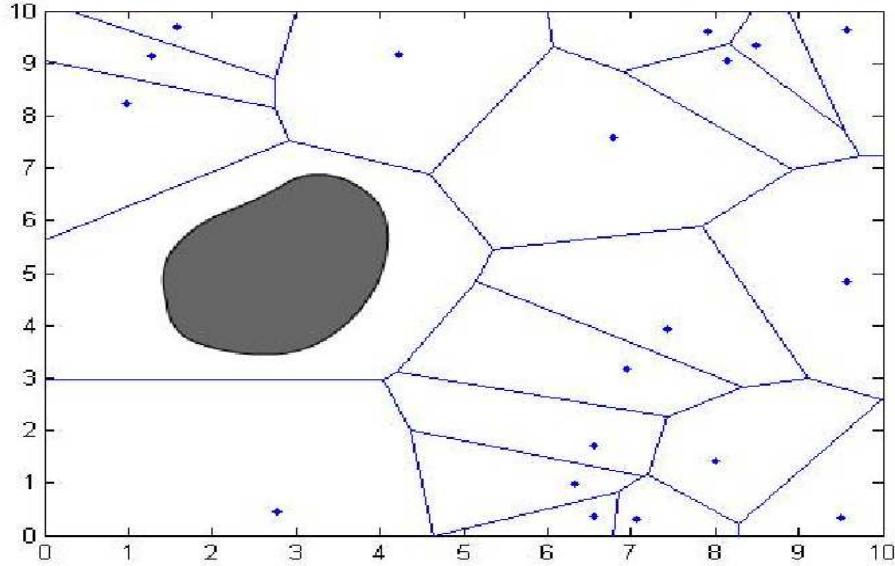


Figure 5.7: Voronoi partition of state space.

to generate  $N$  number of points in the free portions of the state space. The goal is to generate a non-uniform partition of the state space. The suitable value of  $N$ , of course, depends on the dimension and range of the problem instance. Let us call these  $N$  points as registration points. Next, we do a Voronoi partition of the state space based on these  $N$  registration points, according to a chosen metric  $\rho$ . The goal is to find a single step transition probability of a particle from region  $i$  to region  $j$  of this Voronoi partition.

One problem that may occur is, once we partition the state space, connectivity of a region or cell may be lost. Since the shape of the state space obstacle is unknown, the lowest grid resolution required to overcome the problem is also unknown. We can only assume that the state space obstacles, having large volume measure are more likely to create such connectedness problem for a specific  $N$ . Now, if points are generated on the surface of the state space obstacles in a uniform manner, the problem of disconnectedness reduces substantially. We use therefore, the RWS algorithm to find points on the surface of the obstacles. We call this as enrichment of the initial Voronoi cell distribution. The degree of enrichment is dependent on the number  $M$  of additional points generated.

Next, we do a re-partitioning using a Voronoi grid of  $(N + M)$  points. Then, using Monte-Carlo method we approximate the volume measure of the free portions of the Voronoi grid cells, with a confidence level of 0.95 [49]. To estimate this, sample points are generated uniformly. The points which falls inside the obstacles are rejected. Once

we have an approximate measure of the free volume in each cell represented as  $w_i$ , we give random excitation inputs to the individual particles, for a time period of  $\eta\Delta t$  and run a forward simulation of system dynamics using incremental simulator. The incremental simulator gives us the position of the particle after  $\eta\Delta t$ . We then calculate the transition probability  $P_{ij}$ , defined as the probability that the particle at cell  $i$  at time  $t$ , will go to cell  $j$  at time  $t + \eta\Delta t$ . For all such grid cell we get the  $\eta$  step transition probability matrix  $P_\eta$ . Assuming a new time interval  $T = \eta\Delta t$ , we rename this  $P_\eta$  as single step transition probability  $P_{ij}$ . Note that for the transition probability calculation, the underlying assumption of Markovian nature of the process exists. Therefore, if the number of particles that transit to cell  $j$  from cell  $i$  denoted as  $N_{(j|i)}$ , and if number of particles falling inside cell  $i$  denoted as  $N_i$ , then

$$P_{ij} = \frac{N_{(j|i)}}{N_i} \quad (5.13)$$

$$\sum_{i=1}^{N+M} P_{ij} = 1, \quad \forall j \in [1, 2, \dots, N+M] \quad (5.14)$$

Once we have the transition probability of the entire grid region we can calculate the first passage time and most probable path, etc. Following are some simulations which show the effectiveness of the proposed scheme.

## 5.7 Simulation

The path planning procedure clearly depends on

1. The non-uniform grid distribution.
2. The number of grid cells.
3. The number of points generated on the surface of the obstacles.
4. The criticality of the configuration space.
5. The reachable set  $R^k$ .

While implementing the above algorithm one should carefully evaluate the transition probability matrix, as it is the heart of the whole procedure. Depending on grid distribution one may find cases where  $P_{ij} = 1$  which indicates a transient region, [50]. In such case one may generate additional points with increased  $\eta\Delta t$  and try to approximate  $P_{ij}$ . Also, there may be cases where  $P_{ij} = 0$ , because of small cell measure. In this case one can excite the corresponding cell registration point with random control input and thus

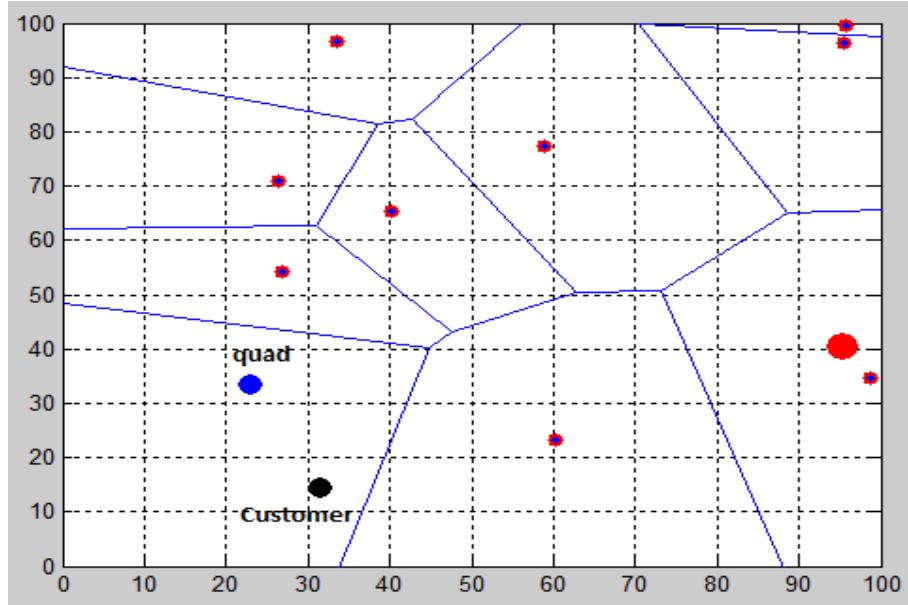


Figure 5.8: (a) Figure showing the quad rotor initial position and the customer location

approximate the value of  $P_{ij}$ . Depending on the existence of narrow passages within the configuration space, there may be large uncertainty in evaluating transition probability matrix.

As a non-holonomic model of an aerial vehicle such as a quad rotor, we assume it can be represented by the following equations.

$$\dot{x} = v \cos \theta \quad (5.15)$$

$$\dot{y} = v \sin \theta \quad (5.16)$$

$$\dot{\theta} = (v/L) \tan \phi \quad (5.17)$$

With these the simulations of the motion planning are shown as follows. Figure 5.8 and 5.9 shows the location of quad rotor and the customer as well as the path planned by the modified RRT algorithm. Figure 5.10 shows another instances of path planning and obstacle avoidance for the quad rotor in the longitudinal plane. Figure 5.11 shows an opengl simulation of quad rotor motion planning and obstacle avoidance in a cityscape.

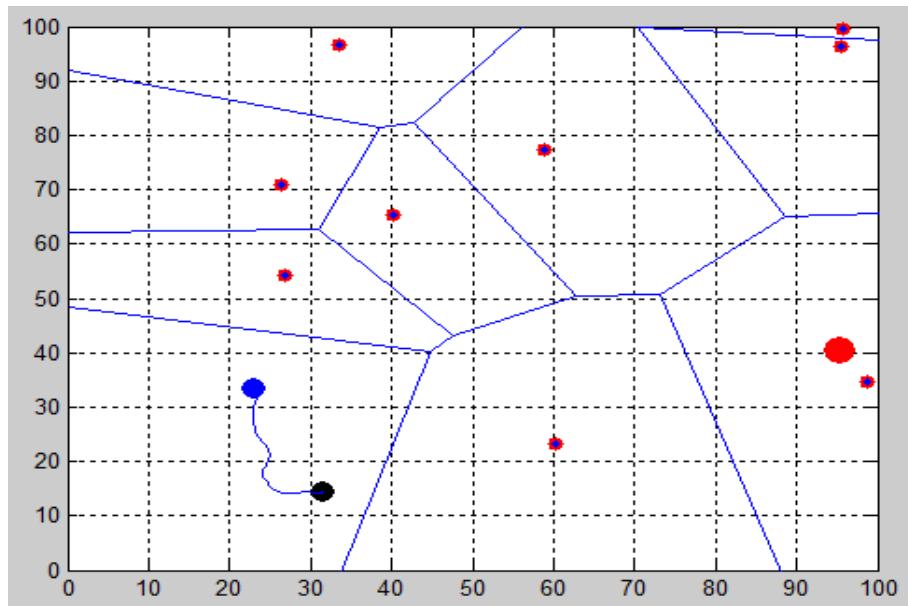


Figure 5.9: (a) Figure showing the path planned by the modified RRT algorithm

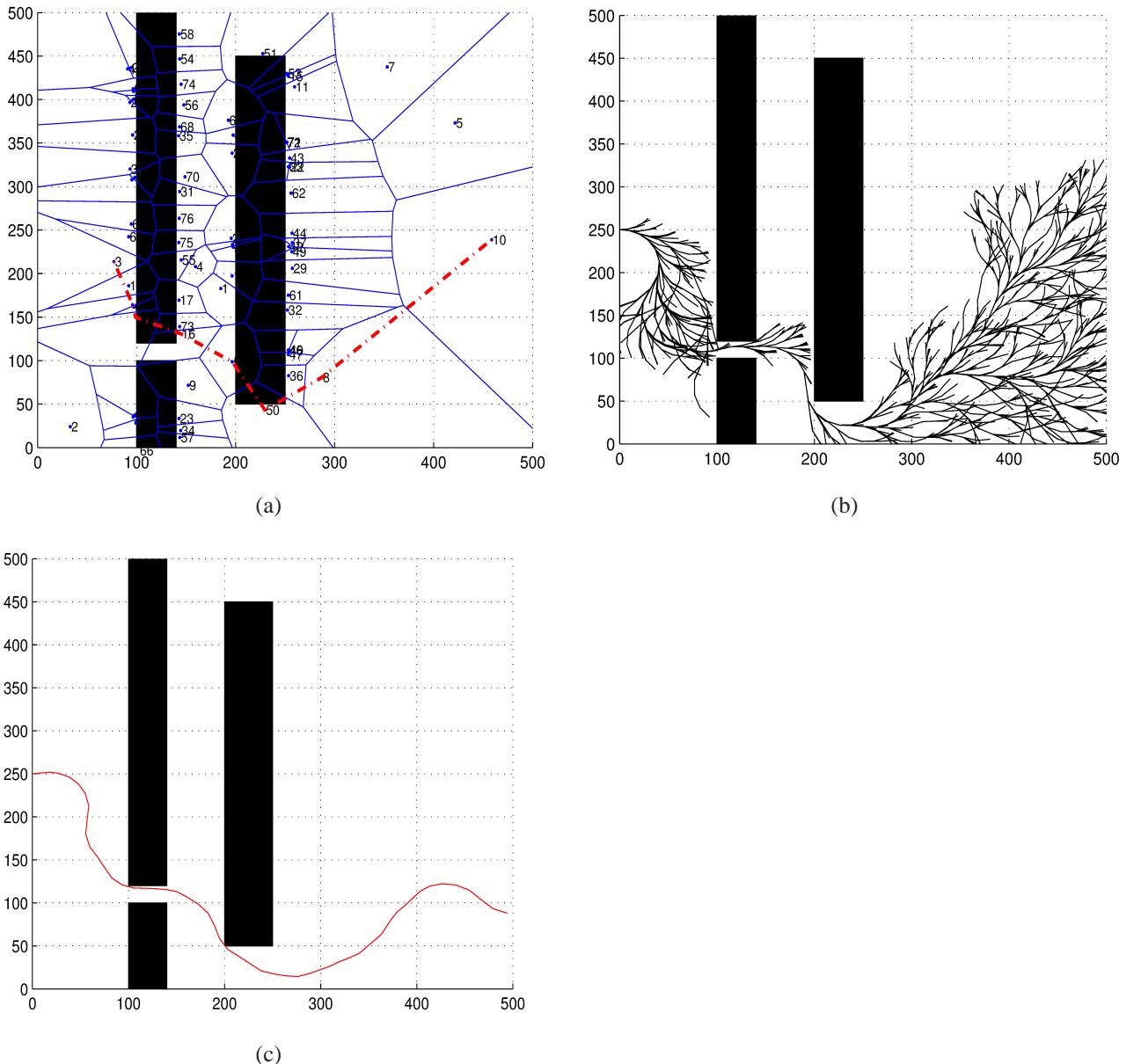
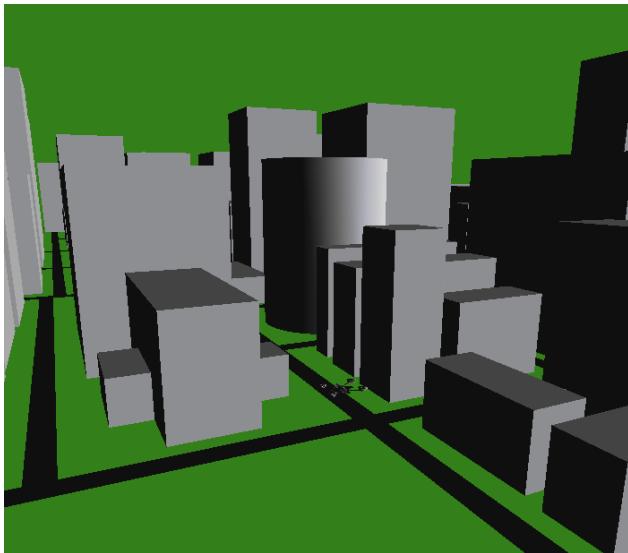
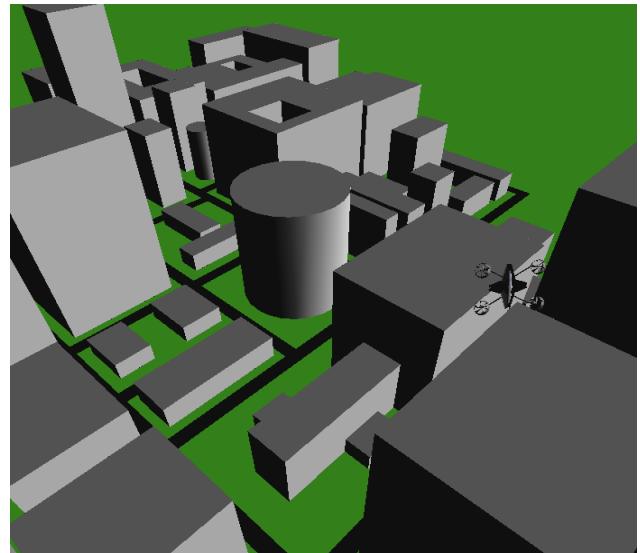


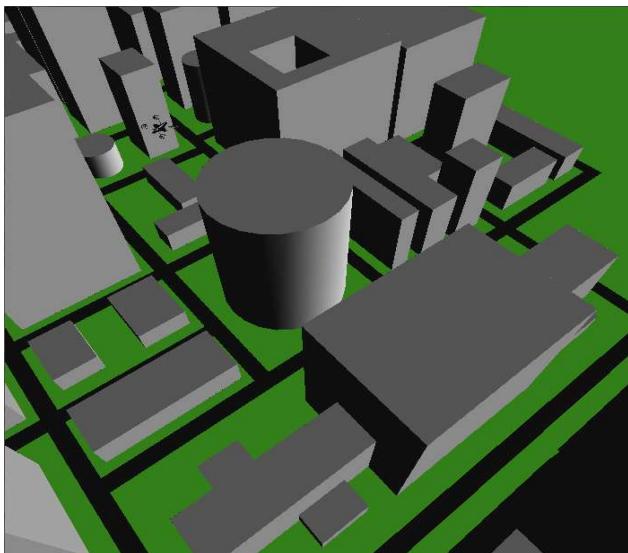
Figure 5.10: (a) Zone sequence as obtained from modified RRT (b) modified RRT vertices distribution after 2000 iteration (c) Path closest to the final state found by modified RRT after 4000 iteration (d)  $u, w, q$  and  $\theta$  variation along the path generated by the modified RRT. Clearly distance from goal configuration to the closest Tree node for modified RRT is less than the basic RRT



(a)



(b)



(c)

Figure 5.11: Figures showing different instance of OpenGL based simulation of quad rotor path planning and obstacle avoidance.

# **Chapter 6**

## **Hardware System Validation**

### **6.1 3D Scanning and CAD Model of Quadcopter Blade**

Reverse engineering is often useful in industries and at times in research, due to efficiency and usability of the existing products. Established products can be utilized for unique design requirements by making specific changes.

We have carried out 3D scanning to develop a CAD model of the rotor blades of the quadcopter. A 3D scanner is a device that analyzes a real-world object and obtains data about its shape and appearance. The collected data can then be used to construct digital three-dimensional models which are useful for CAD. The purpose of a 3D scanner is to create a point cloud of geometric samples on the surface of the component. These points are used to extrapolate the shape of the component (a process called reconstruction). The component is coated with a protective layer to avoid damage and scanned using the equipment shown in Figure 6.1 to generate cloud points.

The generated cloud point's file is converted into IGES (Initial Graphics Exchange Specification) format by using Geomagic software. The cloud points for the rotor blade are shown in Figure 6.2.

Then the file is imported into a 3D modeling software, such as CATIA, to extrapolate the surface of the blades. Figure 6.3 and 6.4 show the 3D surface and CAD model of the blade, respectively. This CAD model is used for 3D printing.

### **6.2 3D Printing**

3D printing or additive manufacturing is a process of making three dimensional solid objects from a digital file. The creation of a 3D printed object is achieved using additive processes. In an additive process an object is created by laying down successive layers



Figure 6.1: 3D Scanner

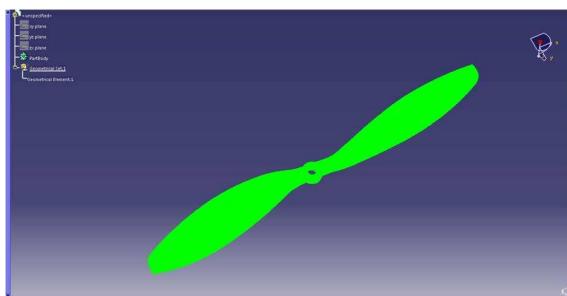


Figure 6.2: Cloud Points Generated from 3D Scanner

of material until the entire object is created. Each of these layers can be seen as a thinly sliced horizontal cross-section. It all starts with making a virtual design of the object you want to create.

To prepare the digital file created in a 3D modeling program for printing, the software slices the final model into hundreds or thousands of horizontal layers. When this prepared file is uploaded in the 3D printer, the printer creates the object layer by layer. The 3D printer reads every slice (or 2D image) and proceeds to create the object, blending each layer together, with no sign of the layering visible, resulting in one 3-dimensional object. Not all 3D printers use the same technology to realize their objects. There are sev-

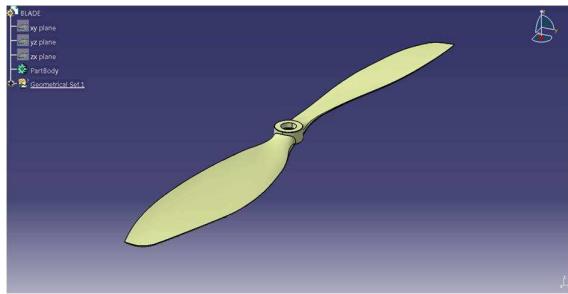


Figure 6.3: 3D Surface of Blade

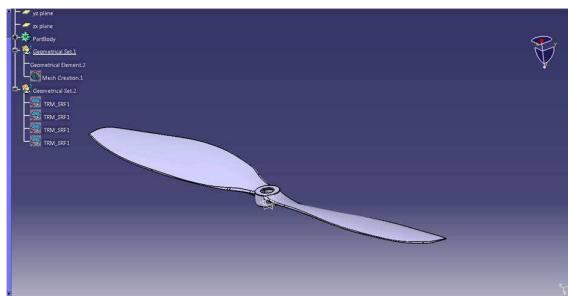


Figure 6.4: 3D CAD Model of Blade

eral ways to do it and all those available, differ mainly in the way layers are built to create the final object. Some methods use molten or softening material to produce the layers. Selective laser sintering and fused deposition modeling are the most common technologies using this way of printing. Another method of printing is to lay liquid materials that are cured with different technologies. The most common technology using this method is called stereolithography. Stereolithography is now one of the most widely used rapid prototyping techniques for plastic models.

Starting from your STL file, the required supports for overhangs and cavities are automatically generated in the model under construction. The support and model files are then "cut" into thin horizontal slices and programmed into the stereolithography 3-D printing machine. This machine then uses a computer-controlled laser to draw the bottom cross section onto the surface of a liquid polymer that hardens when struck by the laser. The part is then lowered to a depth corresponding to the section's thickness and the next cross section is then drawn directly on top of the previous one. This is repeated until the part is finished. The supports are removed manually after the product is taken from the stereolithography machine.

## 6.3 Fabrication and design of the quadcopter

The technical proposal has been validated with a Quadcopter. The quadcopter has been built with a payload capacity of 3 lb, approximately 1.36 kg. Total weight of the quadcopter with the payload is 2.5 kg. The copter can fly at speed 12m/s with 30 minutes endurance, and tilts to approximately 27 degrees angle, from vertical, in flight. The quadcopter can travel a maximum distance of 21.6 kms. The quadcopter will take-off and land vertically. The acceleration at time of take off is  $1 \text{ m/s}^2$ . The Quadcopter will be operated at a service height of 40 m, and will take 13 sec, approximately, to reach the service height after take-off. For first 5 sec, the quadcopter will accelerate at the rate of  $1 \text{ m/s}^2$ , for next 3 sec the quadcopter will move with constant velocity of 5 m/s, and remaining 5 sec the quadcopter will decelerate with  $1\text{m/s}^2$  to attain the desired height. The total weight of the quadcopter has been considered as 2.5 kg and the hardware has been validated against the same weight.

## 6.4 Hardware Components

**Selection of Motor** According to the thrust calculations, the quadcopter requires 4.2084 N minimum thrust. Therefore, each motor driven propeller must provide  $4.2084/4=1.0521$  N thrust. Based on this analysis, four brushless DC motor have been selected. The specifications are given in Table 6.1. Figure 6.5 shows the image of a brushless DC motor, which is used to built the quad copter.

Table 6.1: Specification of the Brushless DC motor

Parameter	: Attribute
Quantity	: 4
Model	: GT 2215/09
RPM/V	: 1180KV
No. of Lipo Cells	: 2-3S
Max Watt	: 312W
Max Current	: 28A
Weight	: 70g
Motor Dimensions	: D28.5 x 36.5 mm
Stator Dimensions	: 22 x 15 mm
Shaft diameter	: 4 mm
Max thrust	: 1250g
Recommended model weight	: 600 - 1100g
Recommended ESC	: EMAX 30A
Recommended Propeller	: EMP 10x4.7SF, EMP 10x5E @3S LiPo



Figure 6.5: Brushless DC motor, which is used to build the quadcopter

**Quadcopter Propeller** Corresponding to the specification of the motor, given in Table 6.1, and based on availability, we have selected the propeller. Table 6.2 contains specification of the propeller. Two propellers are of clockwise pitch angle, and other two

Table 6.2: Quad copter Propeller

Parameter	: Attribute
Quantity	: 4
Product Dimensions	:14.2 x 2.2 x 0.5 inches

propellers are of anti-clockwise pitch angle. Figure 6.6 shows the image of the clockwise and anticlockwise propellers, which are used to built the quadcopter.



Figure 6.6: Clockwise and anticlockwise propeller of the quad copter

**Quad-Copter Frame With Crab Landing Gear** The frame of the quadcopter is selected such that four propellers of specification (Table 6.2) are accommodated properly. The arrangement must ensure smooth air flow during the propulsion, and low inter-propeller interference. From the application point of view, the quadcopter design should have enough space to accommodate a parcel of weight 3 lb. Here, a parcel box of size  $12'' \times 12'' \times 16''$  has been considered, and selected a quadcopter frame with specification, given in Table 6.3. Figure 6.7 shows one of the four arms of the frame. Figure 6.8 shows

Table 6.3: Quad-Copter Frame With Crab Landing Gear

Parameter	: Attribute
Quantity	: 4
Width	: 500mm
Height	: 58mm w/o crab gear 258mm with crab gear
Weight	: 550g (w/ included Crab hi-lift gear)
Motor Mount Bolt Holes	: 16/19mm
hook Rod Rail	: 55-60mm center to center 12mm rod (11.75mm)



Figure 6.7: An arm of the quadcopter Frame

the central body of the quadcopter frame, and Figure 6.9 shows the complete frame.



Figure 6.8: Central Body of the Quadcopter Frame



Figure 6.9: Quad-Copter Frame With Crab Landing Gear

**Speed controller** To produce the required amount of thrust during the different phases of the flight, the propellers have to be run at different RPM. The motor RPM is controlled with help of electronic speed controllers. The speed controllers work on the principle of connecting the motor to the supply voltage in a duty cycle. Based on the motor rating we require a speed controller of minimum 30 A current rating. Table 6.4 contains details of the speed controller, and Figure 6.10 shows the speed controller used to design the quadcopter.

Table 6.4: Electronic speed controller

Parameter	: Attribute
Quantity	: 4
Constant Current	: 30A
Burst Current	: 40A
Battery	: 2-4S Lipoly / 5-12s NiXX
BEC	: 5v / 3A
Motor Type	: Sensorless Brushless
Size	: 54 x 26 11mm
Weight	: 32g



Figure 6.10: Electronic speed controller

**Speed Controller Connector PCB** This PCB is connected to LiPo battery at its input. Four speed controllers are connected to this common PCB to get power supply. Figure 6.11 shows the image and Table 6.4 provides the technical specification of this PCB.

Table 6.5: Speed controller connector PCB

Parameter	: Attribute
Quantity	: 1
Current	: 8 x 20A outputs (MAX)
Power input	: 8 x contact points
Power output	: 8 x contact points
Dimensions	: 50x50x2mm
Weight	: 7.6g (PCB only)

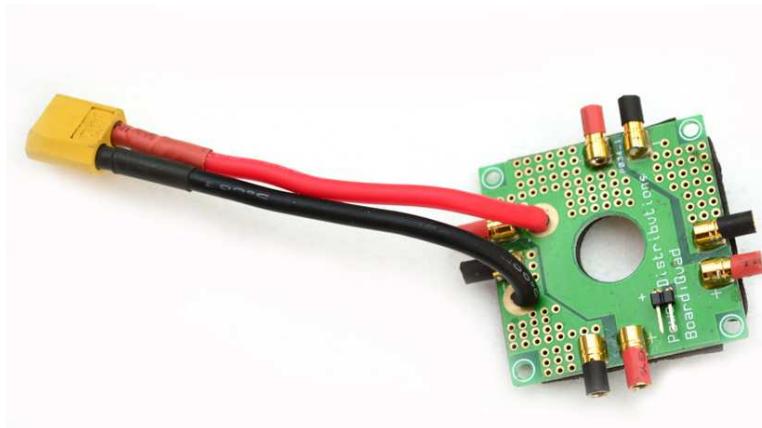


Figure 6.11: Speed controller connector PCB

**Autopilot** This autopilot provides control algorithm to the quadcopter. Here we have used a Multiwii\_Pro/ MegaPirate Flight controller. This controller supported by MegaPirateNG and MultiWii firmware. A GPS can be connected externally to this board directly. The board contains MEMS Gyro, a 3-axis magnetometer and a barometer sensor with a resolution of 0.01 millibar, approximately a 10 cm height difference. Figure 6.12 shows the autopilot board, and Table 6.6 contains its geometrical properties.

Table 6.6: Multiwii\_Pro/ MegaPirate Flight controller

Parameter	: Attribute
Quantity	: 1
Dimension	: 50mm × 50mm
Height	: 11.6mm
Fixing hole spacing	: 45mm
Hole diameter	: 3mm
Weight	: 14.2g

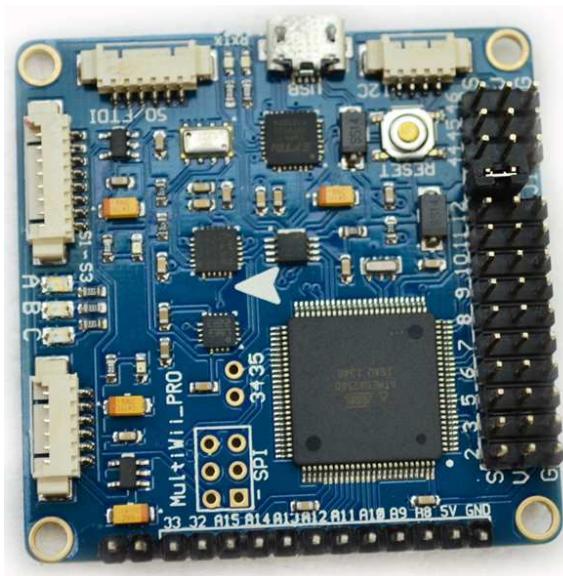


Figure 6.12: Multiwii\_Pro/ MegaPirate Flight controller

Other technical features of the autopilot board are provided below

- Supported MegaPirateNG and MultiWii firmware
- Up to 8-axis motor output
- 8 input channels for standard receiver
- 4 serial ports for debug/Bluetooth Module/OSD/GPS/telemetry
- 2 servos output for PITCH and ROLL gimbal system
- 1 servo output to trigger a camera button
- 6 Analog output for extend device
- A I2C port for extend sensor or device
- Separate 3.3V and 5V LDO voltage regulator
- ATMega 2560 Microcontroller
- MPU6050 6 axis gyro/accel with Motion Processing Unit
- HMC5883L 3-axis digital magnetometer
- MS5611-01BA01 highprecision altimeter
- FT232RQ USB-UART chip and Micro USB receptacle
- On board logic level converter

**Li-Po Battery** Based on the requirement of minimum weight and high current discharge rate, Li-Po batteries were selected as the power bank for the quadcopter. Power requirement calculations:

No. of cells:3. Maximum current rating of ESC=40A. Maximum power of motor=312W at 28A. The thrust required for the levelled flight will require a current of 10A. For endurance of 30 minutes at the required current rating the energy content of battery should be:  $10 \times 4h2 = 20Ah$ . To take into account some hovering time and other losses in flight, a safety factor of 1.1 is considered. Corresponding to above factor minimum capacity of battery should be  $20 \times 1.1 = 22Ah = 22000mAH$ . Number of batteries=2. Minimum Capacity of battery: 12000mAh. Discharge rating=maximum current/battery rating= $28 \times 4 / 2 \times 12 = 4.66C$ . Based on above data the battery selected has following specifications:

Table 6.7: Li-Po Battery

Parameter	: Attribute
Minimum Capacity	: 12000mAh
Configuration	: 3S1P / 11.1V / 3Cell
Constant Discharge	: 10C
Peak Discharge (10sec)	: 20C
Pack Weight	: 244g
Pack Size	: 112 x 34 x 30mm
Charge Plug	: JST-XH
Discharge Plug	: XT60



Figure 6.13: Li-Po Battery

**Transmitter and Receiver Module** The quadcopter can be controlled by a RC transmitter and receiver. The RC transmitter and receiver module, which is used for this project, is shown in Figure 6.14 contains following technical features

1. 2.4 Ghz operating frequency
2. 6-channel (dedicated six input from transmitter to receiver at same time.)
3. PC programmable with cable.
4. Sub trims knobs located besides stick to fine tune the stick response.
5. Endpoint adjustment.
6. Four type of model/stick orientation settings.
7. ACRO, HELI-120, HELI-90 AND HELI-140 settings.
8. Throttle curve adjustment.
9. Channel Mixing
10. Enhanced receiving power with remote receiver.



Figure 6.14: RC Transmitter and receiver module

## 6.5 Final Quadcopter Design

All the parts, described above, are assembled and the final design is shown in Figure 6.15 and Figure 6.16. The direction of propeller rotation are shown in Figure 6.15.

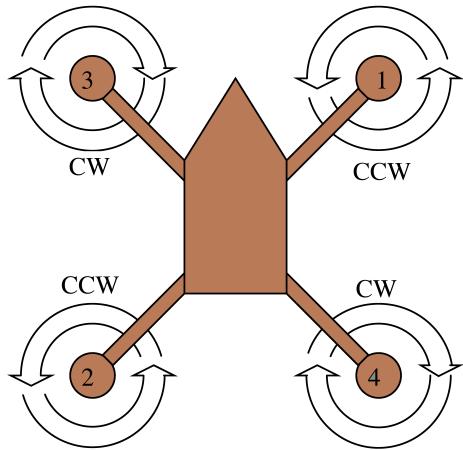


Figure 6.15: Direction of propeller rotation



Figure 6.16: Complete quadcopter

# Chapter 7

## Cost Analysis

Cost analysis of the system-of-system design is performed for three year of operational time. The goal is to obtain a financial data to ensure the sustainability of the whole system. In this proposal, one central Warehouse (CW) location is provided. Four number of Forward Supply Locations (FSLs) are considered to dispatched the packages to the customers. A combination of advanced R-MAX helicopters and quadrotors is used to deliver the requisite 5000 packages to the customers. A set of mathematical relations are developed which accounts for the associated with the requisite monetary items. Cost associated with the proposed system design in accordance with the Measures-of-Effectiveness (MoEs) mentioned in the following sections. The table (7.1) lists the various measures of effectiveness for a quick reference.

### 7.1 Cost associated to forward supply locations

The prescribed monthly rent for additional locations apart from central warehouse is \$15. Four additional forward supply locations (FSLs) are considered in this proposal. These FSLs act as nodal points for their respective zones from where packages are loaded to the UAVs to be delivered to the customers. The FSLs include storage area required for approximately  $1/5^{th}$  of the total packages to be delivered. In addition, they also serve as maintenance and refuelling & (or) recharging stations for the RUAVs.

Area required for storage of 1000 packages in square inches (for one FSL) =  $12 \times 12 \times 1000 = 144000$ . Storage area in square feet =  $144000 \times 0.007 = 1008$ . Percentage additional area considered for larger packages = 10%. Total storage area =  $1110\text{square feet}$ . Service/maintenace area required =  $625\text{square feet}$ . Total area for each FSL in square feet = 1735.

Therefore the cost associated with the rent can be calculated as, Monthly rent for each

Table 7.1: Measures of effectiveness at a glance

Particular	Value
Monthly rent	\$104100
Rent for 3 years of operation	\$3747600
Cost of electrical energy consumed in a single day of typical operation	\$120
Cost of electrical energy consumed in 3 years of operation	\$10800
Pounds of $CO_2$ released in a typical day	799.2lb
Pounds of $CO_2$ released in 3 years of operation	719280lb = 326.26metric ton
Labor and operation cost per day	\$1000
Labor and operation costs for 3 years	\$900000
Development cost for advanced R-MAX RUAV	\$28219136
Development cost for quadrotor RUAV	\$661386
Total development cost	\$28880522

$FSL = 15 \times 1735 = \$26025$ . Monthly rent for all 4 FSLs = \$104100. Total rent for three years of operation = \$3747600

## 7.2 Cost for electricity consumed by vehicles

Maximum rate of energy consumption by a single quadrotor in a typical mission =  $11.1V \times 40 = 444W$ . Energy consumed by a single quadrotor in a typical mission =  $0.444 \times 0.5KW - hr$ . Cost of total energy consumed in a single day of operation =  $(0.444 \times 0.5 \times 3000)KW - hr \times \$0.18/KW - hr = \$120$ (approx.). Therefore cost of total energy consumed in 3 years of operation =  $120 \times 300 \times 3 = \$10800$ .

## 7.3 Pounds of CO<sub>2</sub> released for grid based charging

As per the prescribed rate of  $CO_2$  released per KW-hr of grid based charging

Pounds of  $CO_2$  released in a typical day =  $1.2 \times 0.444 \times 0.5 \times 3000 = 799.2$

Pounds of  $CO_2$  released in 3 years =  $799.2 \times 300 \times 3 = 719280$

$CO_2$  released in 3 years in metric tons = 326.26

## 7.4 Vehicle repair labor and operation

Total labor and operation maintenance cost per day = \$100 per hour  $\times$  10 hour per day = \$1000. Total labor and operation maintenance cost for 3 years =  $\$1000 \times 300 \times 3 = \$900000$ .

## 7.5 Development cost of RUAVs based on empty weight

Empty weight of advanced RMAX RUAV =  $64kg = 141.096lb$

Empty weight of quadrotor =  $1.5kg = 3.3069lb$

$$\text{Total development cost} = 200000 \times (141.096 + 3.3069) = \$28880600 \quad (7.1)$$

# Bibliography

- [1] Sodano., H. A., *AFOSR Mech. of Multifunctional and Microsystems Review*, 2012.
- [2] Lavalle, S. M., “Rapidly-exploring random trees: A new tool for path planning,” Tech. Rep. TR 98-11, Iowa State University, Oct. 1998.
- [3] Yershova, A., Jaillet, L., Siméon, T., and LaValle, S. M., “Dynamic-domain RRTs: Efficient exploration by controlling the sampling domain,” *Robotics and Automation, 2005. ICRA 2005. Proceedings of the 2005 IEEE International Conference on*, IEEE, 2005, pp. 3856–3861.
- [4] Leishman, J. G., *Principles of Helicopter Aerodynamics*, Cambridge university press, 2nd ed., 2006.
- [5] Lin, X.-j., Zhou, K.-c., Zhang, X.-y., and Zhang, D., “Development, modeling and application of piezoelectric fiber composites,” *Transactions of Nonferrous Metals Society of China*, Vol. 23, No. 1, 2013, pp. 98–107.
- [6] Beckert, W. and Kreher, W. S., “Modelling piezoelectric modules with interdigitated electrode structures,” *Computational Materials Science*, Vol. 26, 2003, pp. 36–45.
- [7] Padhee, S. S., “A Synergetic Micromechanics Model For Fiber Reinforced Composites,” 2014.
- [8] Liao, L. and Yu, W., “An electromechanical Reissner–Mindlin model for laminated piezoelectric plates,” *Composite Structures*, Vol. 88, No. 3, 2009, pp. 394–402.
- [9] Roy, S. and Yu, W., “A coupled Timoshenko model for smart slender structures,” *International Journal of Solids and Structures*, Vol. 46, No. 13, 2009, pp. 2547–2555.
- [10] Koutsawa, Y., Belouettar, S., Makradi, A., and Tiem, S., “X-FEM implementation of VAMUCH: Application to active structural fiber multi-functional composite materials,” *Composite Structures*, Vol. 94, No. 4, 2012, pp. 1297–1304.

- [11] Tan, P. and Tong, L., “Micromechanics models for non-linear behavior of piezo-electric fiber reinforced composite materials,” *International journal of solids and structures*, Vol. 38, No. 50, 2001, pp. 8999–9032.
- [12] Tang, T. and Yu, W., “Effective nonlinear behavior of electrostrictive multiphase composites: A micromechanical study,” *International Journal of Engineering Science*, Vol. 48, No. 12, 2010, pp. 1769–1777.
- [13] Berdichevsky, V., *Variational Principles of Continuum Mechanics: I. Fundamentals*, Springer Science & Business Media, 2009.
- [14] Hashin, Z. and Rosen, B. W., “The elastic moduli of fiber-reinforced materials,” *Journal of Applied Mechanics*, Vol. 31, No. 2, 1964, pp. 223–232.
- [15] Yu, W., “VAMUCH Manual for Users,” 2010.
- [16] Yu, W., “Manual of GEBT,” 2011.
- [17] Hodges, D. H., “Nonlinear composite beam theory,” *Progress in astronautics and aeronautics*, Vol. 213, 2006, pp. 304.
- [18] Tressler, J., Alkoy, S., Dogan, A., and Newnham, R., “Functional composites for sensors, actuators and transducers,” *Composites Part A: Applied Science and Manufacturing*, Vol. 30, No. 4, 1999, pp. 477–482.
- [19] Hu, Y. and Rao, S. S., “Robust Design of Horizontal Axis Wind Turbines Using Taguchi Method,” *Journal of Mechanical Design*, Vol. 133, No. 11, 2011, pp. 111009.
- [20] Roy, R. K., *A primer on the Taguchi method*, Society of Manufacturing Engineers, 2010.
- [21] Geem, Z. W., “Multiobjective optimization of time-cost trade-off using harmony search,” *Journal of Construction Engineering and Management*, Vol. 136, No. 6, 2009, pp. 711–716.
- [22] Rao, S., Dhingra, A., and Miura, H., “Pareto-optimal solutions in helicopter design problems,” *Engineering Optimization*, Vol. 15, No. 3, 1990, pp. 211–231.
- [23] Crossley, W. A., Wells, V. L., and Laananen, D. H., “The potential of genetic algorithms for conceptual design of rotor systems,” *Engineering Optimization*, Vol. 24, No. 3, 1995, pp. 221–238.

- [24] Yang, X.-S., “Bat algorithm for multi-objective optimisation,” *International Journal of Bio-Inspired Computation*, Vol. 3, No. 5, 2011, pp. 267–274.
- [25] Yang, X.-S. and He, X., “Bat algorithm: literature review and applications,” *International Journal of Bio-Inspired Computation*, Vol. 5, No. 3, 2013, pp. 141–149.
- [26] Myers, R. H. and Anderson-Cook, C. M., *Response surface methodology: process and product optimization using designed experiments*, Vol. 705, John Wiley & Sons, New Jersey, 2009.
- [27] Ganguli, R., *Engineering optimization: a modern approach*, Universities Press, Hyderabad, 2012.
- [28] Roy, R. K., *A primer on the Taguchi method*, Society of Manufacturing Engineers, Dearborn, MI, 2nd ed., 2010.
- [29] Mallick, R., Ganguli, R., and Bhat, M. S., “Robust design of multiple trailing edge flaps for helicopter vibration reduction: A multi-objective bat algorithm approach,” *Engineering Optimization*, , No. ahead-of-print, 2014, pp. 1–22.
- [30] Yang, X.-S., “Review of meta-heuristics and generalised evolutionary walk algorithm,” *International Journal of Bio-Inspired Computation*, Vol. 3, No. 2, 2011, pp. 77–84.
- [31] Richardson, P., *Bats*, The Natural History Museum, New York, revised and reformat ed., 2011.
- [32] Altringham, J. D., Hammond, L., and McOwat, T., *Bats: biology and behaviour*, Oxford university press, Oxford, 1996.
- [33] Coello Coello, C. A., “An updated survey of evolutionary multiobjective optimization techniques: state of the art and future trends,” *Proceedings of the 1999 Congress on Evolutionary Computation*, Vol. 1, IEEE, Washington D.C., 1999, pp. 3–13.
- [34] Deb, K., *Multi-objective optimization using evolutionary algorithms*, John Wiley & Sons, Chichester, 2001.
- [35] LaValle, S. M. and Kuffner, J. J., “Randomized kinodynamic planning,” *The International Journal of Robotics Research*, Vol. 20, No. 5, 2001, pp. 378–400.
- [36] Lindemann, S. R. and LaValle, S. M., “Current issues in sampling-based motion planning,” *Robotics Research. The Eleventh International Symposium*, Springer, 2005, pp. 36–54.

- [37] Urmson, C. and Simmons, R. G., “Approaches for heuristically biasing RRT growth.” *IROS*, Vol. 2, 2003, pp. 1178–1183.
- [38] Kim, J., Esposito, J. M., and Kumar, V., “Sampling-based algorithm for testing and validating robot controllers,” *The International Journal of Robotics Research*, Vol. 25, No. 12, 2006, pp. 1257–1272.
- [39] Pepy, R. and Lambert, A., “Safe path planning in an uncertain-configuration space using RRT,” *Intelligent Robots and Systems, 2006 IEEE/RSJ International Conference on*, IEEE, 2006, pp. 5376–5381.
- [40] Frazzoli, E., Dahleh, M. A., and Feron, E., “Real-time motion planning for agile autonomous vehicles,” *American Control Conference, 2001. Proceedings of the 2001*, Vol. 1, IEEE, 2001, pp. 43–49.
- [41] Jailllet, L., Cortés, J., and Siméon, T., “Sampling-based path planning on configuration-space costmaps,” *Robotics, IEEE Transactions on*, Vol. 26, No. 4, 2010, pp. 635–646.
- [42] Garcia, I. and How, J. P., “Improving the efficiency of rapidly-exploring random trees using a potential function planner,” *Decision and Control, 2005 and 2005 European Control Conference. CDC-ECC’05. 44th IEEE Conference on*, IEEE, 2005, pp. 7965–7970.
- [43] Kuwata, Y., Karaman, S., Teo, J., Frazzoli, E., How, J. P., and Fiore, G., “Real-time motion planning with applications to autonomous urban driving,” *Control Systems Technology, IEEE Transactions on*, Vol. 17, No. 5, 2009, pp. 1105–1118.
- [44] Cheng, P. and LaValle, S. M., “Reducing metric sensitivity in randomized trajectory design,” *Intelligent Robots and Systems, 2001. Proceedings. 2001 IEEE/RSJ International Conference on*, Vol. 1, IEEE, 2001, pp. 43–48.
- [45] Cheng, P. and LaValle, S. M., “Resolution complete rapidly-exploring random trees,” *ICRA*, 2002, pp. 267–272.
- [46] LaValle, S. M. and Kuffner Jr, J. J., “Rapidly-exploring random trees: Progress and prospects,” 2000.
- [47] Yershova, A., Jailllet, L., Siméon, T., and LaValle, S. M., “Dynamic-domain RRTs: Efficient exploration by controlling the sampling domain,” *Robotics and Automation, 2005. ICRA 2005. Proceedings of the 2005 IEEE International Conference on*, IEEE, 2005, pp. 3856–3861.

- [48] Plaku, E., Kavraki, L. E., and Vardi, M. Y., “Discrete Search Leading Continuous Exploration for Kinodynamic Motion Planning.” *Robotics: Science and Systems*, 2007, pp. 326–333.
- [49] Fishman, G. S., *Monte Carlo : concepts, algorithms, and applications*, Springer-Verlag New York, 1996.
- [50] Howard, R. A., *Dynamic Probabilistic Systems, Volume I: Markov Models*, Vol. 1, Dover Publications, 2007.